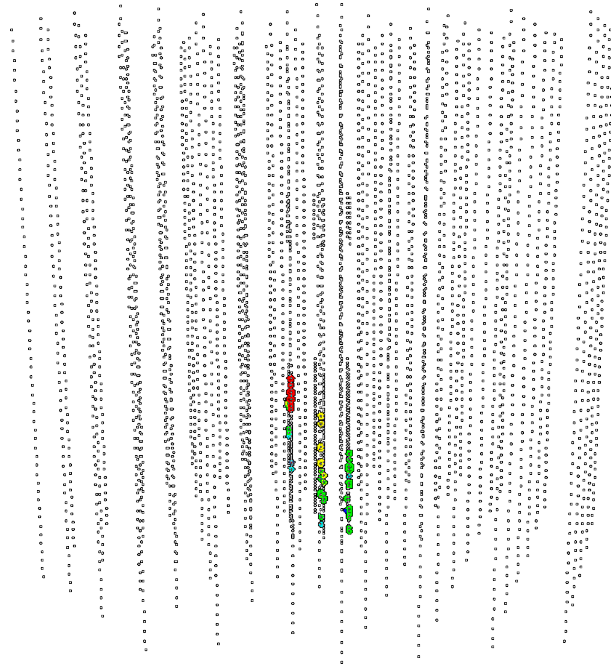# The design study of IceCube DeepCore: Characterization and veto studies

Olaf Schulz

Max-Planck Institut für Kernphysik

Heidelberg 2010

Dissertation
submitted to the
Combined Faculties of the Natural Sciences and Mathematics
of the Ruperto-Carola-University of Heidelberg, Germany
for the degree of
Doctor of Natural Sciences

Put forward by
Olaf Schulz
born in Hamburg, Germany
oral examination: 21.07.2010

The design study of IceCube DeepCore:
Characterization and veto studies

Abstract

In this thesis the design study for the low energy extension to the IceCube neutrino telescope, called DeepCore, is presented. IceCube and DeepCore are currently under construction at the geographic South Pole, Antarctica. With DeepCore the energy threshold of IceCube is significantly lowered, opening new possibilities to, e.g., improve low-energy point source searches, to measure standard vacuum neutrino oscillations and to increase the sensitivity to solar dark matter annihilation signals. In parallel to the DeepCore design study a, software based, active atmospheric muon veto technique has been developed, which for the first time, allows IceCube to measure neutrinos with a full sky (4π) acceptance, although at a significantly reduced effective volume.

Furthermore, in the course of the active atmospheric muon veto development, a new opportunity has been discovered to also reduce the measured rate of atmospheric muon neutrinos, a previously irreducible background to any search for extra-terrestrial neutrinos. This effect has been analytically studied, independent of any detector design.

As of today, the first data-taking period with full atmospheric muon veto capabilities lies ahead. This thesis concludes with a first look on early data taken with DeepCore and a first estimation of a sensitivity to a southern hemisphere point source.

Zusammenfassung

In dieser Arbeit wird die zentrale Design-Studie für die Niedrig-Energie Erweiterung "DeepCore", des IceCube Neutrino Teleskops, vorgestellt. IceCube und DeepCore befinden sich derzeit im Bau am geographischen Südpol. Mit DeepCore wird die Energieschwelle von IceCube signifikant gesenkt, was neue Möglichkeiten eröffnet um, unter anderem, die Suche nach galaktischen Neutrino-Punktquellen zu optimieren, Neutrino-Oszillationen in einem bisher nur grob vermessenen Energiebereich zu messen und eine

höhere Sensitivität für etwaige, durch Annihilation dunkler Materie induzierte, Neutrino Signale von der Sonne zu erreichen.

Parallel zu der DeepCore Design-Studie, wurde eine neuartige, Software-basierte, Technik entwickelt um den Hintergrund von atmosphärischen Myonen zu reduzieren (Myon-Veto). Mit dieser Technik ist es IceCube erstmals möglich im gesamten messbaren Energiebereich nach Neutrinos aus der südlichen Hemisphäre zu suchen, wenn auch mit reduziertem effektivem Volumen.

Desweiteren wurde, im Laufe der Entwicklung dieser Myon-Veto Technik, eine Möglichkeit entdeckt, auch die gemessene Rate von atmosphärischen Neutrinos zu reduzieren. Diese stellen einen bislang unreduzierbaren Hintergrund für alle Suchen nach Neutrinos extraterrestrischen Ursprungs dar. Dieser Effekt wurde, unabhängig von einem etwaigen Detektor-Design, analytisch untersucht.

Zum Zeitpunkt der Beendigung dieser Arbeit beginnt die erste Datennahme von IceCube mit DeepCore bei der die volle Myon-Veto Kapazität zur Verfügung steht. Diese Arbeit endet mit einem ersten Blick auf mit DeepCore genommene Daten und einer ersten Abschätzung der Sensitivität DeepCores zur Messung einer Punktquelle am Südhimmel.

Für Kathrin und Marlene

Contents

List of Figures

LIST OF FIGURES

List of Tables

LIST OF TABLES

About this thesis

This thesis consists of three main parts, which interweave with each other. It starts out with an introductory part, which covers cosmic ray and neutrino astro- and particle-physics. Then it gives an introduction to neutrino detection methods, conditions and analysis strategies with the IceCube neutrino telescope.

The second part of the thesis deals with the design of the DeepCore low-energy extension of IceCube as well as development and performance of atmospheric muon veto techniques which can be applied to provide IceCube and DeepCore with access to neutrino signals from the southern hemisphere.

The third part of the thesis covers the newly discovered effect of a possible rejection of atmospheric muon neutrinos in analyses that cover the hemisphere of the location of a given neutrino detector.

Finally, the current detector status and a first sensitivity estimation to a southern sky point source are presented.

Author's contribution

An huge experiment like IceCube can only be run successfully in a big collaboration between many skilled scientists. Every member of the collaboration is focusing their efforts on a different task with typically large overlap to other members. Thus, the results presented in this thesis are to a large degree a product of teamwork. Here I list the results to which I have provided major contributions since my joining of the IceCube collaboration in January 2007. The work on the analytic estimation of the atmospheric neutrino veto effect was independent of the IceCube collaboration.

- **Atmospheric muon veto:**

- contribution of geometrically penalized veto simulations to the first veto feasibility study

- code development of geometrically penalized veto

- code revision and development of the causally related hit veto algorithm

- veto efficiency optimization studies focused on the first atmospheric muon veto level (hit veto)

- **DeepCore design study:**

  - veto efficiency and optimization studies for the first atmospheric muon veto level (hit veto) at all stages of the design study

  - effective volume studies for the new locations of replaced strings number 79 and 80

- **Atmospheric neutrino veto:**

  - significant contribution to all stages of the work which was done in collaboration with T. K. Gaisser[1], E. Resconi and S. Schönert[2] and published in [85]

---

[1]Bartol Research Institute, University of Delaware, Newark, U.S.A.
[2]both: Max-Planck Institut für Kernphysik, Heidelberg

1

Introduction

At 1:06 p.m. on the 30th of March 2010 the first collisions of protons at 7 TeV center of mass energy were observed at the Large Hadron Collider near Geneva, Switzerland [1]. These were the largest energies to which mankind has ever accelerated single nucleons and enormous efforts had to be taken to reach this goal. However, these energies are not the largest ever observed by mankind. In fact, compared to the highest energetic nuclei ever observed, the energies at the LHC are quite moderate. Somewhere in our universe sources exist which can accelerate charged protons and nuclei to energies larger than 10^{20} eV (more than 10^7 times larger then LHC energies[1]). We know this, because we observe such high energetic particles when they hit our atmosphere and create cascades of particles and electro-magnetic radiation. These are the cosmic rays, which were first observed and correctly interpreted by Victor Hess in his famous balloon flights in 1911 [60]. Today, almost 100 years after Hess' discovery, we still do not know for sure where the sources of the cosmic rays are, as the charged particles are deflected on their way to Earth by the galactic magnetic fields. Thus, the only charged cosmic ray source ever observed is our own Sun and it does emit particles only at the lowest observed energies. There is, however, some fundamental knowledge on the kind of sources which could be able to accelerate cosmic rays to the observed energies. Stellar supernovae, their remnants, active galactic nuclei, gamma-ray bursts, pulsars and x-ray binaries are the most prominent among them. These are the most violent objects in the known universe, emitting large amounts of energy in form of electro-magnetic radiation and possibly also in the accelerated charged particles that we observe as cosmic rays. Even if these do not point back to their sources, it is likely that they will leave traces at,

---

[1]The composition of cosmic rays at the highest energies is not well known, however even for the heaviest nuclei the energy per nucleon will still be five orders of magnitude above the LHC proton energy.

or near the location of their sources. If they interact with the ambient matter close to their source, hadronic interactions will produce pions. In the decay chain of this pions gamma-rays (π^0) and neutrinos ($\pi^\pm$) will be produced and, being electrically neutral particles, these point back to their sources if observed at Earth. Now, gamma-rays can also be produced in other processes not involving charged nuclei and they might be (partially) absorbed in interstellar matter. Neutrinos on the other hand, are ideal tracers of cosmic ray acceleration sites as they hardly interact and are thus unabsorbed and un-deflected. This advantage, unfortunately, also implies that neutrinos are very hard to detect and huge volumes are needed to be able to measure significant fluxes.

Today, the largest of the detectors which are built to measure an extra-terrestrial neutrino signal is IceCube [24]. IceCube is located at the geographic South Pole next to the Amundsen-Scott South Pole station and is going to be completed in the upcoming austral season 2010/11. When finished, IceCube will equip roughly 1 km^3 of antarctic glacial ice in depths between 1450 m and 2450 m with 5160 optical modules to detect the Čerenkov light of neutrino induced charged leptons and cascades. The density of this optical modules is optimized for detection of neutrino induced muon tracks at about 10 TeV neutrino energy. This energy corresponds to the average neutrino energy obtained from an initial cosmic ray energy (at the neutrino production site) of $\mathcal{O}(1\ \text{PeV})$[71]. At these cosmic ray energies one of the few features of the cosmic ray energy spectrum, a steepening of the exponential power law often called "the knee", has been observed and a detection of a neutrino source at these energies would not only reveal the cosmic accelerators, but eventually also give some insides on the origin of this spectral feature.

Another reason for the design energy of IceCube is the background of atmospheric neutrinos. It is produced in the air-shower cascades initiated by cosmic rays. The meson decays that produce these neutrinos also produce muons, which form the largest background in a neutrino telescope. It is to avoid mis-identification of this overabundant muon background, that IceCube (and other neutrino telescopes) predominantly look for neutrinos that come from below, i.e. that have crossed through the Earth. Thus the muon background is effectively reduced, but the background of atmospheric neutrinos becomes irreducible, since the neutrino carries no information on the distance to its production site. However, the energy spectrum of the atmospheric neutrinos is steeper than the expected energy spectra of astro-physical sources and thus it is expected that above several TeV a signal can be effectively distinguished from the background. This agrees well with IceCubes design energy.

Nevertheless, a number of recent observations of galactic gamma-ray sources, which might be associated with cosmic ray acceleration, show cut-offs or a steepening in their energy spectra at a few TeV to some tenths of TeV [32][31][30][33]and thus the assumption is consistent, that also the potential neutrino spectra would show such a cut-off. This would be expected at approximately half the energy of the gamma-rays [71]. Below these energies IceCube is not optimized and the atmospheric neutrino background is large making it difficult to separate a signal from the background. On the other hand, the additional information on potential source spectra provided by gamma-ray observations can in some cases be used to optimize searches for neutrino point sources. The energies below 1 TeV are also of large interest for other research topics of IceCube, besides the cosmic rays, such as the search for a dark matter induced neutrino signal coming from the core of the Earth or the Sun. With a lower energy threshold the parameter space of models predicting such particles beyond the standard model could be further constrained. But also the physics of atmospheric air-showers at these energies are a topic of research within the IceCube collaboration.

The detection and reconstruction of neutrino events at lower energies calls for a denser spacing of optical modules. Initially this task was fulfilled by IceCubes predecessor, the Antarctic Muon And Neutrino Detector Array (AMANDA) [25]. AMANDA provided a denser module spacing and by 2007 it had been fully integrated into the IceCube data-taking procedure. The combined data has been used with success to improve galactic point source searches and dark matter analyses, but the maintenance of AMANDA grew increasingly difficult. Therefore it was proposed, that AMANDA should be decommissioned and replaced by a new extension to IceCube, dedicated to the low energy analyses. Thus the idea of IceCube DeepCore was born and the story of its design and construction is one of major success.

A large part of this thesis covers the DeepCore design study in detail, which has been achieved in a remarkably short time period. From the first proposal to the deployment of the first DeepCore modules, less then two years have passed. On the one hand, this was little time for an extended design study, but on the other, a deployment of DeepCore within the planned IceCube construction seasons was by far the most cost-effective solution, which also guaranteed the longest detector lifetime and has now been proven to be a winning strategy. We will show, how DeepCore has been designed to study neutrino induced muons and cascades at energies in the 100 GeV range and below, with a trigger threshold at only a few GeV. These energies also open the possi-

bility to study neutrino particle physics, i.e. neutrino vacuum oscillation in an energy range not well measured by preceding experiments such as SuperKamiokande [20].

The second main topic of this thesis is the development of an active veto against atmospheric muons which went hand in hand with the DeepCore design study. Throughout this work, algorithms have been devised to use a large part of the instrumented volume of IceCube as a veto detector to efficiently detect and reject atmospheric muon events entering the detector from the outside. A reduced fiducial volume in the bottom center part of the IceCube detector can then be used to look for downwards-going starting (neutrino induced) muon or cascade events, thereby opening IceCube's field of view to the southern hemisphere. This is a novel opportunity in a neutrino telescope. The background rejection achieved with the devised algorithms has been shown, in Monte Carlo simulations, to effectively reduce the muon background below the flux of atmospheric neutrinos and thus DeepCore provides a full sky (4π) coverage in the search for neutrino point sources, dark matter induced particles and for neutrino oscillation studies. Note however, that this is only possible at a significantly reduced effective volume, which, for the point source searches, is aimed to be comparable to that of the ANTARES detector in the Mediterranean [17].

Additionally, in the course of the muon veto development, a new opportunity to also reduce the background of atmospheric neutrinos, became apparent. The atmospheric muon background has its origin in the same decays of mesons within atmospheric air-showers as does the atmospheric neutrino background. Since the energies of interest are very large, these decay products are heavily boosted and appear almost aligned when they reach typical detector depths. Therefore, an atmospheric neutrino event, e.g. in DeepCore, can be rejected if the accompanying muon, from the same meson decay, is detected by the veto system[1]. Thus the formerly (for upwards going neutrinos) irreducible atmospheric neutrino flux might be significantly reduced when looking for downwards-moving events. We have estimated this effect analytically and found a dependence of the veto probability on the neutrino energy and zenith angle, with a veto probability of $>99\%$ for vertical neutrinos above 10 TeV. This study was done independent of IceCube and the effect has been evaluated at different depths in water. Eventually it may lead to a paradigm change in the conception of neutrino telescopes, as future experiments could devise shallow veto layers to effectively reduce the muon

---

[1]Note, that this is a conservative assumption, as the veto could also be triggered by another muon of the same air-shower.

background and retain much larger effective volumes than that of IceCube DeepCore. The atmospheric neutrino veto effect is not only a potential aid to neutrino point-source (or other) searches with downwards-going events, but, as it comes naturally with the atmospheric muon veto system, it is also a systematic effect to all such analyses, even if a veto effect is not desired, as e.g. in neutrino oscillation up-down asymmetry measurements.

The structure of this thesis is the following: After this short introduction to the thesis, in the second chapter, we give an overview of the relevant neutrino and cosmic ray physics which form the main motivations for IceCube and DeepCore and we elaborate the necessary background for the presented studies. In the third chapter we shed some light on neutrino detection principles and give a short overview over the IceCube detector layout, data-taking procedures and analysis techniques. The fourth chapter is dedicated to the atmospheric muon veto techniques and follows their development from the first proof of feasibility to the current algorithm performance. The DeepCore design study is thereafter discussed in chapter 5 from the first proposal to the final layout. We the present the results of the analytic evaluation of the atmospheric neutrino veto effect and go on to a summary of the first DeepCore performance checks and a first estimate of a sensitivity to southern hemisphere point sources.
Finally, we report on results of the analytic evaluation of the atmospheric neutrino veto effect and conclude by a summary and outlook.

1. INTRODUCTION

2

Cosmic rays and neutrinos: An introduction

Neutrino astronomy is a relatively new branch within the young field of astro-particle physics. It is tightly related to the physics of cosmic rays and to high energy γ-ray astronomy and combines neutrino particle physics with the physics of astrophysical sources.

In this chapter, we give both the physics motivations and the background to the work done throughout this thesis. We will start with a short summary of the current knowledge on cosmic rays as they are observed at the Earth. For neutrino astronomy they do not only impose the main motivation (by the means of answering the question "Where do they come from?"), but they also are the main source of backgrounds for any search of extra-terrestrial neutrinos. These background sources are muons and neutrinos from cosmic ray air-showers produced in the Earth's atmosphere. We will put a special focus on analytic descriptions of the spectra of these background particles. A novel method to suppress these backgrounds has been developed throughout this thesis.

From there we will go on with a brief overview of the potential high energy neutrino and cosmic ray source candidate classes and the acceleration processes supposed to happen in them. A short description of the hadronic interaction will lead us to motivate the indirect search of cosmic ray sources via γ-rays and neutrinos. The connection of γ-rays and neutrinos and the implications of measured γ-ray source spectra on expected neutrino fluxes are briefly touched thereafter.

Finally, we will outline other potential sources of neutrinos, such as dark matter, and will briefly discuss neutrino oscillations.

2.1   Cosmic rays at the Earth: Spectrum and composition

Cosmic rays hit the Earth at an average rate of $\sim 1000 \, \frac{\text{particles}}{m^2 \, s}$. They are mostly high energetic fully ionized nuclei, but also electrons, positrons as well as γ-rays and neutrinos. The most abundant nuclei are protons (90%) and α-particles (9%). The remainder are heavier nuclei up to uranium. The abundances of the individual nuclei follows mostly the abundance of elements in stellar matter, i.e. it follows the odd/even effect resulting from nuclear stability. This indicates that cosmic rays are of stellar origin. Nevertheless, a few elements, such as Lithium, Beryllium and Boron are by orders of magnitude more abundant in cosmic rays. This is generally understood as a consequence of interactions of carbon and oxygen nuclei with interstellar matter (spallation), in which the rare elements are produced. The fact that the individual spectra of these elements are steeper than the overall cosmic ray spectrum supports this understanding.

The cosmic ray energy spectrum is shown in figure (2.1). It follows a power law of the form

$$\frac{\text{d} N_0(E)}{\text{d} E} \; \propto \; E^{-(\gamma+1)} \tag{2.1}$$

over more than 10 orders of magnitude up to the highest observed energies of more than 10^{20} eV. Note that this is about seven orders of magnitude above the highest energies produced at man-made accelerators! The spectrum is nearly feature-less, having only few slight changes to the spectral index. Up to the so called "knee" at ≈ 4 PeV the spectral index is $\gamma + 1 \approx 2.7$. Above the knee the spectrum steepens to $\gamma + 1 \approx 3.0$. At energies above 10^{18}eV ("the ankle") the spectrum gets harder again. The origin of these features is not fully understood. The flux below the "knee" ($E_{CR} < 10^{15}$eV) is generally attributed to sources within our own galaxy as the measured cosmic ray energies can be understood in terms of 1st order Fermi acceleration in supernova shock waves (see below). The flux above the ankle ($E_{CR} > 10^{18}$eV) on the other hand is generally attributed to purely extra-galactic sources by a simple argument. The magnetic fields within our galaxy have an average strength of $B \sim 3 \, \mu G$ which confine most of the cosmic rays. But at very large energies and thus also large rigidity $R = p \, / \, Ze$ cosmic ray nuclei can not be confined anymore (depending also on their charge) and thus would leave our galaxy. Other arguments question if there are sources in our galaxy powerful enough to produce these cosmic ray energies.

The steepening of the spectrum between "knee" and "ankle" has hypothesized to be related to the composition of cosmic rays through the different charge-dependent confinement energies of the cosmic ray components [91][88][62]. The measurement of the
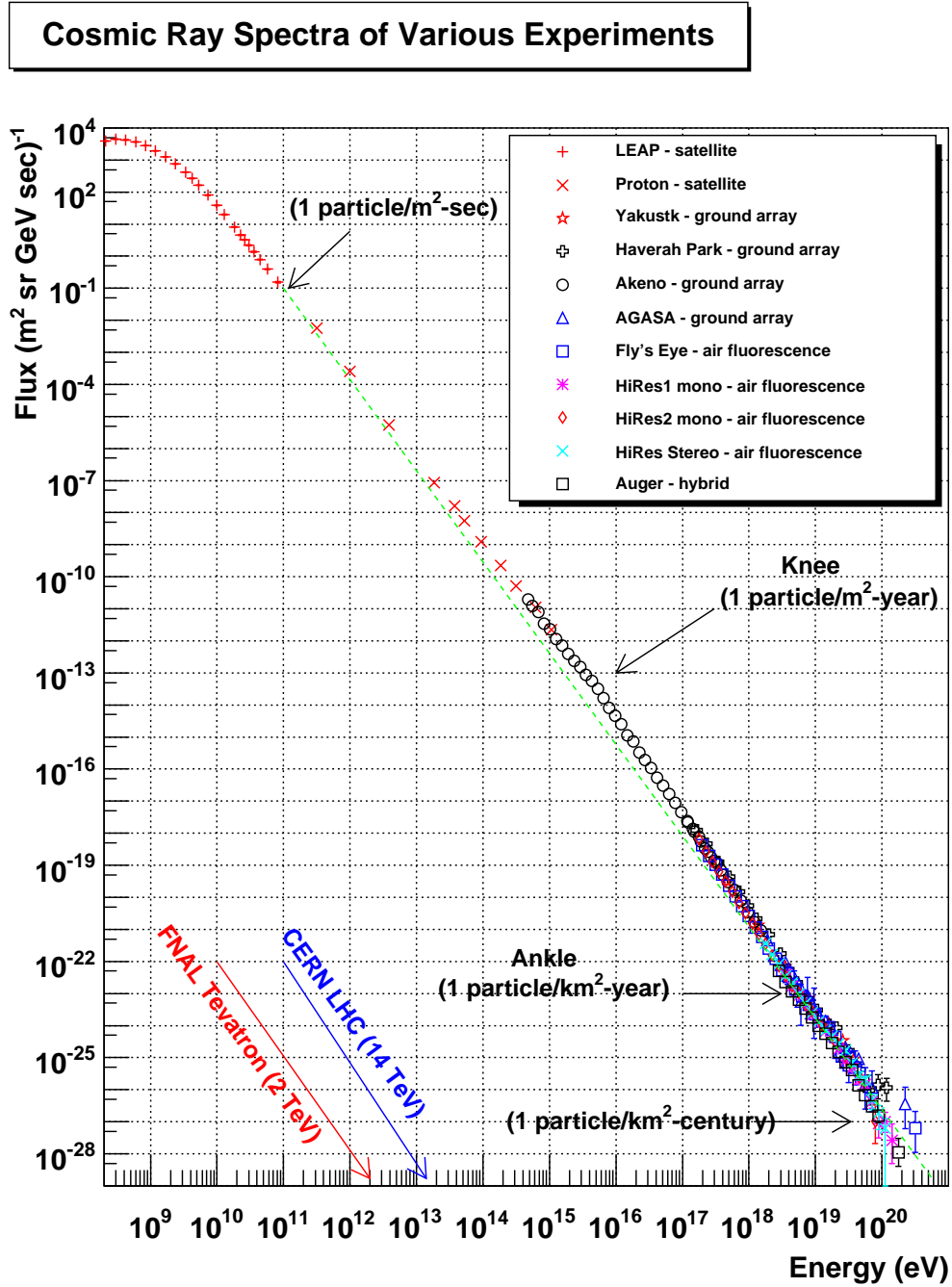
Figure 2.1: Measured Cosmic ray spectrum - From [94]

composition at the energies of the "knee" and above is difficult as fluxes become so low that satellite born experiments, measuring the cosmic rays directly, would have to be much bigger than is feasible at this time. So at these energies cosmic rays can be only observed indirectly by measuring the air-showers they produce. From the air-shower the composition can not be measured directly, but inferences from the shower development can be made, which are nevertheless difficult and involve a lot of systematic uncertainties.

At energies above $10^{19.6}$eV a suppression of the cosmic ray flux has been observed [89], which is likely to be associated with the long theorized Greisen-Zatsepin-Kuzmin (GZK) cut-off. This cut-off is predicted to arise from energy losses of the highest energetic cosmic rays in pion photon-production with the cosmic microwave background (CMB). The decay of pions produced in this process is also leading to a guaranteed flux of ultra-high energy neutrinos.

Cosmic rays arrive to the Earth almost isotropically. They are deflected in the galactic magnetic field and their direction is mostly randomized. They thus do not point back to their sources, as photons and neutrinos generally do, and this is the main reason why these sources up to today have not been unveiled by direct measurement. At the lower end of the spectrum, cosmic rays get deflected by the magnetic field of the Earth, causing the geomagnetic latitude effect. At the very highest energies, above 10^{19}eV the deflection in the galactic magnetic field becomes minor and the cosmic rays potentially point back to their sources. Due to low statistics this effect has not lead to any definite source detection yet, but first hints of anisotropies have been reported by the AUGER collaboration [19].

2.2 Cosmic ray air-showers

2.2.1 Hadronic shower phenomenology

While cosmic ray particles up to the knee can be observed directly by instruments born on balloons or satellites, the small rates of cosmic rays at higher energy imply that they have to be measured indirectly from the ground by the particle showers they produce when interacting with air nuclei in the atmosphere. The secondary particles produced in such air-showers are often referred to as cosmic rays themselves, which has historical reasons, as it was this secondary component which once lead to the discovery of cosmic rays.

The development of a cosmic ray air shower is sketched in figure 2.2. It can be divided
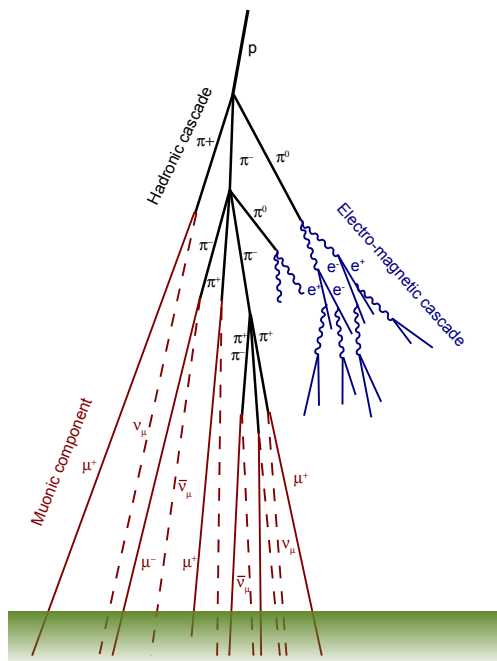
Figure 2.2: Sketch of the cosmic ray air-shower development -

into three components, namely a hadronic, an electro-magnetic and a muonic part. The interaction of the incident nuclei with air nuclei (at these energies it is effectively nucleon-nucleon interaction) produces a number of hadrons of which pions are most abundant. Nevertheless, depending on the energy carried by the interacting nucleon, also heavier hadrons such as strange or charmed mesons and baryons or anti-protons can be produced. These hadrons will, depending again on the energy, either decay or interact. In interactions with further air-nuclei they will then mostly produce more hadrons of lower energy, thus feeding a hadronic cascade.

Decay of neutral mesons, such as the π^0 or η particles will produce high energetic γ-rays. Through a series of alternate electron-positron pair-productions and Bremsstrahlung-emission these produce an independent electro-magnetic cascade, which dies out once the photon energies are not anymore sufficient for pair-production.

The decay of charged hadrons, such as $\pi^{\pm}$ and $K^{\pm}$, will produce predominately muons and muon neutrinos. This muonic component is also mostly independent of the further shower development, since neutrinos rarely interact and high energy muons will typically not decay, interact or suffer large energy losses due to ionization within the atmosphere. Therefore this component is observed relatively unchanged at the surface

13

of the Earth, while hadronic and electro-magnetic cascades die out typically far above
the sea-level.

The height of the shower maximum in terms of particle multiplicity (X_{max}) is in good
approximation proportional to the natural logarithm of the primary cosmic ray energy
E_0. The particle multiplicity itself is directly proportional to E_0. The shape of the
shower slightly depends on the sort of primary nucleus. Showers induced by heavier
elements e.g. typically evolve higher in the atmosphere. Assuming a simple superposi-
tion model, which treats an incident nucleus as a group of nucleons which all interact
independently, X_{max} becomes proportional to $\ln(E_0/A)$. Here A is the mass number
of the cosmic ray nucleus. Thus the shower maximum is shifted to greater heights.

A detailed understanding of the shower development and especially the muonic com-
ponent is essential for any experiment in neutrino astronomy. The muons produced in
the atmosphere represent the primary background to any search for neutrino induced
muons and cascades. And the corresponding atmospheric neutrinos form a typically
irreducible background to any search for extra-terrestrial neutrino signals. In this the-
sis new methods to reduce both of these backgrounds are described which are partially
based on the analytic calculations of atmospheric muon and neutrino spectra, we will
now derive.

2.2.2 Cascade equations

In this section we outline approximate analytical descriptions of particle fluxes in cosmic
ray air showers, mostly following the description as it is given in [51].

The fluxes of hadrons in the atmosphere can be described by a set of coupled transport-
or cascade-equations of the form:

$$\frac{\mathrm{d}\, H_i(E_i, X)}{\mathrm{d}\, X} = -\left(\frac{1}{\lambda_i} + \frac{1}{d_i}\right) H_i(E_i, X) + \sum_j \int \frac{F_{ji}(E_i, E_j)}{E_i} \frac{H_j(E_j)}{\lambda_j}\, \mathrm{d}\, E_j \qquad (2.2)$$

$H_i(E_i, X)\, \mathrm{d}\, E_i$ is the flux of hadrons of type i evaluated in the energy interval $E_i +$
ΔE_i and at "slant depth" X. The latter is defined as the density of the atmosphere
integrated along the path of the given particle i from the top of the atmosphere to the
evaluation point.

$$X = \int_0^{\vec{r}} \rho(h)\, \mathrm{d}\, \vec{r} \qquad \left[\frac{g}{cm^2}\right] \qquad (2.3)$$

A schematic view of X and the relation to other atmospheric length-like variables
is illustrated in figure 2.3. The first term in equation (2.2) describes the energy losses
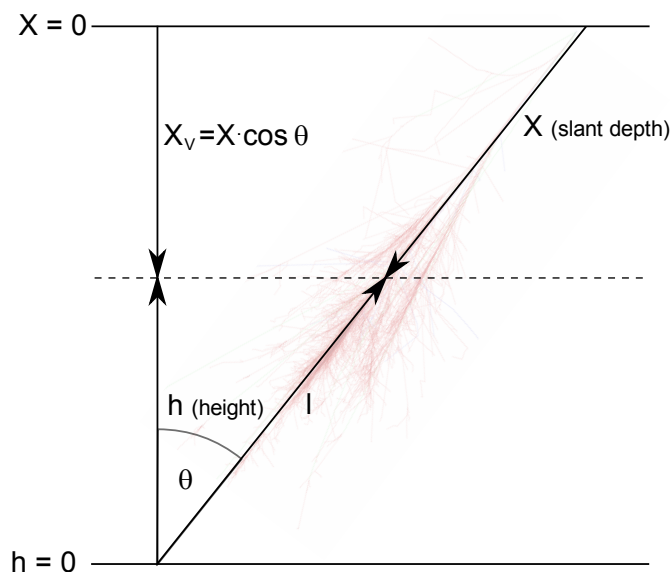
Figure 2.3: Definitions of depth variables in the Atmosphere -

to the respective hadron flux. Losses due to interaction with other particles are accounted for by the factor $1/\lambda_i$, where λ_i is the interaction length of the given hadron in the atmosphere, measured in g/cm^2. Losses by decay are described through the decay length d_i which is likewise given in g/cm^2. Both λ_i and d_i are generally dependent on the particle energy as well as the density structure of the atmosphere.

The sum of terms in equation (2.2) accordingly describes possible additions to the given hadron flux by production in interactions of other particles j with air nuclei. $F_{ij}(E_i, E_j)$ represents the (dimensionless) inclusive cross-section integrated over the transverse momentum (p_T).

Boundary conditions are necessary to relate the set of equations (2.2) to real particle fluxes. Essentially this boundary conditions are given by the incident cosmic ray nucleon flux $(H_N(E_N, 0) \equiv N_0(E))$ at the top of the atmosphere $(X = 0)$.

For comparisons of experimental results with theoretical expectations a Monte-Carlo simulation is usually the best method. Analytic evaluations of air-shower developments are difficult and typically done by restricting the equations to the most abundant particles and by applying a number of approximations. Nevertheless such solutions are good cross checks and offer the possibility to estimate new effects before running time consuming simulations. Especially for the purpose of, for the first time, estimating a veto of atmospheric neutrinos, as it will be discussed in chapter 6, such approximate solutions are appropriate. In this particular case we are especially interested in the

fluxes of pions and kaons, since the decay of these mesons predominantly gives rise to the fluxes of $\mu^{\pm}$ and ν_{μ} in the atmosphere. We therefore restrict our selves to the consideration of the fluxes of the initial nucleons ($N(E, X)$) as well as pions ($\Pi(E, X)$) and kaons ($K(E, X)$). Since the descriptions of pions and kaons are formally the same we content ourselves with evaluating the pion case, giving the kaon expression whenever it is appropriate.

The flux of pions in the atmosphere is thus described by

$$\frac{\mathrm{d}\,\Pi}{\mathrm{d}\,X} = -\left(\frac{1}{\lambda_\pi} + \frac{1}{d_\pi}\right)\Pi \quad + \int\limits_0^1 \frac{\Pi(E/x_L)F_{\pi\pi}(E_\pi, E_\pi/x_L)}{\lambda_\pi(E/x_L)}\frac{\mathrm{d}\,x_L}{x_L^2}$$
$$+ \int\limits_0^1 \frac{N(E/x_L)F_{N\pi}(E_\pi, E_\pi/x_L)}{\lambda_N(E/x_L)}\frac{\mathrm{d}\,x_L}{x_L^2} \tag{2.4}$$

Cross-coupling to other channels as well as nucleon-antinucleon production is neglected and thus the production of pions is restricted here to collisions of other pions (2nd term in equation 2.4) and nucleons (3rd term) with air nuclei. Equation 2.4 also includes a variable change from E_j to $x_L = E_i/E_j$, which simplifies the integrations especially after the following approximations are made:

$$\lambda_i(E) \rightarrow \lambda_i = \text{const.} \tag{2.5}$$
$$F_{ij}(x_L, E) \rightarrow F_{ij}(x_L) \tag{2.6}$$

These are hadronic expressions of the so called "Approximation A" which is used in electro-magnetic cascade theory. The assumption (2.6) is known as hadronic (or Feynman) scaling and is valid over a wide energy range. At very high energies, it is violated, as well as assumption (2.5), since the interaction cross-sections are not completely independent of energy.
In the given approximation the respective cascade equation for nucleons ($N(E, X)$) has an elementary solution of the form

$$N(E, X) \propto e^{-\frac{X}{\Lambda_N}} E^{-(\gamma+1)} \tag{2.7}$$

which fulfills the boundary condition for a cosmic ray power law spectrum. The attenuation length Λ_N is defined as

$$\frac{1}{\Lambda_N} = \frac{1}{\lambda_N}\left[1 - \int\limits_0^1 x_L^{\gamma-1} F_{NN}(x_L)\,\mathrm{d}\,x_L\right] \equiv \frac{1}{\lambda_N}\left[1 - Z_{NN}\right] \tag{2.8}$$

where Z_{NN} is the spectrum-weighted moment of the inclusive cross-sections

$$Z_{ij} \equiv \int\limits_0^1 x_L^{\gamma-1} F_{ij}(x_L)\,\mathrm{d}\,x_L \tag{2.9}$$

To find explicit solutions to the pion flux $\Pi(E, X)$ we have to apply further approximations. In equation (2.4) we approximate the pion flux under the integral in the second term by $\Pi(E/x_L, X) \approx f(X)\left(\frac{E}{x_L}\right)^{-(\gamma-1)}$ which leads to the simplified form

$$\frac{\mathrm{d}\,\Pi}{\mathrm{d}\,X} = -\left(\frac{1}{\Lambda_\pi} + \frac{1}{d_\pi}\right)\Pi(E, X) + \frac{Z_{N\pi}}{\lambda_N}N_0(E)e^{-\frac{X}{\Lambda_N}} \tag{2.10}$$

Thus the first term gives the attenuation of pions as a combination of interaction loss and regeneration. The second term has been evaluated using the solution for the nucleon flux (2.7).

While the decay times and cross-sections can be measured at collider experiments (although not in the whole cosmic ray energy range) the attenuation and decay lengths depend on the local density $\rho(X)$ of the atmosphere. The interaction length λ_i in air is given by

$$\lambda_i \;=\; \frac{\rho(X)}{\rho_N(X)\,\sigma_i^{air}} \;=\; \frac{A\,m_p}{\sigma_i^{air}} \tag{2.11}$$

Where $\rho_N(X)$ is the number density of nucleons in air and σ_i^{air} is the cross-section of the incident particle i with air. A is the atomic mass number of the air nuclei and m_p the proton mass.

The decay length dependence on the atmospheric density is governed by

$$\frac{1}{d_i} = \frac{1}{\rho(X)\,c\,\gamma\,\tau_i}. \tag{2.12}$$

In this case γ is the Lorentz-factor of the decaying particle in the rest-frame of the atmosphere. τ_i gives the decay time. Under the rough assumption that the atmosphere is isothermal, the pressure (given by the vertical component of the slant depth $p = X_V$) can be described by a power law with a constant scale height h_0.

$$X_V = X_0 e^{-\frac{h}{h_0}} \tag{2.13}$$

Since the density $\rho = \mathrm{d}\,X_V/\,\mathrm{d}\,h = X_V/h_0$ it follows

$$\rho \approx \frac{X_V \cos\theta}{h_0} \quad , \tag{2.14}$$

parameter	value	constraints
λ_N	$86 \ \frac{g}{cm^2}$	evaluated at $E \sim 100 \ GeV$, $A = 14.5$
λ_π	$116 \ \frac{g}{cm^2}$	evaluated at $E \sim 100 \ GeV$, $A = 14.5$
λ_K	$138 \ \frac{g}{cm^2}$	evaluated at $E \sim 100 \ GeV$, $A = 14.5$
$Z_{N\pi}$	0.079	$A = 14.5$, $\gamma = 1.7$, no η production
$Z_{\pi\pi}$	0.271	$A = 14.5$, $\gamma = 1.7$, no η production
Z_{NK}	0.0118	$A = 14.5$, $\gamma = 1.7$, no η production
Z_{KK}	0.223	$A = 14.5$, $\gamma = 1.7$, no η production
Z_{NN}	0.298	$A = 14.5$, $\gamma = 1.7$, no η production
Λ_N	$120 \ \frac{g}{cm^2}$	evaluated at $E \sim 100 \ GeV$
Λ_π	$160 \ \frac{g}{cm^2}$	evaluated at $E \sim 100 \ GeV$
Λ_K	$180 \ \frac{g}{cm^2}$	evaluated at $E \sim 100 \ GeV$
h_0	6.4 km	$X_V < 200 \frac{g}{cm^2}$
ϵ_π	115 GeV	at $h_0 = 6.4$ km
ϵ_K	850 GeV	at $h_0 = 6.4$ km

Table 2.1: Parameters guiding the transport of hadrons in air - Values taken from [51].

if the curvature of the Earth is neglected, which is a valid approximation up to zenith angles close to the horizon. Following from this and employing $\gamma = E/mc^2$, the decay length can be described as:

$$\frac{1}{d_i} = \frac{m_i h_0 c}{\tau_i E X \cos\theta} \equiv \frac{\epsilon_i}{E X \cos\theta} \tag{2.15}$$

As λ_i is approximately constant, the turnover from the regime where interaction losses dominate ($\lambda_i < d_i$) to the regime where decay losses are dominant ($d_i < \lambda_i$) depends on the ratio ϵ_i/E. Thus ϵ_i determines the critical energy below which decay is favored. With this last approximation, an exact solution to equation (2.10) is given by:

$$\Pi(E, X) = e^{-\frac{X}{\Lambda_\pi}} \frac{Z_{N\pi}}{\lambda_N} N_0(E) \int\limits_0^X \left(\frac{X'}{X}\right)^{\frac{\epsilon_\pi}{E \cos\theta}} e^{\left(\frac{X'}{\Lambda_\pi} - \frac{X'}{\Lambda_N}\right)} \mathrm{d}\,X' \tag{2.16}$$

A corresponding solution for kaons follows the same form.

The various parameters in the above given formulas are listed in table 2.1. The interaction (and thus the attenuation) lengths are evaluated in the 100 GeV energy regime. Even though these lengths get shorter at higher energies this is a good approximation

also at higher energies. The air nuclei are generalized to have mass number $A = 14.5$. The spectrum-weighted moments Z_{ij} are evaluated assuming a spectral index $\gamma = 1.7$ and neglect the production of η-mesons which becomes more important at higher energies. The scale height h_0 corresponds to the height in the atmosphere where the first few interactions typically appear. This value is also used to evaluate the critical energies $\epsilon_{\pi/K}$.

2.2.3 From mesons to neutrinos: Decay kinematics

The production spectrum of secondaries of type i in the decay of parents of type j within the atmosphere is described by

$$\mathcal{P}_i(E, X) = \sum_j \int_{E_{min}}^{E_{max}} \frac{\mathrm{d}\, n_{ij}(E, E')}{\mathrm{d}\, E} \mathcal{D}_j(E', X)\, \mathrm{d}\, E' \tag{2.17}$$

The function $\mathcal{D}_j(E', X)$ gives the component of the parent spectrum which actually decays. For pions it is given by

$$\mathcal{D}_\pi(E, X) = \frac{\epsilon_\pi}{E\, X\, \cos\theta} \Pi(E, X) \tag{2.18}$$

within the approximations that have been applied in the derivation of equation 2.15. $\frac{\mathrm{d}\, n_{ij}(E, E')}{\mathrm{d}\, E}$ is the inclusive spectrum of secondaries i with energy E which arises from decay of parents j with energy E'. As well as the integral limits in equation (2.17), it is determined by the kinematics of the decay, which will be discussed in the following.

As ultimately we are interested in the production spectra of neutrinos and muons and these arise predominantly from the decay of pions and kaons, we focus here on the kinematics of the respective two-body decays $\pi^\pm \to \mu^\pm \nu_\mu (\bar{\nu}_\mu)$ and $K^\pm \to \mu^\pm \nu_\mu (\bar{\nu}_\mu)$. In the rest frame of the parent meson the muon and the neutrino are emitted back-to-back and their energies are given by

$$
\begin{aligned}
E_\mu^{cm} &\simeq \frac{m_i}{2} \left(1 + r_i\right) \\
E_\nu^{cm} &\simeq \frac{m_i}{2} \left(1 - r_i\right) = |p^{cm}|
\end{aligned}
\tag{2.19}
$$

With $c = 1$ and $r_i = m_\mu^2/m_i^2$, which gives the quadratic mass ratio of the muon relative to the parent meson. Also we neglect the neutrino mass and neutrino oscillations. The
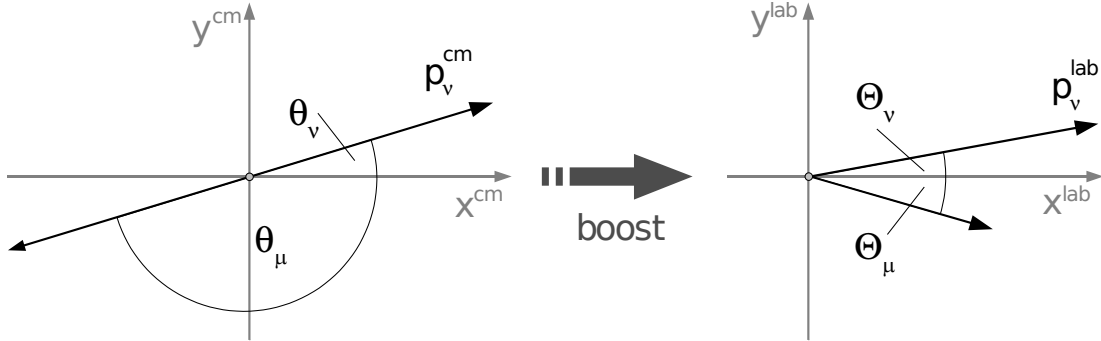
Figure 2.4: Two body decay of the parent meson into muon and neutrino. - The left figure displays the back-to-back kinematics in the meson center of mass (cm) frame. The right figure shows the momenta after Lorentz transformation into the laboratory frame.

respective values of r_i for pions and kaons are $r_\pi \approx 0.573$ and $r_K \approx 0.046$.

Thus the energy is almost equally shared between muon and neutrino in the kaon decay, but in the case of the pion decay the energy balance is shifted strongly towards the muon since its mass is comparable to that of the pion. Anyhow, within the center-of-mass (cm) system the muon energy will always be larger then the energy of the neutrino.

When transferring from the cm-frame into the rest-frame of the Earth (laboratory (lab)-frame) the energies of the muon and the neutrino are determined by Lorentz-transformation. If we define the positive x-direction along the direction of the boost, then

$$E_\nu = \gamma \, E_\nu^{cm} + \beta \, \gamma \, p_{x\nu}^{cm}$$
$$E_\mu = \gamma \, E_\mu^{cm} + \beta \, \gamma \, p_{x\mu}^{cm} \quad , \tag{2.20}$$

where γ and β are the Lorentz-factor and speed of the parent meson. As the back-to-back emission can occur in all directions, with respect to the boost direction, the angle θ_ν (see figure 2.4) between the boost- and the neutrino direction in the cm-frame strongly influences the relation of muon to neutrino energies in the laboratory frame. From

$$p_{x\nu}^{cm} = |p^{cm}| \cos\theta_\nu \qquad \text{and}$$
$$p_{x\mu}^{cm} = |p^{cm}| \cos(\theta_\nu - \pi) = -|p^{cm}| \cos\theta_\nu, \tag{2.21}$$

and the relativistic approximation $\beta \to 1$, which is valid for pion and kaon energies

above a few GeV, we can rewrite equation (2.20) as

$$E_\nu = \gamma|p^{cm}|(1 + \cos\theta_\nu)$$

$$\text{and} \qquad E_\mu = \gamma|p^{cm}|\left(\frac{1 + r_i}{1 - r_i} - \cos\theta_\nu\right). \tag{2.22}$$

The lowest possible muon energy (and highest neutrino energy) will occur when the muon goes in the opposite direction of the boost ($\cos\theta_\nu = 1$) and vice versa. Thus their energies are limited by

$$r_i E \leq E_\mu \leq E \qquad \text{and}$$

$$0 \leq E_\nu \leq (1 - r_i) E \tag{2.23}$$

which implies

$$E_\nu \frac{r_i}{1 - r_i} \leq E_\mu \tag{2.24}$$

The strong dependence on the parameter r_i leads to a quite different kinematic behavior for pions and kaons. For the pion case the muon energy will always be larger then the neutrino energy, even in the lab-frame ($r_\pi/(1 - r_\pi) = 1.342$). On the other hand the muon energy can be as low as 5% of the neutrino energy in the case of kaon decay ($r_K/(1 - r_K) = 0.048$).

The distributions $\frac{\mathrm{d}n}{\mathrm{d}E_\nu}$ and $\frac{\mathrm{d}n}{\mathrm{d}E_\mu}$ of the muon and neutrino energies in the lab-frame are flat within the limits given in equation (2.23). This follows from the isotropic decay directions (in the absence of polarization) in the cm-frame, where

$$\frac{\mathrm{d}n}{\mathrm{d}\Omega} = \frac{\mathrm{d}n}{2\pi\,\mathrm{d}\cos\theta} = \text{const.} \tag{2.25}$$

and from the Lorentz-transformation (equation 2.20)). $E_{\nu/\mu} \propto \cos\theta$ implies that also $\frac{\mathrm{d}n}{\mathrm{d}E} = \text{const.}$ By normalization over the allowed energy range one gets

$$\frac{\mathrm{d}n_{ij}}{\mathrm{d}E} = \frac{\text{const.}}{E_j(1 - r_j)} \tag{2.26}$$

which is valid for muons and neutrinos alike.

Another important aspect of the meson decay kinematics is the opening angle between the muon and the neutrino in the lab-frame. From the momentum components the respective angles for muon and neutrino to the boost direction can be derived as

$$\tan\Theta_\nu = \frac{\sin\theta_\nu}{\gamma(\cos\theta_\nu + 1)} \qquad \text{and}$$

$$\tan\Theta_\mu = \frac{\sin\theta_\nu}{\gamma\left(\cos\theta_\nu - \frac{1 - r_j}{1 + r_j}\right)} \tag{2.27}$$

Thus the opening angle between the muon and the neutrino is given by the sum $\Theta_\nu + \Theta_\mu$. This angle gets smaller (on average) when the meson energy rises and at sufficiently high energy the muon and neutrino traverse the atmosphere quasi aligned. This is illustrated in figure 2.5. It shows the distance of muon and neutrino at the surface in dependence of the cms-frame angle θ_ν, assuming a typical interaction height of 10 km. The solid red curves show the result for pions of different energies, while the dashed green curves give the distances for kaon decays.
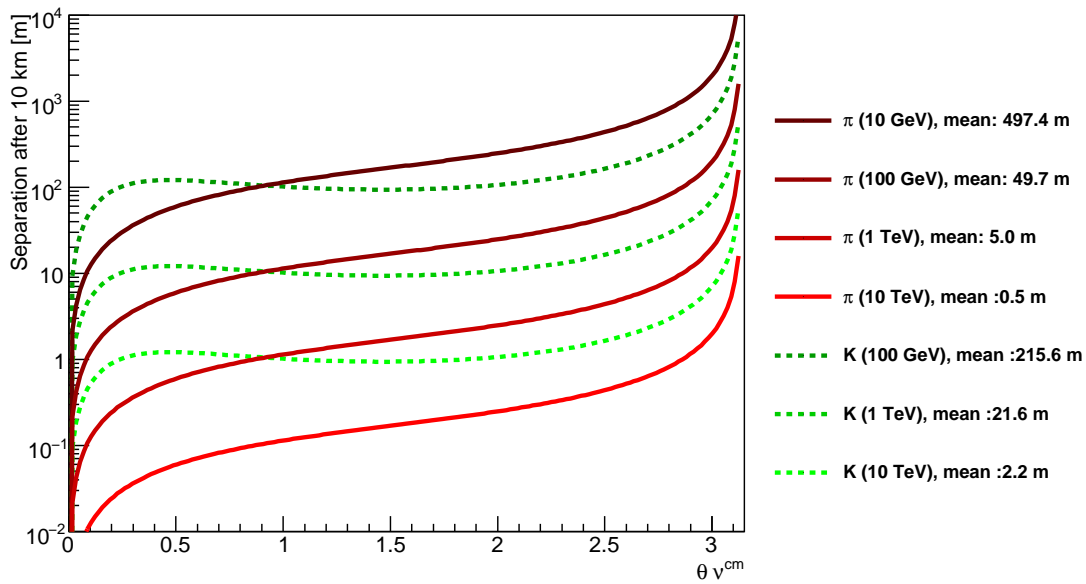
Figure 2.5: Distance of muon and neutrino 10 km after meson decay - The distance is shown in dependence of the neutrino angle w. r. t. the boost direction in the cms-frame θ_ν. The solid red curves represent the distances for decays of pions of 10 GeV to 10 TeV, the dashed green curves show the distances for kaon decays of 100 GeV to 10 TeV.

The close proximity of the atmospheric neutrino and its partner muon gave rise to the idea of the atmospheric neutrino veto, as discussed in detail in chapter 6.

It should be noted that while the muon will always move in the forward direction of the parent meson, the neutrino can principally escape in the opposite direction, leading to an infinite distance.

2.2.4 Muon and neutrino spectra in the atmosphere

From the production spectrum of secondaries i (equation (2.17)) and the kinematics discussed in the previous section, we can specify the production spectra of muons and

neutrinos from the two-body decays of pions and kaons:

$$\mathcal{P}_i(E_i, X) =$$

$$\int\limits_{E_{\pi,\mathrm{min}}}^{E_{\pi,\mathrm{max}}} \left[\frac{B_{\pi \to \mu\nu}}{E\,(1 - r_\pi)} \right] \left\{ \frac{\epsilon_\pi}{E\,X\,\cos(\theta)} \right\} \Pi(E, X)\,\mathrm{d}E$$

$$+ \int\limits_{E_{K,\mathrm{min}}}^{E_{K,\mathrm{max}}} \left[\frac{B_{K \to \mu\nu}}{E\,(1 - r_K)} \right] \left\{ \frac{\epsilon_K}{E\,X\,\cos(\theta)} \right\} K(E, X)\,\mathrm{d}E. \tag{2.28}$$

Where $i = \mu, \nu_\mu$. The branching ratios $B_{K/\pi \to \mu\nu}$ give the fraction of the parent mesons that decay via the discussed two-body decays. While $B_{\pi \to \mu\nu}$ can be safely approximated as 1, $B_{K \to \mu\nu}$ is smaller, at $\approx 63.4\%$. From equation (2.28) it is clear that the muon and neutrino spectra are determined exclusively through the integral borders which can be derived easily from equation (2.23) as

$$\begin{aligned} E_\mu &\leq E_j \leq \frac{E_\mu}{r_j} \qquad \text{and} \\ \frac{E_\nu}{1 - r_j} &\leq E_j \leq \infty \qquad (j = \pi, K) \end{aligned} \tag{2.29}$$

When the energy is high enough that muon decay and energy loss in the atmosphere can be neglected, the muon, resp. neutrino flux at the Earths surface (after full shower development) is given by integrating the production spectrum over the whole atmosphere up to X. But since showers usually develop high in the atmosphere ($X \gg \Lambda_j$) the integral can be extended to infinity :

$$\phi_i(E) = \int\limits_0^\infty \mathcal{P}_i(E, X)\,dX \tag{2.30}$$

Using the approximate solutions for the pion, resp. kaon flux found in the previous section (equation 2.16) this equation can be written as

$$\phi_{ij}(E_i) = N_0(E_i) Z_{Nj} \frac{\Lambda_j}{\lambda_N} \frac{\xi_j(E_i)}{1 - r_j} \times \int\limits_{z_{ij,min}}^{z_{ij,max}} \frac{\mathrm{d}z}{z^{\gamma+2}}$$

$$\left[\frac{1}{z + \xi_j(E_i)} - \frac{\Lambda_j/\Lambda_N - 1}{2z + \xi_j(E_i)} + \frac{(\Lambda_j/\Lambda_N - 1)^2}{3z + \xi_j(E_i)} + \ldots \right] \quad,$$

$$(i = \mu, \nu), (j = \pi, K) \tag{2.31}$$

The integration variable has been changed to $z = E_j/E_i$ which (from equations (2.29)) leads to the integral borders

$$
\begin{aligned}
1 &\leq z_\mu \leq \frac{1}{r_j} && \text{and} \\
\frac{1}{1-r_j} &\leq z_\nu \leq \infty && (j = \pi, K)
\end{aligned}
\tag{2.32}
$$

Furthermore we define $\xi_j(E_i) = \frac{\epsilon_j}{E_i \cos\theta}$. The remaining integral in equation (2.31) can be solved analytically in a high and a low energy approximation ($\epsilon_j \ll E_i$ and $\epsilon_j \gg E_i$, respectively). In case of very high energy $\xi_j(E_i)$ becomes very small and can be neglected in the denominators within the integral of equation (2.31). The high energy solution thus becomes:

$$
\begin{aligned}
\phi_{ij}^{high}(E_i) =\ & N_0(E_i)\frac{Z_{Nj}}{\gamma+2}\frac{\Lambda_j}{\lambda_N}\frac{\Lambda_j}{\Lambda_j-\Lambda_N}\ln\frac{\Lambda_j}{\Lambda_N}\frac{\xi_j(E_i)}{1-r_j}\left[z^{-(\gamma+2)}\right]_{z_{ij,max}}^{z_{ij,min}} \\
& \text{with} \qquad\qquad (i = \mu, \nu), (j = \pi, K)
\end{aligned}
\tag{2.33}
$$

Similarly, the low energy approximation leads to $\xi_j(E_i)$ becoming very large and thus the z-dependence in the denominators can be neglected, leading to

$$
\begin{aligned}
\phi_{ij}^{low}(E_i) =\ & N_0(E_i)\frac{Z_{Nj}}{\gamma+1}\frac{\Lambda_j}{\lambda_N}\frac{1}{1-r_j}\left[z^{-(\gamma+1)}\right]_{z_{ij,max}}^{z_{ij,min}} \\
& \text{with} \qquad\qquad (i = \mu, \nu), (j = \pi, K)
\end{aligned}
\tag{2.34}
$$

This approximations reflect the regimes where meson decay dominates (low energy) and where interaction dominates (high energy). The spectral index in the low energy case ($\gamma + 1$) is smaller then in the high energy solution ($\gamma + 2$), which describes the characteristic steepening in the observed atmospheric muon and neutrino spectra from a spectral index ≈ 2.7 to ≈ 3.7.

Both approximate solutions can be combined to a single solution by following the simple Ansatz

$$
\frac{1}{\phi} = \frac{1}{\phi_{low}} + \frac{1}{\phi_{high}}
\tag{2.35}
$$

which leads to

$$
\begin{aligned}
\phi_{ij}(E_i) &= N_0(E_i)\frac{\Lambda_N}{\lambda_N}\left(\frac{A_{ij}}{1 + B_{ij}\xi_j^{-1}(E_i)}\right) \\
\text{with}\quad A_{ij} &= Z_{Nj}(1-r_j)^{-1}(\gamma+1)^{-1}\left[z^{-(\gamma+1)}\right]_{z_{ij,max}}^{z_{ij,min}} \\
\text{and}\quad B_{ij} &= \frac{\gamma+2}{\gamma+1}\frac{\left[z^{-(\gamma+1)}\right]_{z_{ij,max}}^{z_{ij,min}}}{\left[z^{-(\gamma+2)}\right]_{z_{ij,max}}^{z_{ij,min}}}\frac{\Lambda_j-\Lambda_N}{\Lambda_j \ln\frac{\Lambda_j}{\Lambda_N}}
\end{aligned}
\tag{2.36}
$$

Assuming an initial flux of cosmic rays given by a power law spectrum $N_0(E) \approx 1.8 \cdot E^{-2.7} \frac{\text{nucleons}}{\text{cm}^2\,\text{sr}\,\text{s}\,\text{GeV}}$, which is evaluated at the respective particle energy, and employing the parameter values given in table 2.1, we can write the spectra of muons and neutrinos in the atmosphere explicitly as

$$\phi_\nu(E_\nu) = \frac{0.02 \cdot E^{-2.7}}{\text{cm}^2\,\text{s}\,\text{sr}\,\text{GeV}} \left\{ \frac{1}{1 + \frac{2.79 \cdot E_\nu\,\cos\theta}{115\,\text{GeV}}} + \frac{0.37}{1 + \frac{1.18 \cdot E_\nu\,\cos\theta}{850\,\text{GeV}}} \right\} \tag{2.37}$$

and

$$\phi_\mu(E_\mu) = \frac{0.14 \cdot E^{-2.7}}{\text{cm}^2\,\text{s}\,\text{sr}\,\text{GeV}} \left\{ \frac{1}{1 + \frac{1.06 \cdot E_\mu\,\cos\theta}{115\,\text{GeV}}} + \frac{0.55}{1 + \frac{1.13 \cdot E_\mu\,\cos\theta}{850\,\text{GeV}}} \right\} . \tag{2.38}$$

These spectra are shown in figure (2.6). Each of these spectra is evaluated at the respective particle energy. The steepening of the muon and neutrino spectra following the dominance of interaction over decay is clearly visible. This steepening occurs at higher energies for the muons, which reflects the kinematic fact, that the muon will on average take away more energy from the parent decay then the neutrino.
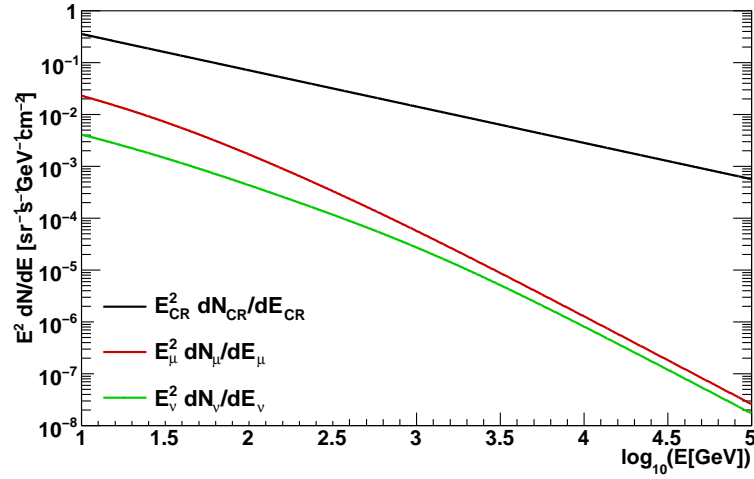
Figure 2.6: Cosmic ray (proton), muon and neutrino spectra - The analytically calculated spectra of muons (red) and neutrinos (green) from air-showers are shown together with the assumed initial cosmic ray spectrum (black) of the form $\frac{\text{d}\,N(E)}{\text{d}\,E} = E^{-2.7}$. This result was obtained from equations (2.37) and (2.38).

2.3 Sources of cosmic rays

It has already been stressed, that the sources of high energy cosmic rays are yet unknown. Nevertheless, there is a number of restrictions on the properties of potential sources and only few categories of sources are realistic candidates.

A first argument has already been mentioned in the discussion of the cosmic ray spectrum. The interpretation of the "knee" as a change of composition due to leakage of CR out of the galaxy suggests a galactic origin to the bulk of CR. Only at the highest energies above the "ankle" extra-galactic sources dominate.

The first order Fermi acceleration process in shock waves (see 2.3.2) suggests supernova remnants (SNR) as promising source candidates [23]. A simple energetic estimation supports this theory. If SNR were the primary sources of CR, their energy output must be in agreement with the observed energy density of cosmic rays of $\sim 1\text{eV/cm}^3$. This density requires a luminosity of roughly $\mathcal{L}_{CR} \sim 10^{40}\text{erg/s}$, assuming a CR residence time in the galaxy of $\sim 10^6\text{yr}$. The energy output of SNR can be estimated as $\sim 10^{42}\text{erg/s}$ (assuming a mass outflow of $10\text{M}_\odot$ and a SN rate of 1 per 30 years). Thus if the CR acceleration in SNR would be $\mathcal{O}(0.01)$ efficient they could be responsible for the bulk of accelerated CR.

Another general argument on the possible types of CR accelerators was illustrated by
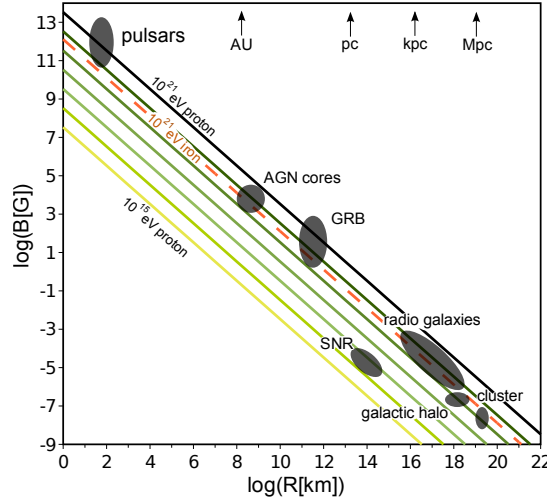
Figure 2.7: Hillas Plot - Magnetic field strength vs. size for several candidate objects of cosmic ray sources. Solid black line indicates minimum configuration to reach 10^{20}eV .

Hillas in 1984 [61]. The Larmor-radius $R_L = \frac{E}{Z\,e\,B}$ of accelerated particles sets the minimal size of the accelerating region, if we assume a gradual (stochastic) accelera-

tion process. Figure 2.7 shows a Hillas plot in which the magnetic field $\mathbf{B}$ and the size $\mathbf{R}_s$ of several potential CR accelerators are plotted against each other logarithmically. The solid lines mark the minimal configurations needed to reach energies from 10^{15}eV to 10^{21}eV for protons ($Z = 1$) and the dashed line for $E_{max} = 10^{21}$eV and iron ($Z = 26$). Relatively small objects, such as pulsars, which principally have the necessary magnetic fields, have inherent problems of energy losses due to radiation in the magnetic fields and collisions in the dense environment. Very large objects on the other hand, such as galaxy clusters, lead to extremely long acceleration times. Thus "medium sized" objects, such as the cores of active galactic nuclei (AGN), gamma ray bursts (GRB) or SNR are favored. Although this arguments make SNR unlikely to be the source of the ultra high energy CR (UHECR) these objects could still be responsible for CR acceleration up to the knee (10^{15}eV). AGN are generally held to be prime candidates for UHECR sources also because of another argument. The field strength required to accelerate UHECR up to 10^{20}eV is $\sim 10^{20}$ V. Assuming the impedance of vacuum ($\sim 380\ \Omega$) we get a minimal power to be dissipated by a potential accelerator of $P = U^2/R \gtrsim 10^{44}$erg/s. The observed intensity of UHECR then sets an upper limit on the density of their sources ρ_S within the universe. One finds $\rho_S \lesssim 10^{-3}/\text{Mpc}^3$ which excludes usual galaxies, but fits the density of the most common AGN, Seyfert galaxies (AGN with relatively weak radio emission).

2.3.1 Potential source classes

Potential sources of CR can generally be divided in sources within our own galaxy and extra-galactic sources.

2.3.1.1 Galactic sources

- **Supernovae (SN) and supernova remnants (SNR):** When massive stars reach the end of their fusion process their core is completely fused to iron and no further energy releasing processes are possible. With the radiation pressure gone, the outer shells drop in on the core, rapidly increasing its pressure. Eventually free electrons get forced to interact with the protons to form neutrons via inverse β-decay: $p + e^- \rightarrow n + \nu_e$. Thus a neutron star (NS) or potentially even a black hole (BH) forms. Once the density in the core reaches nuclear densities, compression stops and the core stiffens. In-falling matter from the outer shell then gets reflected and finally blasted away from the core in a supernova explosion. This is generally the case for stars of M $> 5 - 8$ M$_\odot$ and is called a core-collapse

or Type II supernova. The largest amount of the emitted energy is taken away by thermal neutrinos from the core (99%). These neutrinos have typically low energies of a few 10 MeV. The out-moving shock wave can potentially accelerate particles, as will be shown in the next section. The maximum energy reachable by Fermi acceleration in SNR depends on the charge of the particle and is roughly Z·100 TeV. This limit is mainly a consequence of the limited free expansion time of the shock front, which is $\sim 1000 \, yr$.

- **X-ray binaries:** A binary system of a compact object (NS or BH) with a massive companion star is called a high mass x-ray binary (HMXB, as compared to low-mass x-ray binary (LMXB), where the companion is less massive) if accretion of mass from the massive star on to the compact object takes place and thermal x-rays emission from the accretion disc can be observed. If this accretion leads to formation of relativistic jets, flowing out perpendicular to the accretion disc, one usually refers to the system as "micro-quasar" (μQSO). These objects mimic many properties of quasars on much smaller scales. Many μQSO show a strong timing variability in the x-ray which is associated to emissions in radio and infra-red wavelengths from the emitted jet. Acceleration of CR is thought possible in these jets and neutrino emission in the TeV region has been predicted [72].

2.3.1.2 Extra-galactic sources

- **Active galactic nuclei (AGN):** AGN are typically located at the center of very luminous galaxies. A super massive black hole (SMBH, $M > 10^8 M_\odot$) in the very center is surrounded by an accretion disc which feeds the SMBH. Eventually a mass outflow in the form of relativistic jets is observed perpendicular to the accretion disc. Around the accretion disc a toroidal gas cloud supports the accretion with matter. Depending on the orientation of the AGN axis towards an observer the measured spectra lead to a different classification of objects. In the unified scheme of AGN they are interpreted of being of the above described constitution. Flat spectrum radio quasars and BL Lacertae objects have jets aligned to the line of sight, which makes them prime candidates in the search for neutrinos from interactions of CR accelerated in the jets.

- **Gamma ray bursts (GRB):** GRBs are short, extremely luminous flashes of gamma radiation which occur in other galaxies. They are generally divided into two types, short and long GRBs, according to their duration. Short GRB last less than two seconds and are theorized to be associated with a merging of two

binary neutron stars. Long GRB have longer durations and show a clear afterglow in x-ray and optical wavelengths. They are thought to be associated with core collapse supernovae of high mass stars.

The energy output of GRBs is enormous and can only be understood under the assumption of a beamed emission. First estimates of neutrino fluxes from GRBs have been calculated in [90].

2.3.2 Fermi acceleration

The first suggestion on the kind of process that could accelerate nuclei to energies as high as observed in cosmic rays was made by Enrico Fermi in 1949 [46]. He suggested that collision-less scattering of charged particles on magnetized clouds could provide a net acceleration. The magnetic field lines in such large magnetic fields are bound to matter and thus relatively stable over time. For statistical reasons more head-on then head-tail collisions between these clouds and cosmic rays occur, leading to an average energy gain per collision of

$$\frac{\Delta E_k}{E_k} \approx \frac{4}{3}\beta^2 \tag{2.39}$$

where β gives the speed of the scattering with respect to the laboratory system. As can be seen from equation (2.39) this process is of second order in β and it is doubtful if it can ever lead to the high energies observed in cosmic rays.

A more efficient process is the acceleration at shock fronts as outlined by A. Bell [10]. This process leads to an energy gain in first order and is generally believed to be the main mechanism of cosmic ray acceleration at least up to the knee. Figure 2.8 illustrates this first order Fermi acceleration in the rest-frame of the shock front. This shock front is assumed plane and moving at a super-sonic speed $|u_1| \gg c_s$ where c_s is the sound-speed in the gas the shock runs through. The gas in front of the shock (up-stream) moves in on the front at the said speed u_1, while the shocked gas behind (down-stream) moves away at a reduced speed u_2 (in other words, in the rest-frame of the unshocked gas, the shocked gas gets accelerated in the shock direction). Now consider a relativistic ($E \gg m$) particle of energy E_k in the unshocked region. It will be overtaken by the shock front, crossing to the down-stream region under an angle $\theta_{1,k}$. There, its direction will be isotropized by elastic scattering from the irregular magnetic fields in the turbulent wake behind the shock. Its energy is transformed to
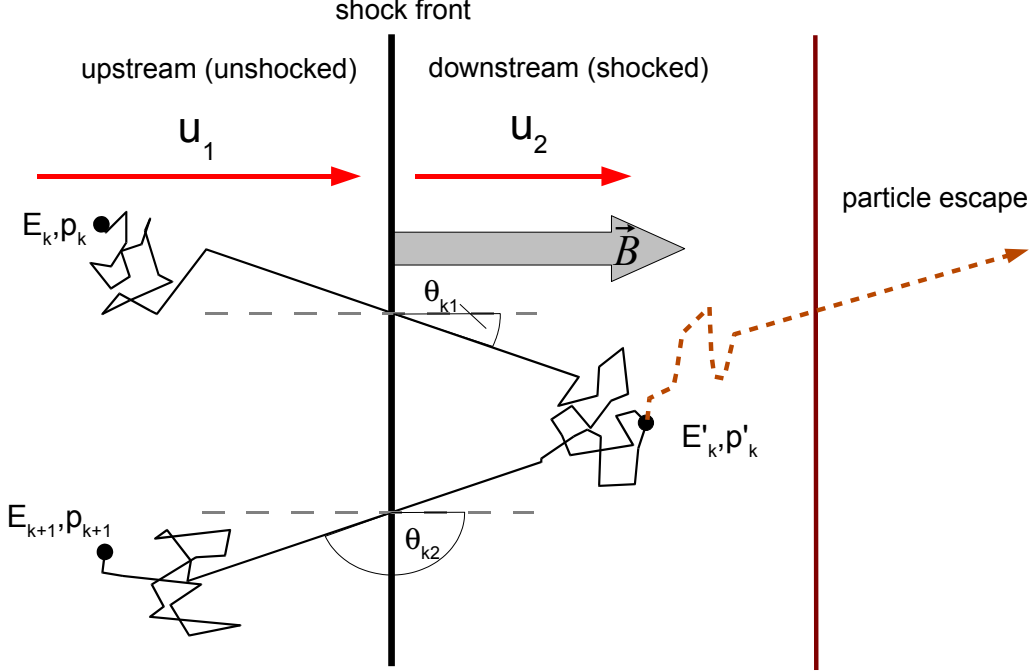
Figure 2.8: Acceleration process in super-sonic shock-fronts - Schematic view.

the rest-frame of the shocked gas via Lorentz-Transformation:

$$E'_k = \gamma \, E_k (1 \; + \; \beta \; \cos\theta_{1,k}) \tag{2.40}$$

β in this case is the shock speed $\beta \; = \; u_1 \; - \; u_2$ (note that we use $c \; = \; 1$). As the particle direction is isotropized the particle will eventually cross the shock-front again, under an angle $\theta_{2,k}$, returning in the unshocked region. The corresponding Lorentz-Transformation of the energy gives

$$E_{k+1} = \gamma \, E'_k (1 \; - \; \beta \; \cos\theta'_{2,k}). \tag{2.41}$$

Thus there is a net energy gain of

$$\frac{\Delta E_k}{E_k} \quad = \frac{1+\beta\cos\theta_{1,k}}{1+\beta\cos\theta_{2,k}} - 1. \tag{2.42}$$

To get the average energy gain we have to average over all angles, which in case of a plane shock-front gives $\langle\cos\theta_{1,k}\rangle = -\langle\cos\theta_{2,k}\rangle = \frac{2}{3}$. Thus we get

$$\frac{\Delta E_k}{E_k} = \frac{4}{3}\beta \equiv \xi \tag{2.43}$$

if the shock is not relativistic ($\beta \ll 1$). Note that this result is of first order in β. If this process is repeated k times then

$$E_k = E_0 (1 - \xi)^k \tag{2.44}$$

This acceleration process continues until the particle eventually escapes in the down-stream region. The probability to escape P_{esc} is given as the ratio of the escaping flux ϕ_{esc} and the total flux of particles crossing the shock-front to the down-stream region, ϕ_{tot}. The former is given by $\phi_{esc} = \mathcal{N} \cdot u_1$, where $\mathcal{N}$ is the number density of particles behind the shock. The latter is given by

$$\phi_{tot} = \int\limits_0^1 \mathrm{d}\cos\theta \int\limits_0^{2\pi} \mathrm{d}\phi \frac{\mathcal{N}}{4\pi} \cos\theta = \frac{\mathcal{N}}{4} \tag{2.45}$$

Thus the probability of escape is

$$P_{esc} = 4 \cdot u_2. \tag{2.46}$$

The number of particles that repeat the described acceleration cycle at least k times is

$$N(\geq E_k) \propto \sum\limits_{m=k}^{\infty} (1 - P_{esc})^m = \frac{(1 - P_{esc})^k}{P_{esc}} \tag{2.47}$$

By rearranging equation (2.43) we can derive k which, combined with equation (2.47), finally leads to a power law:

$$N(\geq E_k) \propto \frac{1}{P_{esc}} \cdot \left(\frac{E_k}{E_0}\right)^{-\gamma} \tag{2.48}$$

The spectral index γ is given by

$$\gamma = \frac{\ln\left(\frac{1}{1-P_{esc}}\right)}{\ln(1+\xi)} \approx \frac{P_{esc}}{\xi} = \frac{3}{\frac{u_1}{u_2} - 1} \tag{2.49}$$

For a strong shock u_1 is approximately $4 \cdot u_2$ which gives $\gamma = 1$. It is remarkable that this is rather close to the observed spectral index of cosmic rays, once it has been corrected for the effects of propagation.

2.4 Indirect observations of cosmic ray sources

Cosmic rays do not point back to their sources due to the galactic magnetic field, but accelerated charged particles may leave traces at their acceleration sites. Close to the

source the cosmic ray flux is highest and this may lead to a significant production of secondary particles in interactions with ambient matter or photon fields. The nucleon-nucleon interactions are similar to that discussed in air-showers:

$$p \; + \; N \; \rightarrow \; \pi^{\pm} \; + \; \pi^0 \; + \; K^{\pm} \; + \; K^0 \; + \; \eta \; + \; ... \tag{2.50}$$

while the nucleon-γ interactions lead to π production through the Δ^+-resonance:

$$p \; + \; \gamma \; \rightarrow \; \Delta^+ \rightarrow \; \pi^+ \; + \; n$$
$$p \; + \; \gamma \; \rightarrow \; \Delta^+ \rightarrow \; \pi^0 \; + \; p. \tag{2.51}$$

Under the assumption that the density in the ambient matter is low (i.e. much lower than in the Earths atmosphere) we can neglect interactions of secondaries. Thus all charged pions decay as well as the subsequent muons:

$$\pi^{\pm} \; \rightarrow \quad \mu^{\pm} \quad + \nu_{\mu}$$
$$\downarrow$$
$$\mu^{\pm} \quad \rightarrow \; e^{\pm} \; \nu_e \; \nu_{\mu} \tag{2.52}$$

This also implies that the neutrino spectra will be dominated by ν from pion decay at all energies. The neutrinos produced in the pion decay chain have the flavor-ratio $(\nu_e + \bar{\nu}_e):(\nu_{\mu} + \bar{\nu}_{\mu}):(\nu_{\tau} + \bar{\nu}_{\tau}) = 1 : 2 : 0$, which may change at high energies ($E_{\nu} \gg 100 \mathrm{TeV}$) if free pion and muon decay get suppressed in dense sources [69]. Such a change in the flavor ratio will also go along with a change in the neutrino spectrum for the same reasons as discussed for air-showers (section 2.2.4).

The neutral secondaries π^0 and η will decay in almost all cases finally producing mostly γ-rays:

$$\pi^0 \quad \rightarrow \; 2\,\gamma \qquad\qquad (98.8\%)$$
$$\eta \quad \rightarrow \; 2\,\gamma \qquad\qquad (39.3\%)$$
$$\eta \quad \rightarrow \; 3\,\pi^0 \qquad\qquad (32.6\%) \tag{2.53}$$

The spectrum of these γ-rays will have the same spectral shape as the spectrum of their decaying parents.

The neutral γ-rays and neutrinos produced in these hadronic interactions provide a signal that may be measurable at Earth, thus revealing the cosmic ray acceleration sites.

2.4.1 Gamma-ray astronomy

High energy γ-rays ($\sim 30\text{GeV} < E_\gamma <\sim 300\text{TeV}$) are observed at the Earth by imaging air Čerenkov telescopes (IACT), such as VERITAS [75], MAGIC [8] and H.E.S.S. [29]. Up to today $\sim$100 extended or point like sources have been detected, of which most are located within the galactic plane. Spectra have been measured for most of these sources and compared to models of γ-ray production. However, the interpretation of these studies are not unambiguous in terms of the question of cosmic ray origin. There are also other processes that produce γ-rays without the need of accelerated nuclei. The most prominent of these is the "inverse Compton" process in which an accelerated electron up-scatters a low energy photon up to γ-ray energies. In the "synchrotron self-Compton" model (SSC) the low energy photons are provided by synchrotron radiation of the same electron population, while "external Compton" models (EC) have the photons provided by the nearby source.
Nevertheless the spectral shape of the observed γ-ray spectra together with observations at other wavelengths (radio, infra-red, x-ray,...) may give hints on the production process, even though they have not yet been conclusive.

2.4.2 Neutrino astronomy

The unknown origin of cosmic rays and the ambiguity of the production mechanisms of γ-rays mark the central motivation for neutrino astronomy. Neutrinos are unambiguous traces of hadronic interactions and an observation of a neutrino point source in the TeV energy regime would be a "smoking gun" of cosmic ray acceleration. The extremely low cross-sections of neutrinos make them very hard to detect, but on the other hand this makes them practically unaltered messengers carrying information on the heart of their production sites. The methods of neutrino astronomy by the means of water or ice Čerenkov detectors is introduced in chapter 3.
The flux of neutrinos from cosmic ray sources depends strongly on the density of the ambient matter and photon field in the source. These properties are very hard to assess, but eventually, in some specific cases, observed γ-ray spectra can provide an upper limit on expected neutrino fluxes, as we will show now.

2.4.3 Connection between the gamma-ray and neutrino spectra

The spectra of secondaries in nucleon-nucleon interactions are typically calculated using Monte-Carlo methods [78]. But for the purposes of understanding the relation between γ-ray and ν spectra and eventually deducing the latter from the former, it is much

more practicable to make use of parametrizations. Such parametrizations of secondary spectra are presented by Kelner et al. for proton-proton (p-p) interactions in [71] and for proton-γ (p-γ) interactions in [70]. We summarize here their results for p-p interaction.

The authors deduce the spectra of γ-rays, ν_μ and electrons from parametrizations they found for secondary meson spectra in p-p collisions simulated by the publicly available SYBILL code [48]. They take into account the γ-ray flux from the decays of π^0 and η mesons given in equation (2.53). The η decays contribute significantly to the γ-ray flux, as can be seen from figure 2.9. At $x = \frac{E_\gamma}{E_p} = 0.1$ about 25% of all γ-rays come from η decays.
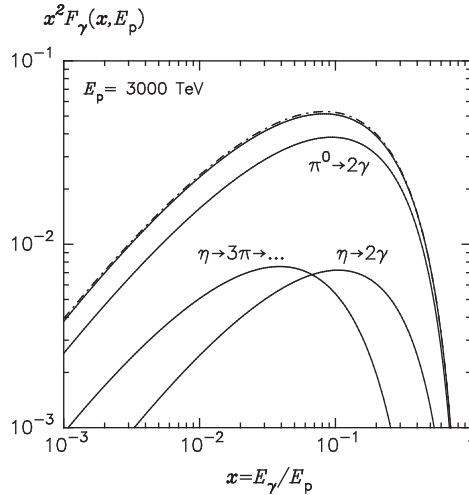
Figure 2.9: γ**-ray energy spectra for p-p interactions at 3000 TeV** - The contributions from π^0 and η meson decay are given separately. Figure taken from [71]

The parametrization used for the spectra in figure 2.9 are given as

$$
\begin{aligned}
F_\gamma(x, E_p) &= B_\gamma \frac{\mathrm{d}}{\mathrm{d}\,x}\left[\ln x \left(\frac{1 - x^{\beta_\gamma}}{1 + k_\gamma x^{\beta_\gamma}(1 - x^{\beta_\gamma})}\right)^4\right] \\
&= B_\gamma \frac{\ln x}{x}\left(\frac{1 - x^{\beta_\gamma}}{1 + k_\gamma x^{\beta_\gamma}(1 - x^{\beta_\gamma})}\right)^4 \times \\
&\quad \left[\frac{1}{\ln x} - \frac{4\beta_\gamma x^{\beta_\gamma}}{1 - x^{\beta_\gamma}} - \frac{4k_\gamma \beta_\gamma x^{\beta_\gamma}(1 - 2x^{\beta_\gamma})}{1 + k_\gamma x^{\beta_\gamma}(1 - x^{\beta_\gamma})}\right].
\end{aligned} \tag{2.54}
$$

The parameters k_γ, β_γ and B_γ depend only on the primary energy, represented by
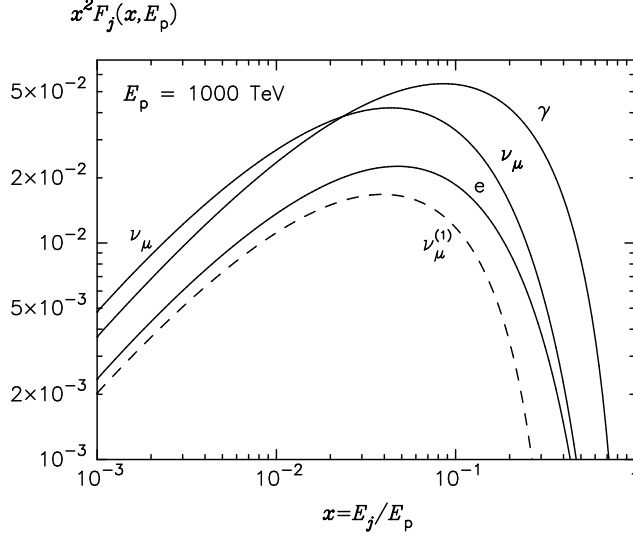
Figure 2.10: Energy spectra of γ-rays, ν_μ and electrons for p-p interactions at 1000 TeV - The dashed curve gives the contribution to the ν_μ-flux from direct $\pi^\pm$ decay. Figure taken from [71]

$L = \ln \frac{E_p}{[1\text{TeV}]}$:

$$B_\gamma = 1.30 + 0.14\,L + 0.011\,L^2 \tag{2.55}$$

$$\beta_\gamma = \frac{1}{1.79 + 0.11\,L + 0.008\,L^2} \tag{2.56}$$

$$k_\gamma = \frac{1}{0.801 + 0.049\,L + 0.014\,L^2} \tag{2.57}$$

The spectra of all secondaries produced in single proton collisions at energy 1 PeV is shown in figure 2.10. The energy relations from cosmic ray protons to γ-rays and ν_μ can be inferred from this plot. The average energy of ν_μ from a single proton collision is about 5% of the initial proton energy and about a factor 2 lower than the average γ-ray energy.

The parametrization of the ν_μ spectrum from direct $\pi^\pm$ decay, as shown in figure 2.10, is given in [71] as:

$$F_{\nu_\mu^{(1)}}(x, E_p) = B' \frac{\ln y}{y} \left(\frac{1 - y^{\beta'}}{1 + k'y^{\beta'}(1 - y^{\beta'})} \right)^4 \times$$

$$\left[\frac{1}{\ln y} - \frac{4\beta'y^{beta'}}{1 - y^{beta'}} - \frac{4k'\beta'y^{beta'}(1 - 2y^{\beta'})}{1 + k'y^{beta'}(1 - y^{beta'})} \right]. \tag{2.58}$$

Here $x = \frac{E_{\nu_\mu}}{E_p}$ and $y = \frac{x}{1 - r_\pi} = \frac{x}{0.427}$. The parameters k', β' and B' are correspondingly

given as

$$B' = 1.75 + 0.204\,L + 0.010\,L^2 \qquad (2.59)$$

$$\beta' = \frac{1}{1.67 + 0.111\,L + 0.0038\,L^2} \qquad (2.60)$$

$$k' = \frac{1}{1.071 + 0.086\,L + 0.002\,L^2} \qquad (2.61)$$

The spectra of γ-rays and ν_μ from a specific proton flux $J_p(E_p)$ is finally obtained by solving the integral:

$$\phi_\gamma E_\gamma \equiv \frac{\mathrm{d}\,N_\gamma}{\mathrm{d}\,E_\gamma} = c \cdot n_H \cdot \int\limits_{E_\gamma}^{\infty} \sigma_{inel}(E_p) J_p(E_p) F_\gamma\left(\frac{E_\gamma}{E_p}, E_p\right) \frac{\mathrm{d}\,E_p}{E_p} \qquad (2.62)$$

Here c is the vacuum light speed and n_H the density of the ambient hydrogen gas. An equivalent equation is valid for neutrinos.

Figure 2.11 shows the resulting energy spectra calculated for a primary proton spectrum of the form

$$J_p(E_p) = \frac{A}{E_p^{\alpha}} \exp\left[-\left(\frac{E_p}{E_0}\right)^{\beta}\right] \qquad (2.63)$$

which is a power-law spectrum with an exponential cut-off at E_0. The relevant parameters used, are given in figure 2.11.

All parametrization used in [71] are accurate within several percent in the energy range $0.1\,\mathrm{TeV} < E_p < 10^5\,\mathrm{TeV}$.
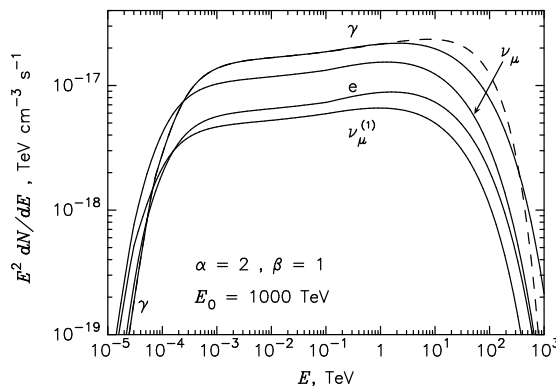
Figure 2.11: Energy spectra of γ-rays, ν_μ and electrons for proton-proton collisions with a proton spectrum given by equation 2.63. - The dashed curve uses a different approximation. Figure taken from [71].

2.4.4   Implications of observed gamma-ray spectra from the galaxy

In many cases the spectra of galactic γ-ray sources observed by H.E.S.S. and other IACTs are best fitted if an exponential energy cut-off of the form given in equation (2.63) is assumed. The cut-off energies found in such fits are typically in the range from a few TeV to 20 TeV [32][31][30][33]. According to the parametrization given in the previous section this relates to a cut-off energy in a neutrino spectrum of several TeV, assuming that the observed γ-radiation is fully of hadronic origin. In figure 2.12 the γ-ray spectrum of the crab nebula, a SNR of a supernova explosion which was observed in the year 1054, is shown. The neutrino spectrum has been deduced from the parametrized fit to the observed data. The found cut-off energy is at ~ 14TeV.
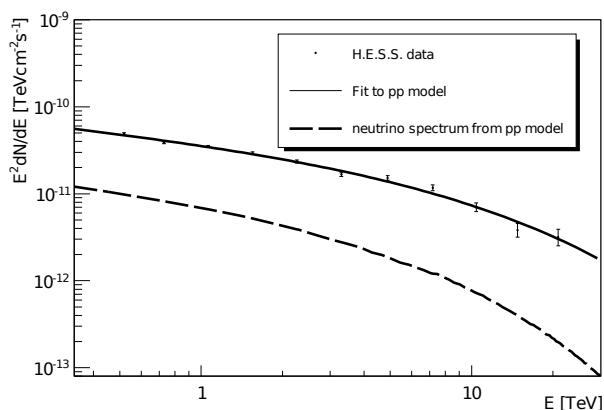
Figure 2.12: Fit to the energy spectrum of the crab nebula - The spectrum of the crab nebula as observed by H.E.S.S. [32] is fitted according to the parametrization given in [71]. The ν_μ spectrum deduced from this parametrization is also shown. Graph from [86]

Km^3-scale neutrino telescopes such as IceCube are optimized for neutrino energies above several TeV and thus galactic sources with the observed cut-offs will be hard to detect, even though the knowledge on the γ-spectra somewhat improves the sensitivity of an analysis [86]. This is one of the main motivations to extend IceCubes capabilities at lower neutrino energies, which has been pioneered by the integration of AMANDA in IceCube and lead to the design and construction of DeepCore (see chapter 5).

2.5   Other sources of neutrinos

2.5.1   Dark matter - Neutrinos from neutralino annihilations

There are many indications that dark matter is very abundant throughout the universe [96][84][87][35][15] and there is strong evidence that a large part of it is non-baryonic and not formed by massive neutrinos or other relativistic ("hot") particles [87][35]. Thus dark matter is "cold", i.e. non relativistic.

One of the most promising candidates for cold dark matter (CDM) are Weakly Interacting Massive Particles (WIMPs). Such particles, which would only interact through gravitation and the weak force are predicted e.g. in super-symmetric extensions to the standard model of particle physics. These models introduce a symmetry between bosons and fermions in the form of a super-symmetric partner to each standard model particle. Fermions get bosonic partners called "gauginos" and bosons get fermionic partners, "higgsinos" and "sfermions". In the simplest model, the Minimal Super-symmetric Standard Model (MSSM), the lightest super-symmetric particle (SSP) is stable and can only be destroyed by annihilation. This particle, a mass eigenstate of gauginos and higgsinos, is its own anti-particle and usually called *the* "neutralino" χ (there is a number of such mass-eigenstates that are called neutralino, but in our case we only refer to the lightest one). The mass of the χ is one of many model parameters, but has been restricted to $46\,\mathrm{GeV} < m_\chi < 1\,\mathrm{TeV}$ at particle accelerators and by cosmological arguments.

In χ-annihilations preferably non-relativistic standard-model particles are produced

$$\chi\chi \rightarrow W^+W^- , \tau^+\tau^-, q\bar{q}, Z^0Z^0, ... \tag{2.64}$$

Neutrinos are produced in the decays of the annihilation products.

The neutralino WIMPs would have been produced in the big bang and since the decoupling from ordinary (standard model) matter it would have accumulated in the potential wells of massive objects throughout the universe, such as the Sun or the Earth [56]. This accumulation is a slow process, since the WIMPs need to loose energy through multiple interactions in order to get caught. Eventually they will have lost so much energy that they follow an orbit within the star or planet. When the accumulated WIMP density becomes large enough, annihilations become probable and an equilibrium is reached between accumulation and annihilation, which depends only on the neutralino scattering cross-section. Thus a constant flux of neutrinos from χ annihilation can be expected at Earth.

Depending on the annihilation channel the average neutrino energy will be between

$\frac{1}{3}$ (hard channel) and $\frac{1}{6}$ of the initial neutralino mass m_χ. The hardest annihilation channels are

$$\chi\chi \;\to\; W^+W^- \qquad \text{and} - \qquad \chi\chi \;\to\; \tau^+\tau^- \tag{2.65}$$

while the softest channel is given by hadronization of

$$\chi\chi \;\to\; b\bar{b}. \tag{2.66}$$

Accordingly the expected neutrino energies lie from a few GeV up to several TeV. Measurements of (or upper limits on) neutrino fluxes from the sun (in this energy range) constrain the parameter space of the MSSM model and especially the mass of the neutralino. One of the chief motivations to increase IceCubes capabilities at the lowest energies is to test the neutralino mass range at and below a few hundred GeV.

2.6 Neutrino oscillations

The disappearance of ν_μ has been seen for solar[36][21], atmospheric [20] and accelerator neutrinos [3][16] and neutrino oscillation is generally accepted as the underlying process, even though no direct appearance of an oscillated neutrino could be measured yet. However the theory of neutrino oscillation makes predictions well in agreement with the measured neutrino fluxes and the confirmation of neutrino disappearance has been one of the major discoveries in the recent years of particle physics.

The neutrino flavor eigenstates $\alpha = (e, \mu, \tau)$ are linear combinations of mass eigenstates $i = (1, 2, 3)$:

$$|\nu_\alpha\rangle = \sum_i U^*_{\alpha i} |\nu_i\rangle \tag{2.67}$$

where $U^*_{\alpha i}$ is the unitary leptonic mixing matrix. If neutrinos were mass-less $U^*_{\alpha i}$ would be the unit matrix and the mass and flavor eigenstates were identical. In the case that only 3 mass eigenstates exist (no sterile neutrinos) the mixing matrix is called the Maki-Nagakawa-Sakata (MNS-) matrix and reads

$$U^* = \begin{pmatrix} c_{12}c_{13} & c_{13}s_{12} & s_{13}e^{-i\delta} \\ -s_{12}c_{23} - c_{12}s_{13}s_{23}e^{i\delta} & c_{12}c_{23} - s_{12}s_{13}s_{23}e^{i\delta} & c_{13}s_{23} \\ s_{12}s_{23} - c_{12}c_{23}s_{13}e^{i\delta} & -s_{12}c_{23} - s_{12}s_{13}c_{23}e^{i\delta} & c_{13}c_{23} \end{pmatrix} \tag{2.68}$$

here $c_{ij} = \cos\theta_{ij}$ and $s_{ij} = \sin\theta_{ij}$. θ_{ij} is the mixing angle. δ is the CP violating phase and we have neglected the fact that neutrinos might be Majorana particles (i.e. their

own anti-particles).

A consequence of the flavor mixing is that neutrinos can oscillate from one flavor state to another. The probability for such oscillations depend on the mixing matrix, the mass-difference $\Delta m_{ij}^2 = m_i^2 - m_j^2$, the neutrino energy and the traveled distance L (strictly it depends on the traveling time t, but we assume relativistic neutrinos) and is given by

$$
\begin{aligned}
P_{\alpha \to \beta} = \delta_{\alpha\beta} \quad &- \quad 4 \sum_{i>j} Re(U_{\alpha i}^* * U_{\beta i} U_{\alpha i} U_{\beta i}^*) \sin^2 \left(\frac{1.27 \Delta m_{ij}^2 L}{E} \right) \\
&+ \quad 2 \sum_{i>j} Im(U_{\alpha i}^* * U_{\beta i} U_{\alpha i} U_{\beta i}^*) \sin^2 \left(\frac{2.54 \Delta m_{ij}^2 L}{E} \right)
\end{aligned}
\tag{2.69}
$$

where Δm_{ij}^2 is given in eV^2, L in km and E in GeV. Following from this the distance between two probability maxima is

$$
L = 2.48 \left(\frac{E}{1\,\text{GeV}} \right) \left(\frac{\text{eV}^2}{\Delta m_{ij}^2} \right)
\tag{2.70}
$$

This length is well below cosmic scales even for the most energetic neutrinos and thus we can assume that neutrinos from cosmic sources are fully mixed. Following this argument, the oscillation probability can be evaluated as an average probability:

$$
\langle P_{\alpha\beta} \rangle = \langle P(\nu_\alpha \to \nu_\beta) \rangle = \sum_i |U_{\alpha i}^*|^2 |U_{\beta i}|^2
\tag{2.71}
$$

If a distant source emits neutrinos in a fixed ratio of neutrino flavors $F_s(\nu_e) : F_s(\nu_\mu) : F_s(\nu_\tau)$ then, after propagation to the Earth, the flavor ratio $F_E(\nu_e) : F_E(\nu_\mu) : F_E(\nu_\tau)$ is given by

$$
\begin{pmatrix} F_E(\nu_e) \\ F_E(\nu_\mu) \\ F_E(\nu_\tau) \end{pmatrix} = \begin{pmatrix} \langle P_{ee} \rangle & \langle P_{\mu e} \rangle & \langle P_{\tau e} \rangle \\ \langle P_{e\mu} \rangle & \langle P_{\mu\mu} \rangle & \langle P_{\tau\mu} \rangle \\ \langle P_{e\tau} \rangle & \langle P_{\mu\tau} \rangle & \langle P_{\tau\tau} \rangle \end{pmatrix} \begin{pmatrix} F_s(\nu_e) \\ F_s(\nu_\mu) \\ F_s(\nu_\tau) \end{pmatrix}
\tag{2.72}
$$

For an initial ratio of 1 : 2 : 0 (see section 2.4) the resulting ratio observable at Earth would be 1 : 1 : 1.

Oscillations of atmospheric neutrinos takes place in the energy range below 100 GeV, because the oscillation lengths get too long to give significant oscillation on the length scale of the Earths diameter ($\sim 10^7 m$). Figure 2.13 shows a, so called, oscillogram of the Earth [4]. It gives the survival probability of ν_μ (left panel) and $\bar{\nu}_\mu$ (right panel) after traveling through the Earth, in dependence of the neutrino energy and zenith
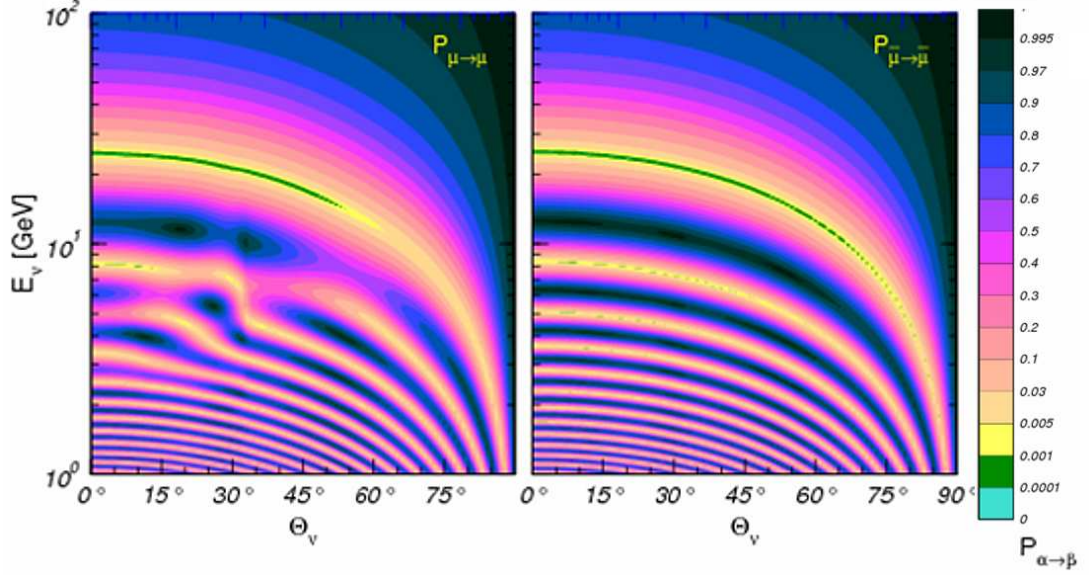
Figure 2.13: Neutrino oscillogram of the Earth - Survival probability of ν_μ (left) and $\bar{\nu}_\mu$ (right) of energy E after passage through the Earth at zenith angle θ_ν. Matter effects included assuming $\sin^2 \theta_{13} = 0.125$ [4].

angle θ_ν. Thus $\theta_\nu = 0$ corresponds to the full diameter of the Earth. The plots also includes matter induced oscillation resonances from the MSW effect [95] [77], calculated assuming $\sin^2 \theta_{13} = 0.125$. This effect is not seen in the $\bar{\nu}_\mu$ oscillations, since there is effectively no anti-matter in the Earth.

The highest energy minimum of survival probability is related to pure vacuum oscillation and is set at ~ 27GeV for a vertical neutrino. This energy is well below the IceCube energy threshold, but as we will show later, the DeepCore low-energy extension has a trigger threshold well below this energy and may have some sensitivity to measure the oscillation effect.

3

Detection of high energy neutrinos in IceCube

In this chapter we will describe the principles of neutrino detection as they are used in IceCube. We will start by reviewing the neutrino interactions with nuclei and the characteristics of the interaction products and the processes which guide their propagation in matter. In the case of IceCube the relevant matter is the South Pole ice, the properties of which are discussed thereafter. The layout of the IceCube detector, which makes use of this ice properties is then discussed, followed by IceCubes data taking procedure. Finally we give a short introduction into a typical point source analysis.

3.1 Neutrino interactions and event signatures

3.1.1 Neutrino interactions

In the standard model of particle physics (SM) the ν interacts only by the weak force. The force is mediated by two charged and one neutral vector boson called $W^{\pm}$ and Z^0, respectively. Interactions involving the exchange of a $W^{\pm}$ are called charged current (CC) and those involving a Z^0 neutral current (NC) interactions. At the high energies considered at neutrino telescopes only the deep inelastic scattering (DIS) processes are of importance, namely:

$$\nu_l + N \rightarrow l + X \qquad \text{(CC)} \qquad (3.1)$$

$$\nu_l + N \rightarrow \nu_l + X \qquad \text{(NC)}, \qquad (3.2)$$

($l = e, \mu, \tau$). In the NC case a neutrino of the same flavor is found in the initial and the final state, while in CC interactions a charged lepton corresponding to the initial ν

flavor is present in the final state. In both cases a hadronic cascade will emerge from the nucleon remnant (X).

The cross-sections of $\nu - N$ scattering have been calculated, e.g. in [52]. They strongly depend on the parton distribution functions (PDF) of the nucleon. Up to $\sim 1\text{PeV}$ these functions have been determined at collider experiments [2][13] and have been tabulated. e.g. by the CTEQ collaboration [79]. Above the energies accessible at collider experiments, the cross-sections have to be extrapolated, which introduces larger uncertainties and model dependencies. If new physics should be present at higher energies the cross-sections might change considerably.

The general behavior of the integrated cross-section in CC and NC $\nu - N$ interactions $\sigma_{\text{CC/NC}}$ is well described by the dependency

$$\sigma_{\text{CC/NC}} \propto \left(\frac{1}{Q^2 + M_{W/Z}^2} \right)^2 E_\nu, \tag{3.3}$$

where $-Q^2$ is the invariant squared momentum transfer from the incident ν to the outgoing charged lepton. $M_{W/Z}$ is either the mass of the $W^\pm$ (80.4 GeV) or of the Z^0 (91.2 GeV). For $Q^2 < M_{W/Z}^2$ the constant boson mass dominates the propagator term $(1/(Q^2 + < M_{W/Z}^2)$ and the cross-section rises linearly with E_ν. For Q^2 larger then the square of the respective boson masses the momentum transfer dominates and the cross-section rises slower.

In figure 3.1 the cross-sections for CC and NC $\nu - N$ and $\bar{\nu} - N$ interactions are shown. The CC are generally larger than the NC cross-sections. At low energies the cross-sections for $\nu - N$ scattering are larger than for $\bar{\nu} - N$, but at larger energies they become almost equal, as the contribution of sea quarks dominates the PDF.

Interactions of ν with electrons generally have a much lower cross-section and usually can be neglected at the relevant energies at neutrino telescopes. One exception is the process $\bar{\nu}_e\, e^- \rightarrow W^-$ which has a resonant behavior at roughly $E_\nu = \frac{M_W^2}{2M_e} = 6.3\,\text{PeV}$ (Glashow peak [55]). At this energy the cross-section for W^--production is ~ 2 orders of magnitude above the one for $\nu - N$ interaction.

Neutrino telescopes typically make use of the small ν-cross-section to reduce the background of atmospheric muons. As ν can traverse the Earth without interactions and muons are typically stopped after several km, this can be done by looking for muons induced by upwards-going ν that have penetrated the Earth. At high energies however, this becomes increasingly difficult, as the ν cross-sections become larger and the Earth finally becomes opaque to neutrinos ($E_\nu > 1$ PeV). Figure 3.2 shows the mean free
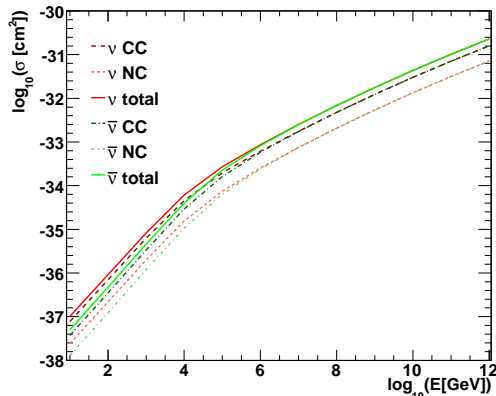
Figure 3.1: Neutrino-nucleon cross-sections - Charged and neutral current cross-sections of neutrinos (red) and anti-neutrinos (green).
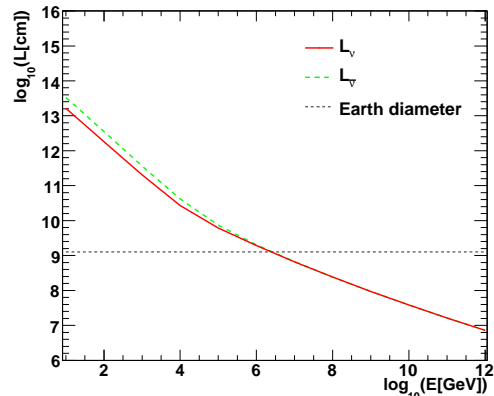
Figure 3.2: Mean free path of (anti-) neutrinos in water - Energy dependence of the mean length a neutrino travels in water before interacting. The Earth radius (scaled by the average matter density of the Earth) is shown to illustrate the approximate energy at which the Earth becomes opaque to neutrinos.

path of neutrinos in dependence of their energy, as calculated by

$$L = \frac{1}{N_A \; \sigma_{\text{CC/NC}} \; \rho}. \tag{3.4}$$

N_A is the Avogadro number $6.022 \cdot 10^{23} mol^{-1}$ and ρ is the density of the traversed matter. For figure 3.2 the density of water $(1\,\text{g/cm}^3)$ has been used. The equivalent of the Earth diameter in cm.w.e. (centimeter water equivalent, $\rho_{Earth} \sim 5.5\text{g/cm}^3$) is shown for comparison. At the ultra high energies (UHE), above few PeV, neutrino telescopes typically resort to searches for neutrinos from the horizon. PeV ν_τ's on the other hand will not be completely stopped by interactions in the Earth, as muons and electrons are. The τ's produced in the interaction, due to their short lifetime, decay before they interact and pass a significant fraction of the energy to a secondary ν_τ, which eventually may reach the detector or go through another cycle of this regeneration. In some cases (see below) the τ decay will also produce a ν_e or ν_μ.

3. DETECTION OF HIGH ENERGY NEUTRINOS IN ICECUBE

3.1.2   Energy loss of charged particles moving through matter

Charged particles that pass through matter will lose energy mainly through the processes of

- ionization

- photo-nuclear interaction

- Bremsstrahlung

- $e^{\pm}$ pair production

- decay

Electrons with energies above ~ 1 GeV will lose their energy very quickly through emission of Bremsstrahlung, which is caused by deceleration and deflection in the field of the atomic nuclei. In alternate $e^{\pm}$ pair production of the emitted photon and further Bremsstrahlung an electro-magnetic cascade is created, comparable to the process in air-showers, though on shorter length scales.

The tauon τ has a very short lifetime of $\sim 291 \cdot 10^{-5}$s and thus up to PeV energies they rather decay then lose energy through interactions with the surrounding matter. In all decays a ν_{τ} will be found. In $\sim 65\%$ of all decays the τ will decay also into one ore more charged and neutral hadrons (mostly pions) which create a hadronic cascade. In $\sim 18\%$ of all cases the τ decays into an electron and two neutrinos, with the electron starting an electro-magnetic cascade. In the remaining 17% a muon is produced along with two neutrinos.

The contribution of the above mentioned energy losses in the propagation of muons through ice is shown in figure 3.3. The energy loss per unit length $-\frac{\mathrm{d}E}{\mathrm{d}x}$, often called "stopping power" is shown in dependence of the muon energy. Below ~ 1TeV the energy loss is dominated by ionization losses, as described by Bethe's stopping power formula [42]:

$$-\frac{\mathrm{d}E}{\mathrm{d}x}_{ion} = K\frac{Z}{A}\frac{1}{\beta^2}\left[\frac{1}{2}\ln\frac{2m_ec^2\beta^2\gamma^2T_{max}}{I^2} - \beta^2 - \frac{\delta(\beta\gamma)}{2}\right] \qquad (3.5)$$

Here I is the mean excitation energy in eV, Z is the atomic number of the stopping material, while A is its atomic mass number. The δ-correction term takes into account polarization effects which effectively reduce the energy losses above a few GeV muon energy. T_{max} is the maximal kinetic energy that can be transferred to a free electron in a single collision. The mean excitation energy I can be taken from tables [65] or
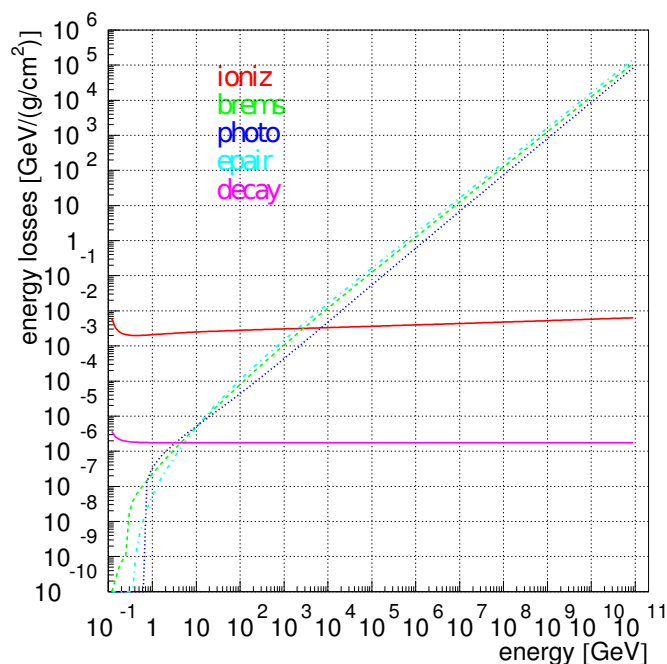
Figure 3.3: Muon energy loss in water - Contributions from ionization (red), Bremsstrahlung (green), photo-nuclear interaction (dark blue), electron-positron pair production (light blue) and muon decay (violet) are shown. From [22].

approximated by Bloch's formula $I = (10 \text{ GeV}) \cdot Z$. As the ionization losses are not depending on energy too strong we can approximate an energy loss of ~ 1 GeV per 5 m of passage through ice.

Above ~ 1 TeV radiative processes become important and Bremsstrahlung, $e^{\pm}$ pair production and photo-nuclear interactions, where a photon is exchanged between the muon and the nucleus, dominate.

All the given energy loss mechanisms have stochastic nature, i.e. they occur in single distinct interactions, but as for ionization , where the Bethe formula gives an excellent approximation, the muon energy loss in the range above some tenths of GeV is very well described by a continuous loss following

$$-\frac{\mathrm{d}E}{\mathrm{d}x} = a + bE \tag{3.6}$$

The parameters a and b have been determined for water, e.g. in [22], as

$$
\begin{aligned}
a &= 0.2596 \frac{\text{GeV}}{\text{m.w.e.}} \\
b &= 0.3571 \frac{10^{-3}}{\text{m.w.e.}}
\end{aligned}
\tag{3.7}
$$

(m .w.e. = meter water equivalent). The average range of x of a muon in ice is following from 3.6 as

$$x = \frac{1}{b} \ln 1 + \frac{b}{a} E_0, \tag{3.8}$$

where E_0 is the initial energy of the muon.

3.1.3 Čerenkov radiation

If a charged particle moves through a polarizable dielectric medium at a speed faster than the speed of light in that medium, it emits Čerenkov radiation. The particle polarizes the atoms it passes by and as they fall back into their ground states the polarization energy is emitted as photons. In figure 3.4 the light emission is illustrated. The photons are emitted at a characteristic angle θ_C to the particle direction which is defined by [66]:

$$\cos \theta_C = \frac{1}{\beta \, n(\lambda)} \tag{3.9}$$

Here $n(\lambda)$ is the refractive index of the medium. This relation holds above the so
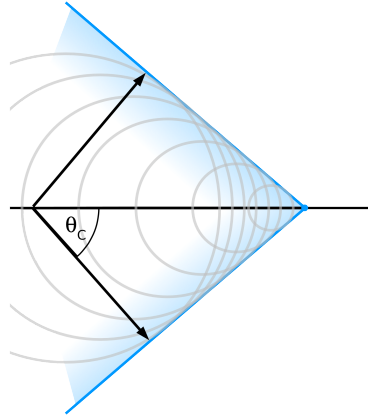
Figure 3.4: Čerenkov light emission - Schematic view.

called Čerenkov threshold $\beta > 1/n(\lambda)$. For muons moving through ice ($n \sim 1.32$ at $\lambda = 400$ nm) this threshold is at

$$E_C = \frac{m_\mu}{\sqrt{1 - \frac{1}{n^2}}} \approx 161 \, \text{MeV} \tag{3.10}$$

At the large energies relevant for this work ($E_\mu > 1\text{GeV}$) we can safely assume $\beta \approx 1$ and the Čerenkov angle in ice thus is fixed at $\theta_C \approx 41°$.

The spectrum of the emitted light follows the Frank-Tamm-formula [66]:

$$\frac{\mathrm{d}^2 N}{\mathrm{d}\,x\,\mathrm{d}\,\lambda} = \frac{2\pi\alpha}{\lambda^2}\left(1 - \frac{1}{\beta n(\lambda^2)}\right), \tag{3.11}$$

where α is the fine structure constant ($\alpha \approx 1/137$). The number of photons emitted per unit length is inversely proportional to the wavelength. The spectrum is peaked in the ultra-violet region (as λ gets smaller, eventually $n(\lambda)$ approaches 1 and the $1/\lambda$ rise is overcompensated). In the sensitive range of photo-multiplier tubes (PMTs) of 300 to 500 nm still $\sim 2.6 \cdot 10^4$ photons are emitted per meter. The total energy loss per meter is however negligible in comparison to ionization and the radiative processes discussed in the previous section (~ 86 keV/m).

At energies above ~ 1 TeV, where radiative processes start to dominate, the light yield is significantly increased and eventually dominated by Čerenkov emission of secondary $e^\pm$.

3.1.4   Event topologies

The three types of charged leptons created in neutrino interactions lead to a number of different event topologies to be expected at neutrino telescopes. All of these are either track-like, cascade-like or a mixture of both. Track-like events are produced by charged particles going straight through the detector and emitting Čerenkov radiation. Cascades are either of hadronic or electro-magnetic origin, in a comparable way as in air-showers, but are spatially very limited. Below ~ 10 PeV, cascades are only up to 5 m long. The Čerenkov radiation emitted by hadronic and electro-magnetic cascades is not distinguishable in a neutrino telescope. At the distances typical for module spacing in neutrino telescopes the emitted light appears nearly spherical with a somewhat stronger light emission in the direction of the neutrino movement, being blurred by scattering. The absorption of light affords that a cascade needs to be within or very close to the detector volume in order to be detected.

- In NC interactions there is only a hadronic cascade present at the interaction vertex. The interacting neutrino flavor can not be distinguished.

- In CC interactions of ν_e a hadronic and a electro-magnetic cascade are present, which overlap each other. Due to the similarity of the Čerenkov signature in hadronic and electro-magnetic cascades these events can not be distinguished from the NC interactions.

- In CC interactions of ν_μ the resulting muon can travel a long way before being stopped or decaying and the Čerenkov emission along its way gives these events a track-like appearance. Thus also ν_μ interactions taking place far away from the detector volume can be detected if the muon track passes through or close by the detector. If the interaction vertex of the ν_μ is within the detector volume, also the initial hadronic cascade is eventually visible.

- The τ produced in CC interactions of ν_τ has a very short lifetime which lead to an average track length of only ~ 45 m at ~ 1 PeV. The decay of a τ gives a hadronic or electro-magnetic cascade in $\sim 83\%$ of the cases, while in the muonic decay mode a muon is produced which will show the track-like topology. At the lower energies where the τ track is short the initial hadronic cascade and an eventual cascade from the τ decay will be hardly distinguishable. If the energy of the τ is sufficiently large to travel a longer way (i.e. ~ 1 km at ~ 100 PeV) the cascades maybe separated giving the so called "double bang" topology. If one of the cascades happens to be outside the detector, only one cascade is seen in conjunction with a track-like part.

The most beneficial topology for neutrino telescopes is the track-like event, as it allows a relatively good reconstruction of the neutrino direction, essential for the search of neutrino point-sources.

3.2 Optical properties of South Pole ice

The large volumes ($\mathcal{O}(\mathrm{km}^3)$), needed to detect neutrino interactions at the TeV- to PeV-scale, exclude controlled man-made detector materials, such as they are used at experiments investigating neutrinos at lower energies. Consequently, neutrino telescopes make use of the most abundant material on Earth which happens to have good optical properties: water, or in the case of IceCube, its frozen form: ice. In fact the deep glacial ice at the South Pole is the most transparent solid known.
The glacier covering the antarctic continent is the biggest glacier on Earth. It has grown over $\sim$165.000 years [81], with each years precipitation adding a new layer of snow which becomes more and more compressed as the next years snow is piled up above. Thus, the top layer of the antarctic ice sheet, called the "firn" still encloses a lot of air. At larger depths air is trapped in sub-millimeter sized air-bubbles, which have a strong impact on the scattering of light. As the pressure increases, the air in this bubbles is forced to form air-hydrates, which are crystals of very similar optical

properties as those of ice. Below $\approx$1500 m almost all air-bubbles have gone through this transition and ideal conditions are found for detection of Čerenkov radiation from neutrino induced muons.[39]

The light attenuation is determined by scattering and absorption, happening predominantly on micron-sized dust-grains, enclosed in the ice. This dust has been brought to Antarctica through the wind and is accumulated in each years layer of snow. It is therefore a tracer of the atmospheric dust-concentration and composition at the time of the snow layer formation and can give much information on the climatological changes throughout the time of the glacier growth [5]. As a consequence, the optical properties of the ice change strongly with depth and only weakly within a plane of fixed depth. The dust particles enclosed in the ice consist mainly of minerals, salt, acids and soot [39], which have different contributions to scattering and absorption.

3.2.1   Scattering

Scattering is a stochastic process, but can approximately be described by an average distance between two scatters λ_s and an average scattering angle $\langle\cos\theta\rangle$. $\langle\cos\theta\rangle = 0$ describes a forward-backward-symmetric scattering of which isotropic scattering is a special case. This would cause the particle direction to be effectively randomized after one scattering length λ_s. If $\langle\cos\theta\rangle > 0$ scattering happens preferably to the forward region and $\langle\cos\theta\rangle = 1$ is identical to no scattering at all. As forward scattering will not randomize the direction completely within one scattering length it is useful to define an effective scattering length λ_e, which describes the length after which the direction has been fully randomized. It is defined by

$$\lambda_e = \frac{\lambda_s}{1 - \langle\cos\theta\rangle}. \tag{3.12}$$

The dust which dominates scattering at more than 1500 m depth can be described by an average angle $\langle\cos\theta\rangle \approx 0.94$, and thus scattering is directed strongly in the forward region, leading to longer effective scattering lengths.

Often it is also appropriate to use the reciprocal value of the scattering length $b_e = \frac{1}{\lambda_e}$, called effective scattering coefficient. The scattering coefficient is dependent on the wavelength of the light by a simple power law $b_e \propto \lambda^{-\alpha}$, with α being ≈ 0.9 [39]. Thus scattering is stronger at shorter wavelengths.

3.2.2 Absorption

In a similar way as for scattering an absorption length λ_a can be defined as the distance at which the survival probability of a photon has dropped by a factor $1/e$. The reciprocate value $a = \frac{1}{\lambda_a}$ is then called the absorption coefficient. To the wavelength range from 200 nm to 500 nm the antarctic ice is extremely clear and absorption is dominated by the dust grains, which thus determine almost solely the optical properties of South Pole ice in the depths IceCube is being deployed. Measurements of the effective scat-
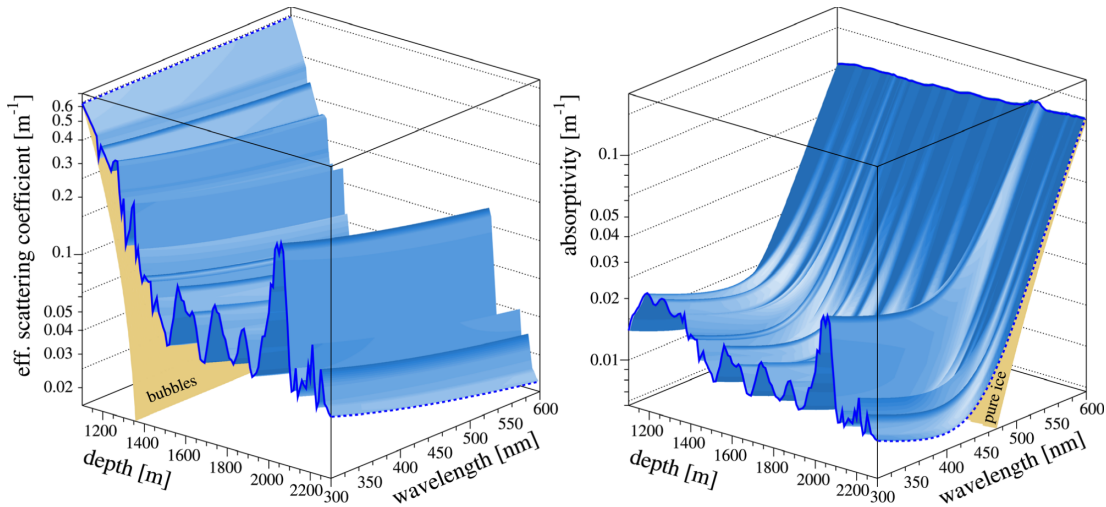
Figure 3.5: Effective scattering coefficient and absorptivity in South Pole ice - Left: Effective scattering coefficient in dependence of depth and wavelength; Right: Absorptivity in dependence of depth and wavelength. From [39].

tering and absorption lengths have been carried out at the South Pole down to depths of 2300 m, with an emphasis on the region from 1500 m to 2000 m [39]. By measuring the response of the AMANDA array (see section 3.3.4) to a number of well controlled light sources mounted on AMANDA optical modules, the scattering and absorption effect have been distinguished and the respective coefficients were measured. Figure 3.5 shows the resulting effective scattering (left) and absorption (right) coefficients in dependence of depth and wavelength. At the depths below 1500 m the dust dominates the optical properties, which is nicely illustrated by the absorption and scattering coefficient following the exact same depth profile, as they trace the dust concentration. The scattering lengths are typically shorter than absorption lengths and their variations are strong, ranging from ~ 5 m to ~ 40 m. In the strongest dust peak at ~ 2000 m, which corresponds to an age of 65.000 years, the scattering and absorption lengths are

shortest. Below this most prominent "dust layer" the clearest ice is found which gives the best conditions for Čerenkov light detection.

As IceCube instruments a detector volume down to depths of 2450 m the measured
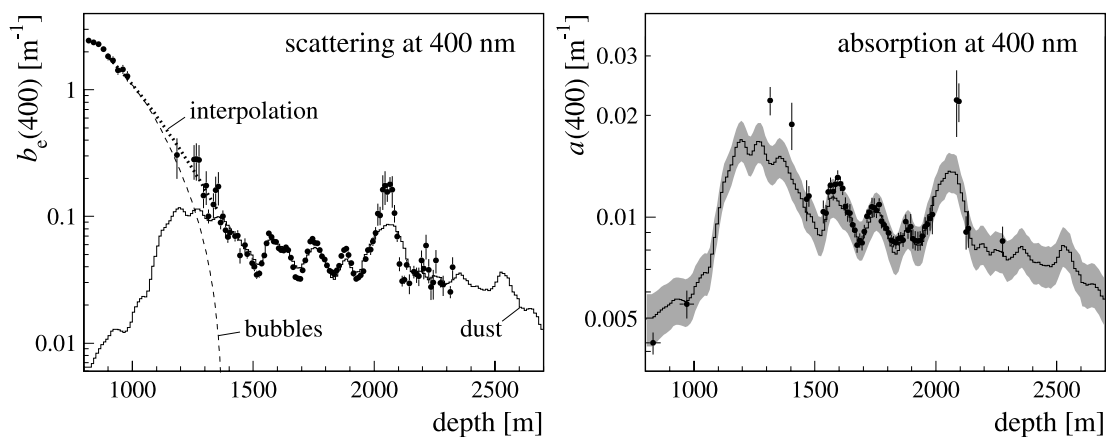
Figure 3.6: Scattering, absorption and dust concentration in South Pole ice - Scattering (left) and absorption (right) in dependence of depth at 400 nm wavelength. The solid line gives the dust concentration in ice and forms the basis for an extrapolation of these parameters to greater depths, as they are used in IceCube simulations. From [39].

ice properties have to be interpolated. This has been done by making use of dust-concentrations measured from ice cores which were taken at the Vostok station [34] ($\sim$ 1000 km distant from the South Pole). Figure 3.6 shows that these dust-concentrations can be scaled to fit very well the scattering and absorption coefficients measured with AMANDA. It is therefore reasonable to assume that the dust-concentration governs the behavior of scattering and absorption also at greater depths.

3.3 The IceCube detector

The IceCube neutrino detector is being built to measure the Čerenkov light emitted by charged particles created in neutrino interactions (tracks and cascades). It utilizes the enormous layer of glacial ice covering most of the antarctic landmass both as a target for neutrinos and as the transparent medium needed to measure the Čerenkov radiation in a large volume.

The detector is currently under construction close to the geographical South Pole, at the Amundsen-Scott South Pole station. It consists of a surface air-shower array called *IceTop* and a volume of roughly 1 km^3 within the ice instrumented with optical sensors at depths between 1450 m and 2450 m. This in-ice part of the detector is made

up by the baseline configuration of IceCube and the DeepCore low-energy extension. The Antarctic Muon And Neutrino Detection Array (AMANDA) [25] was IceCubes predecessor equipping a significantly smaller volume. It was fully integrated into the growing IceCube detector, but has been decommissioned in spring of 2009.

3.3.1 The IceCube baseline layout

The baseline design of the IceCube in-ice part is optimized for detection and reconstruction of neutrinos at energies above several TeV. It consists of 4800 digital optical modules (DOMs, see below). These modules are installed on 80 support cables called *strings*. Consequently each of these 80 strings is equipped with 60 DOMs at a spacing of 17 m giving the instrumented volume a height of $\approx$ 1 km. The strings are arranged at average distances of 125 m in a hexagonal grid. Figure 3.7 shows the string layout of the complete detector. The IceCube baseline strings are marked by red dots and are numbered from 1 to 80.

Apart from the additional DeepCore extension only few modifications have been made to this baseline. Two outer strings (numbered 79 and 80) could not be installed in their original position as the ice has been discovered to be soiled, endangering the drill equipment. These two strings will instead become part of the DeepCore array. Furthermore the central IceCube string (number 36) is equipped in its lowest part with 14 DOMs that hold a high quantum efficiency photo-multiplier tube (PMT) instead of the standard PMT. These devices are also used on the additional DeepCore strings.

3.3.2 IceTop

IceTop is designed to detect cosmic ray air-showers at cosmic ray primary energies above 10^{17} eV. It will consist of 160 ice tanks, two of them installed next to each other above each string of the IceCube baseline layout. Each of the plastic tanks holds two standard IceCube DOMs. Its inner surface has a height of 1 m, a radius of 0.93 m and has a white coating, for diffuse reflection. The freezing process of the newly installed tanks is artificially slowed down to ensure that the ice is sufficiently clear. Coincidences between the pair of tanks at one string position discern noise from an air-shower signal. Apart from being a standalone air-shower detector IceTop coincidences with the IceCube in ice array allow

- a more accurate measurement of the cosmic ray spectrum and shower composition

- systematics studies
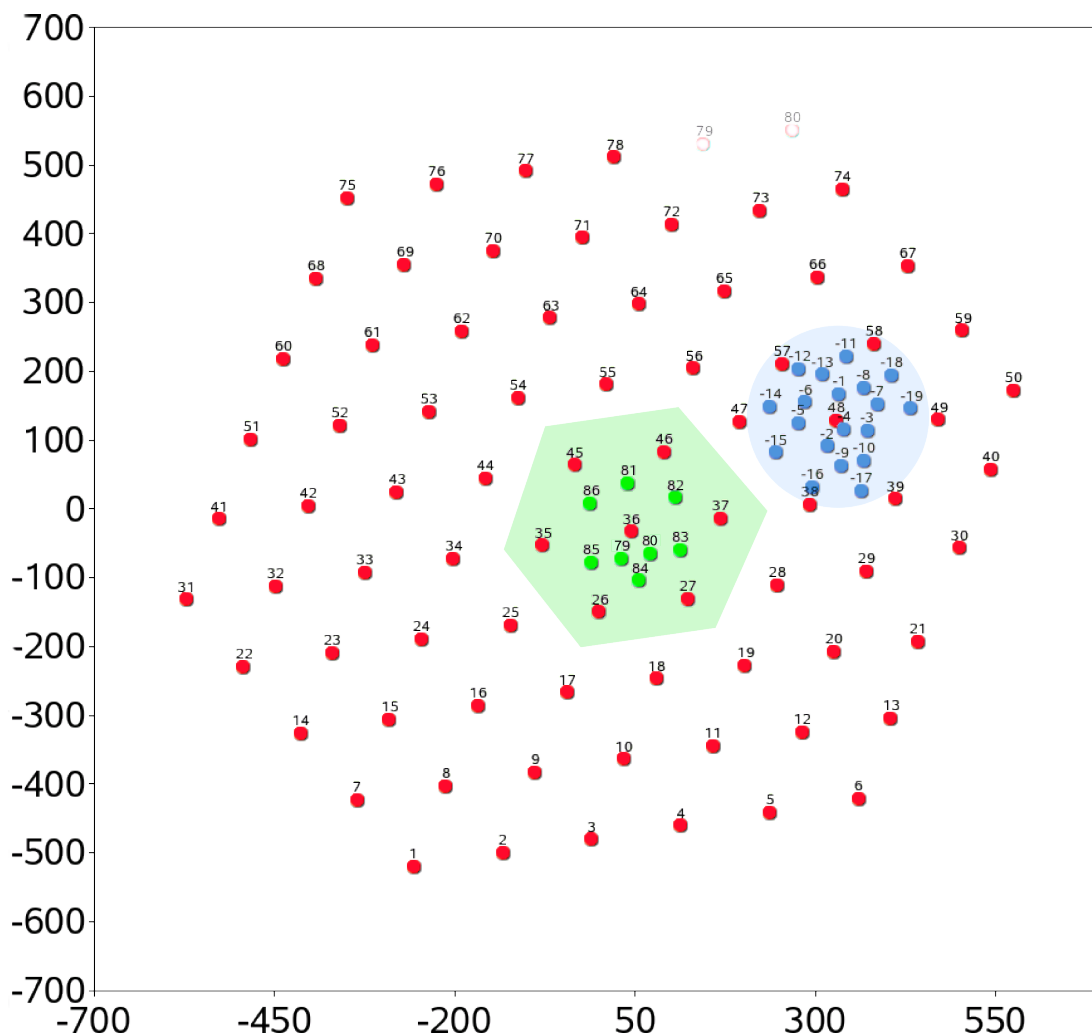
Figure 3.7: String positions of the complete IceCube detector with 86 strings
- Strings number 79 and 80 are not going to be deployed in the original position, instead
they will be part of the DeepCore extension (green shaded area). AMANDA strings have
negative numbers to distinguish them from IceCube (blue shaded area).

3.3.3 DeepCore

DeepCore has been designed to lower IceCubes energy threshold significantly below
100 GeV. This is done by 8 extra strings of which 6 are placed around a central IceCube
string (number 36) at distances of $\approx$ 72 m to this and also the 6 closest standard
IceCube strings. Each of theses 6 strings holds 60 standard IceCube DOMs which
house Hamamatsu PMTs of higher quantum efficiency, increased by $\approx$ 40%. 50 of

theses DOMs are placed in a 7 m spacing at the very bottom of the detector, equipping a height of $\approx$ 350 m. The remaining 10 DOMs are positioned in a 10 m spacing at a depth between 1760 m to 1850 m to support the veto capabilities against vertical muons. Two more strings are positioned at an even denser spacing of $\approx$ 42 m in between the 6 other DeepCore strings and the central string. These two have the same DOM positions as the other DeepCore strings, but house standard PMTs, as these are the repositioned baseline IceCube strings which were originally planned for deployment at positions 79 and 80. The design study of the DeepCore detector is described in all detail in chapter 5.

3.3.4 AMANDA

The Antarctic Muon And Neutrino Detection Array (AMANDA) has been build between 1995 and 2000 in two stages. The AMANDA B-10 detector, consisting of the first 10 strings was finished in 1997. The AMANDA II detector added another 9 strings, making a total of 19. 677 PMTs housed in optical modules equipped a volume of roughly 1/40 of IceCube. Deployment depths are between 1300 m and 2400 m with a main instrumented volume at depths between 1500 m and 2000 m. In contrast to Ice-Cube, the analogue signals of the optical modules are sent to the surface and digitalized in the surface counting house. AMANDAs optical modules are non-uniform since one of its purposes was to test and optimize possible technologies for the IceCube detector. Since 2007 AMANDA was fully integrated into the growing IceCube detector and data was taken in a combined mode. The combined data have been used e. g. for dedicated low energy point source searches [26].
The increased difficulty in AMANDA maintenance, the sub-optimal situation to have two separate data acquisition systems and the not optimal position on the upper border of IceCube, were major motivations for decommissioning AMANDA and building the DeepCore extension. The decommissioning of AMANDA took place in April 2009, after the first DeepCore string was deployed and commissioned.

3.3.5 DOMs

Each DOM consists of a 25 cm diameter photo-multiplier tube (PMT) a main-board housing most of the DOM electronics, a 2 kV power supply for the PMT, a signal delay board as well as a "flasher" board, holding 12 LEDs. All components are housed in a 13 mm thick glass sphere which is filled with Nitrogen at a pressure of roughly 500 hPa. A flexible gel provides optical coupling and support between the PMT and the glass
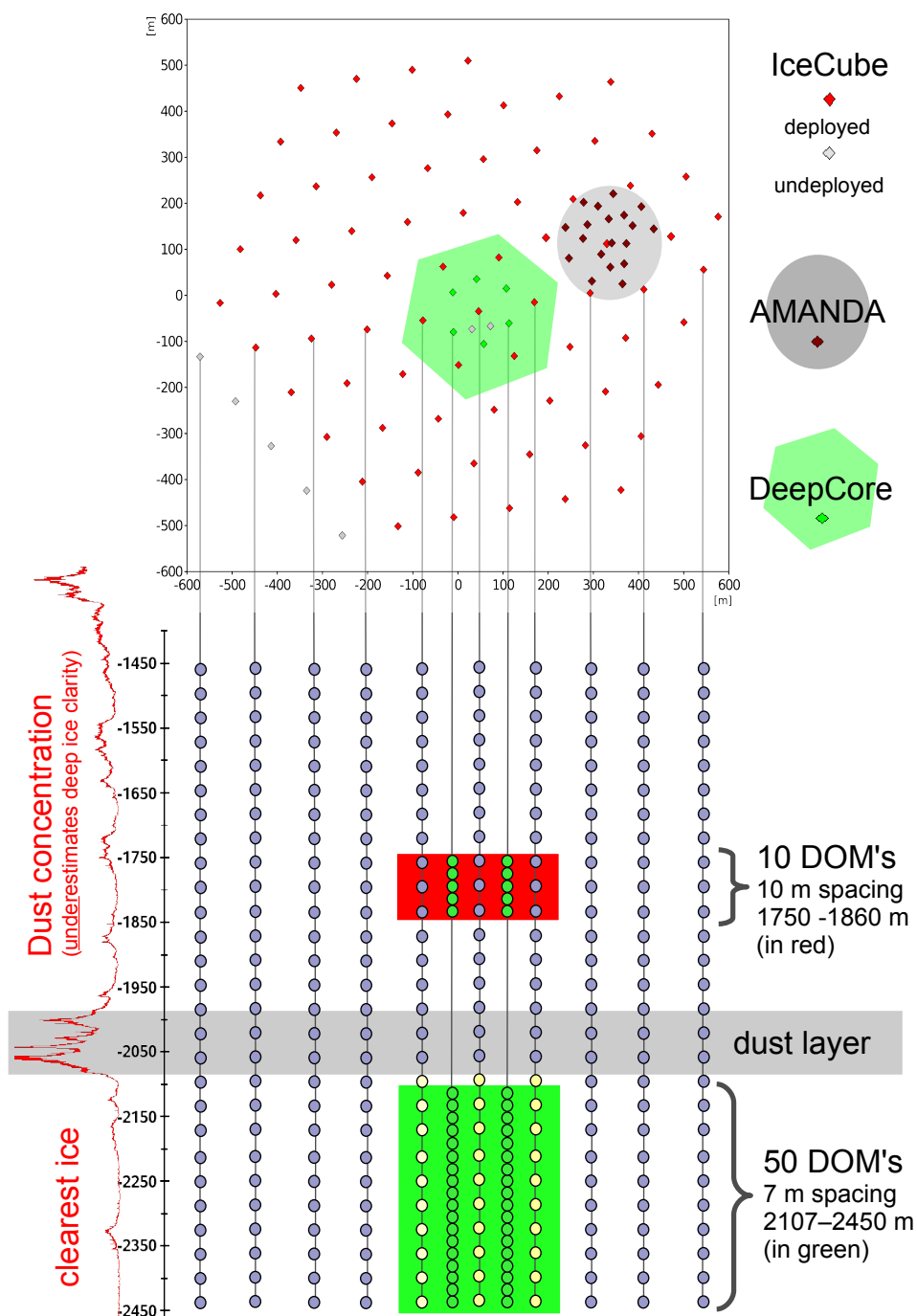
Figure 3.8: Schematic view of IceCube and DeepCore - In the top of the scheme the current IceCube deployment status of 79 strings is given along with the still to deployed strings (in gray). The DeepCore volume is indicated by the green background.
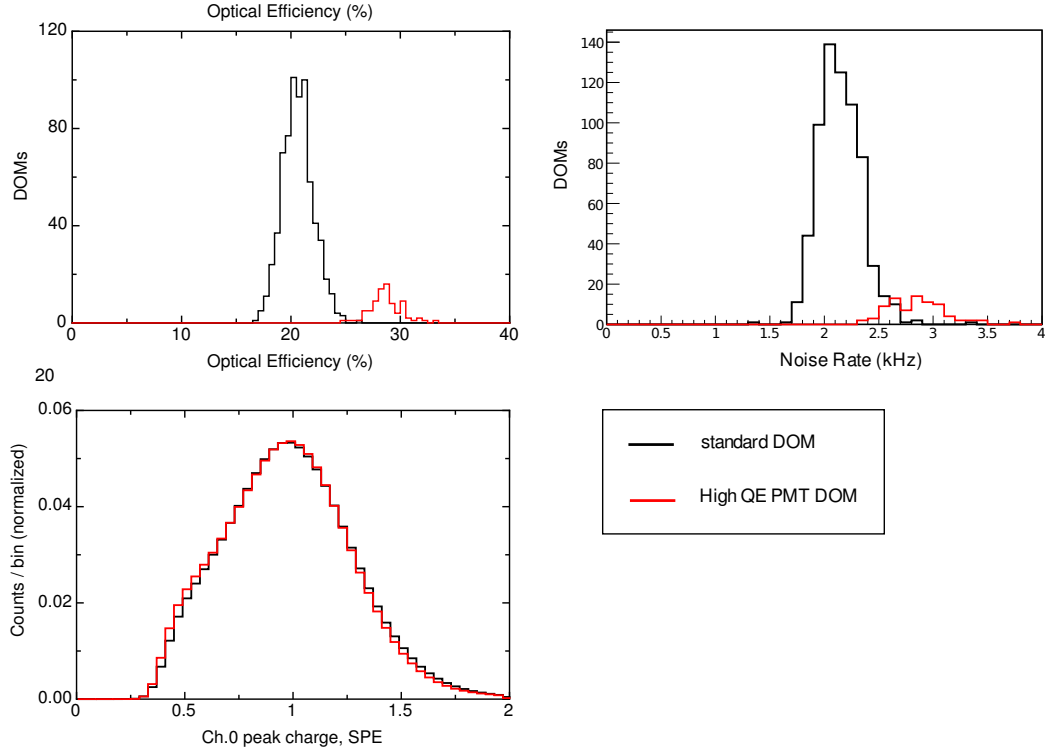
Figure 3.9: Final acceptance test (FAT) results of standard and HQE DOMs -
Top left: Optical efficiency at 405 nm; Top right: Noise rate; Bottom left: Charge response.
Black line: standard DOMs; red lines: High QE DOMs.

sphere.

The PMT [41] used in the IceCube baseline configuration (type Hamamatsu R7081-02) has 10 dynodes which are driven at a voltage of ~ 1300 V to provide an amplification of approximately 10^7. The bi-alkali cathode has a peak quantum efficiency of ≈ 0.25 at a wavelength of ≈ 390 nm. This peak position is almost ideal considering the Čerenkov spectrum and the wavelength cutoff at ~ 350 nm forced by the DOMs glass sphere. The glass sphere of the PMT is built from custom-made low-radioactivity glass. The special PMTs used in DeepCore strings (strings 81-86 and lower half of string 36) are of the same built except for a different cathode material that has a 40% increased quantum efficiency (type Hamamatsu R7081-MOD).

The dark noise of the PMTs is mainly due to thermally released electrons and radioactive decays and scintillation coming from the glass sphere. It amounts to ~ 300 Hz at -40°C [41]. The high quantum efficiency (HQE) PMTs have a $\sim 35\%$ increased noise rate. When installed in the complete DOM structure and deployed to the ice the total

dark noise rate of a DOM is ~ 500 Hz (~ 700 Hz for HQE DOMs). In Fig. 3.9 results of laboratory final acceptance tests (FAT) of later deployed DOMs are shown for DOMs with standard and with HQE PMTs. These tests have been performed at a temperature of $-45°C$, which corresponds to the temperature of the ice at the deployment depths. The increased quantum efficiency, measured at 405 nm, is clearly visible in the upper left plot, while the increased noise rate can be taken from the upper right plot. The high noise rates, compared to the numbers given above, are due to the laboratory setup and are only as low as reported when finally deployed deep in the ice. The plot on the lower right of Fig. 3.9 shows the charge response of both kinds of DOMs which are virtually alike. The high QE PMTs give a slightly lower peak-to-valley ratio in the pulse-height spectrum, which should not have an influence on the performance.

The analog signal of the PMT is digitized by two Analog transient Waveform Digitizers (ATWD) and one fast analogue digital converter (fADC), which are installed on the DOMs main-board. The ATWDs are only read out if the analogue signal crosses a certain threshold, which is determined by a discriminator. In order to provide the ATWDs with the time to react on the discriminator signal, their readout is delayed by 75 ns. The ATWDs sample the waveforms in 128 parts at a rate of 300 MHz, providing a coverage of ≈ 430 ns. Each ATWD has four input channels of which 3 are fed with different amplifications of the PMT signal (0.25x, 2x, 16x). This provides a high dynamic range, as the lesser amplified channels are only read out if the higher ones saturate. The fourth ATWD channel can individually be connected to one of two 4 channel multiplexer chips which sample information on the DOM status including timing and local coincidence.

Additionally to the very detailed ATWD sampling the fADCs sample rate of 40 MHz and 256 channels provides a much longer coverage of 6.4 μs at less accuracy.

The "flasher" board has 6 LEDs pointing horizontally and 6 LED pointing upwards in a 45° angle. They are operated at a wavelength of 405 nm and are used for calibration and verification of ice-properties, timing and DOM positions. As these flashers are essentially point sources they can also be used to tune cascade reconstruction algorithms. Both length and brightness of a flash are variable.

A full description of the DOM structure and performance is given in [40] and a detailed study of the PMT characteristics is given in [41].

3.3.6 Local coincidence

As a measure to reduce noise contribution in the taken data, each DOM also has a circuitry for implementing a local coincidence requirement between DOMs. If a DOMs
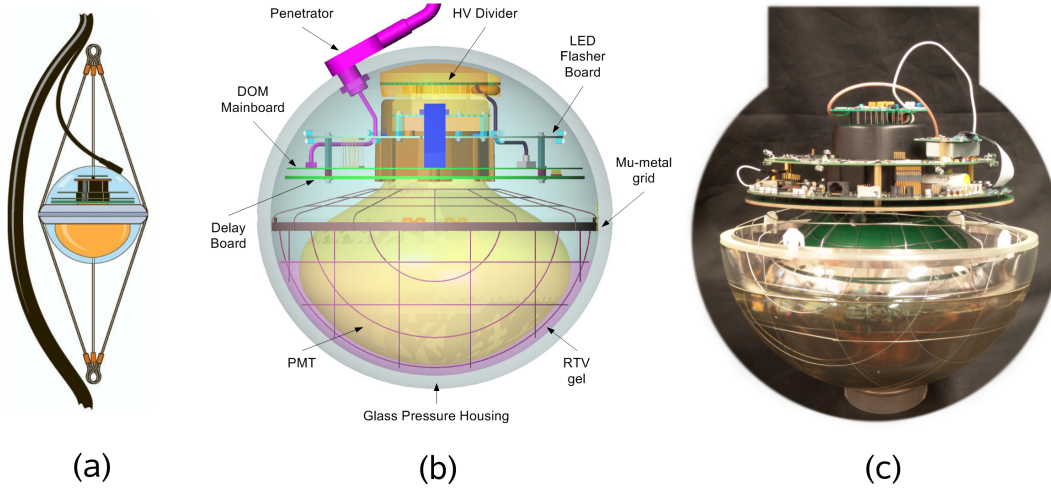
Figure 3.10: Digital Optical Module (DOM) - (a) Sketch of a DOM on a string with support cable. **(b)** Sketch of the DOM composition. **(c)** Photographic image of a DOM before closing.

discriminator is fired, it sends a signal to its neighboring DOM to provide a coincidence check. The DOMs can pass this signal on to check coincidences also with next-to-next or further away lying neighbors. The coincidence time window is set to $\pm 1\,\mu$s around the time of a DOM launch. The condition where only DOMs with at least one or more hits on one of the four nearest neighbors are read out is called "hard local coincidence" (HLC). This has been the standard operating mode in the first years of data taking in a growing IceCube detector. In current data taking mode all DOMs are read out, but only those fulfilling the HLC requirement are counted in the trigger logic (see next section). Furthermore the kept hit information of DOMs not fulfilling the HLC condition is reduced to the launch time and the three fADC charge bins around the highest sample point. This mode is known as "soft local coincidence" (SLC).

3.3.7 Trigger system

The IceCube trigger system is very flexible and able to accommodate various trigger conditions at the same time. In the trigger logic only HLC hits are taken into account. The most relevant triggers for this work are:

- the **Simple Multiplicity Trigger** (SMT), which calls for a minimum amount of hit DOMs in a designated time window. Currently the main IceCube trigger runs at a multiplicity $\geq$8 within a time window of $5\,\mu$s ("SMT8"). It takes into

account all DOMs located in the ice.

- the **DeepCore SMT trigger** is an SMT trigger of multiplicity ≥ 3, which only counts hits on the modules associated to DeepCore. It uses a time-window of $2.5\,\mu s$

- the **string trigger** is a dedicated low energy trigger requiring, in its current form, that 5 out of 7 subsequent DOMs on a string are launched within a time window of $1.5\,\mu s$

The overall rate of triggers in first test runs of the current configuration with 79 deployed strings is at $\sim$ 2.3 kHz. The DeepCore SMT3 trigger fires at an average rate of $\sim$ 180 Hz.

3.3.8 Data storage and filtering

The isolated location of the IceCube detector at the South Pole implies that the taken data can only be brought to the institutes in the north for analysis by storage tapes or via satellite transmissions. The transport of tapes is slow and only possible during the austral summer. On the other hand satellite bandwidths are limited and the large amount of data taken by IceCube ($\sim$ 500 GB/day) has to be filtered before transmission.
A number of different filters are applied for the various analysis chains, which may have large overlaps, and reduce the event rate by more than an order of magnitude. The full data stream is recorded to tape and is brought to the north once a year.

3.3.9 Drilling and deployment

The holes needed to deploy any IceCube string into the ice are drilled in a two step process. First, to drill through the $\sim$ 100 m thick "firn" ice layer, a specialized "firn drill" is used in which hot water is pumped through a cone-shaped spiral of copper tubes. This tubes are in direct contact to the ice which is molten without adding extra hot water, as this would soak into the surrounding, rather porous, firn ice, rather than melting the ice in the appointed direction.
Below the firn ice a dedicated 5 Megawatt hot water drill is used to drill deep into the ice. The hot water for this drill is provided by an array of heaters and then pumped through hoses into the drill head. The drill head is attached to a heavy weight stack and shoots a jet of hot water into the bottom of the hole. The whole procedure of drilling, including the movement of the drill equipment to a new hole location, takes

Season	deployed (total)	deployed (season)	deployed DC (season)
2004/05	1	1	-
2005/06	9	8	-
2006/07	22	13	-
2007/08	40	18	-
2008/09	59	19	1
2009/10	79	20	5
2010/11	*(86)*	*(7)*	*(2)*

Table 3.1: IceCube deployment schedule

2-3 days, with the drilling process itself taking $\sim$ 24 h. The deployment of a string into the hole is usually finished in $\sim$ 12 h and well before the hole refreezes. The final depth of each string is measured after deployment using pressure sensors at the bottom of each string.

3.3.10 Deployment status and plans

The first IceCube string was deployed in the austral summer 2004/05 and since then each season has seen an increase in the number of newly deployed strings, making the construction of IceCube a major success. Table 3.1 gives the configurations of IceCube through the years of construction. Currently 79 strings are installed in the ice and taking data. Of these 79 strings, 6 are dedicated DeepCore strings, which have been deployed in the last two seasons. In the final season 2010/11 two more DeepCore strings will be deployed along with the final five baseline IceCube strings and corresponding IceTop tanks.

The current configuration already provides three rings of strings around the central DeepCore volume, which are needed for an effective veto against atmospheric muons (see chapter 4).

3.4 Simulations

The simulation of events in IceCube is done using Monte Carlo (MC) methods. While the simulations of extra-terrestrial signal neutrinos necessarily are separated from the background simulations, this is also true for the atmospheric neutrinos, even though they origin in the same cosmic ray air-showers as the background atmospheric muons.

The six orders of magnitude larger flux of atmospheric muons in IceCube makes this separation an appropriate decision, as long as one looks for upwards-moving neutrinos. The new development of the atmospheric muon veto technique, and the subsequent effect of the atmospheric neutrino veto (see chapters 4 and 6) raise new simulation needs, in which both major backgrounds to searches for extra-terrestrial neutrinos are not decoupled. However, these techniques are currently under development and the simulations used for the work of this thesis typically follow the following steps:

1. **Event generation:** Atmospheric muon background events are obtained from full air shower simulations using an adapted version of the CORSIKA [27] code. Neutrino events are produced using an IceCube adaption of the ANIS [53] package, called "NeutrinoGenerator".

2. **Muon propagation:** The energy loss of muons in the ice by the processes described in section 3.1.2 is simulated using the "Muon Monte Carlo" (MMC) [22]. This code can take into account the stochastic nature of the processes at different levels of accuracy, allowing for eventual systematics studies. It is also capable of propagating neutrinos.

3. **Čerenkov light yield:** The Čerenkov light emission within the detector volume can be simulated using the Photonics package [74]. With Photonics one can create, in a tabulated form, the photon flux distributions through a specified medium for a given input light source. In this case the medium is the South Pole ice, described by an ice model which is derived from the results of [39] and the light source is either a muon or a cascade. Photonics takes into account the heterogeneity of the ice and the anisotropy of the emitted light. It also provides probability density functions for arrival times of independent photons, as well as the number of photons at the detector positions.

4. **Detector response:** The simulation of signal shapes, from the photon yield provided by the Photonics tables, recorded in IceCube DOMs is done by a dedicated IceCube "HitMaker" software which takes into account the DOM hardware characteristics.

Here we will give a short introduction to the event generators CORSIKA and NeutrinoGenerator, as these simulations form the backbone of any analysis in IceCube. This is especially true for a design study, such as the one done for DeepCore.

3.4.1 CORSIKA

CORSIKA (COsmic Ray SImulation for KAscade) [27] is a detailed MC program to simulate full extensive air showers in the Earths atmosphere from all typical primaries. It has been first devised as a tool for the KASCADE [6] air shower experiment, but is today widely used in many experiments involving air showers. For a detailed description of the code see [27]. CORSIKA simulates the particle interactions of primary and secondary particles with air nuclei, as well as the propagation of all shower particles (including neutrinos) to a specified observation level. It can be tuned to use a wide range of hadronic interaction models, including VENUS [93], DPMjet [83], QGSJET [67] and SYBILL [49] for high energy particles and GHEISHA [47] for the lower energetic ones. Electro-magnetic cascades can be either fully simulated using EGS4 [80] or can be treated by the analytical NKG formalism [59], which saves processing time. The latter approach is typically chosen in IceCube since the electro-magnetic component of an air-shower is of minor interest to IceCube. For the purposes of IceCube, CORSIKA has been adapted and partially modified to meet the needs of a volume detector within the ice, rather than a flat surface detector for which it was originally designed. To simulate the complete background muon energy range, primaries are typically simulated from 600 GeV up to the highest observed cosmic ray energies at 10^{11} GeV. The primary energies follow a power-law spectrum with an adjustable spectral index usually chosen to be 2.7. The fluxes of the different primary nuclei can be taken e.g. from [62]. Since only muons of sufficient energy to reach the detector are of interest, a lower cut on the muon energy is made typically at 273 GeV [14]. Showers can be oversampled with their core position being randomized in a way that guarantees the correct (isotropic) flux using the program "ucr" [14]. The typically chosen oversampling factor is 2.

3.4.2 NeutrinoGenerator

NeutrinoGenerator is an implementation of ANIS (All Neutrino Interaction generator [53]) into the IceCube software framework. Neutrino events of all three flavors can be simulated. The neutrinos are injected on the surface of the Earth with an energy following a power-law spectrum. From the surface they are propagated to the detector volume, taking into account all possible interactions within the Earth and involving a density model of the Earth. If a neutrino interacts in the Earth it may either be absorbed (CC interaction) or regenerated at lower energy (NC interaction). In the special case of τ production in ν_τ interactions, the ν_τ is regenerated correctly in the decay of the τ at a lower energy.

Around the actual detector volume a cylindrical interaction volume, with the cylinder axis chosen along the neutrino direction, is defined. The neutrino is forced to interact at a random position inside this volume and an interaction probability is calculated from the cross-sections and the length of the interaction volume. Secondaries are propagated in the interaction volume until exit. The interaction volume is typically defined in a way that all light created from a particle interaction which could be seen by a module is contained. The length of the cylinder can be made energy dependent to accommodate the greater muon range at large energies.

A set of neutrino events produced with a specific spectral index can be re-weighted to fit any desired spectral shape. The spectral index of the simulation will then be chosen according to the statistics needed in the energy region of interest.

3.5 Event reconstruction

In this section we will shortly explain how, from the measured (or simulated) detector response, the nature of the event can be (at least partially) extracted.

The first step in this chain is the interpretation of the recorded waveforms. These have a length of $6.4\mu s$ (fADC) and $\sim$430 ns (ATWD), respectively. This waveform information, along with the timing and local coincidence information, is referred to as a "DOM launch". But, the waveforms may comprise one or more hits of photons, with each photon ideally giving a characteristic pulse in the measured voltage. These pulses are extracted from the waveforms by an waveform analyzing tool ("FeatureExtractor") which will provide a set of extracted pulses, each with a new time and a charge value, obtained from the integration of the pulse. The charge is often measured in units of photo electrons (PE), where 1 PE is the average charge response to a single photon hitting the PMT's photo cathode (single PE, SPE). If multiple photons hit the cathode in short time so that the single pulses can not be resolved, this is called a multi-photo electron (MPE) pulse.

While the raw DOM launch time is typically used for hit cleaning and can also be used in the veto algorithms presented in the next chapter, the extracted pulses are used for event reconstructions. Depending on the physics analysis and the aimed signal, dedicated reconstruction algorithms are used. For the reconstruction of muon tracks there are two classes of techniques. One class comprises the first guess algorithms, which were optimized for computational speed to be run on-line at the South Pole. With the development of faster processors their task has shifted more to providing a seed to likelihood reconstruction techniques which form the second class of algorithms.

The exact procedure of these reconstructions is of minor importance for this work, as the analyses within the DeepCore and veto design studies were mainly performed at a low analysis level. For further information on the basic reconstruction techniques, see [37].

3.6 Analysis strategies in IceCube

A great variety of analyses are done using IceCube data. Searches for neutrino point sources, using muon neutrinos, form the spearhead of the IceCube research efforts, but many other analyses have, or are being done. These include, among others, searches for

- a **diffuse neutrino flux:** As astro-physical neutrinos are expected to have a harder spectrum, these analyses look for a deviation from the atmospheric neutrino spectrum at the highest observed energies

- **cascade-like events:** Events induced by electron or tauon neutrinos have a cascade-like topology. Up to today no unambiguous cascade event has been observed.

- **Exotic particles:** Magnetic monopoles, Kaluza-Klein dark matter, and other exotic particles that have been theorized about, are expected to show distinct event topologies.

- **Supernova neutrinos:** A supernova within our galaxy will produce a large amount of low energetic neutrinos. Even though they can not be measured individually, the shear amount of low energy neutrino interactions should lead to a significant increase in the observed detector noise rate. Dedicated triggers and filters are in place to look for such events.

Here, we will just give a short introduction into the procedure of a point source search. These searches can be differently focused and optimized. Apart from the clustering of events at a potential source position, also other information can be used to optimize the search results and extract the most information from the measurements. This includes other measured (or inferred) quantities such as the neutrino energy, but also external information, e.g, the timing information in light-curves observed by radio, x-ray or gamma-ray telescopes (multi-messenger approach). Searches for gamma-ray bursts (GRBs) are a special case of the latter example. But also the searches for a dark matter induced neutrino flux from the sun are, in essence, point source searches.

In IceCube two basic approaches to a point source search have been used. A binned method, which essentially looks for events in a fixed circular bin around a potential source position and an unbinned method, which we will shortly introduce here. A detailed description of this analysis method can be found in [11].

3.6.1 Point source analysis

The data of a neutrino telescope, as used in a muon neutrino point source search, typically consist of a set of measured events which have a time, a reconstructed direction and (eventually) a reconstructed energy. In the approach presented here, we neglect the timing and energy information and concentrate on the directional information.
The data at any point in the sky can be interpreted in two ways. First, by a null-hypothesis H_0, assuming that the data consist only of background events, and second, by a source-hypothesis H_S, assuming that the data comprise signal as well as background events. The probability density function $P(data|H)$ of measuring the observed data given either of these hypothesis, can be calculated from knowledge on the spatial distribution of astrophysical and atmospheric events, respectively.
Suppose a test of a potential source at the known position $\vec{x}_S$ using a set of measured events with reconstructed locations $\vec{x}_i$. Then the probability density function can be described by the likelihood function

$$\mathcal{L}(\vec{x}_S, n_S) = \prod_N \left(\frac{n_S}{N} \mathcal{S}_i + \left(1 - \frac{n_S}{N} \right) \mathcal{B}_i \right). \tag{3.13}$$

Here n_S is the number of signal events. $\mathcal{S}_i = \mathcal{S}_i(\vec{x}_i, \vec{x}_S)$ is the source probability density function, which in this case is defined solely by the spatial probability density. The latter can be obtained from directional likelihood reconstruction techniques and is well described by a Gaussian:

$$\mathcal{S}_i(\vec{x}_i, \vec{x}_S) = \frac{1}{2\pi\sigma^2} e^{-\frac{|\vec{x}_i - \vec{x}_S|^2}{2\sigma^2}}. \tag{3.14}$$

Here, $|\vec{x}_i - \vec{x}_S|$ gives the space angle between the event and the source direction and σ is the error estimate of the reconstruction. For a neutrino telescope in ice this error will typically be larger then the vertex angle between the observed muon and the incident neutrino and thus the vertex angle is usually neglected. At the low energies aimed for with DeepCore, this may not be the case anymore, assuming that dedicated low-energy reconstruction can be improved.
The function $\mathcal{B}_i$ in equation 3.13 describes the background probability density. This is

uniform for a given declination δ and typically only events within a declination band $\delta_S \pm \delta_{band}$ around the source declination are considered. $\mathcal{B}_i$ is then simply defined by

$$\mathcal{B}_i = \frac{1}{\Omega_{band}}. \tag{3.15}$$

As a consequence, the likelihood function $\mathcal{L}(\vec{x}_S, n_S)$ has only one unknown variable, the number of signal events n_S. By maximizing the likelihood over this parameter (or minimizing $-\log \mathcal{L}$) one can obtain the best fit value $\hat{n}_S$.

To estimate the significance of such a result, the obtained likelihood is related to the likelihood of the data agreement with the null-hypothesis H_0. Typically one defines the test statistic λ as

$$\lambda = -2 \cdot sign(\hat{n}_S) \cdot \log \left[\frac{\mathcal{L}(\vec{x}_S, 0)}{\mathcal{L}(\vec{x}_S, \hat{n}_S)} \right]. \tag{3.16}$$

Without the factor $sign(\hat{n}_S)$ the test statistic would never be negative and the signum factor is therefore used to clearly separate under-fluctuations. The larger λ is, the larger is the probability that the observed set of events around the tested source location is actually source related.

One can easily extend this method to a full sky search by performing the likelihood estimation on each point of a grid distributed over the whole sky. If a reasonable energy estimate is at hand, the source and background probability functions $\mathcal{S}_i$ and $\mathcal{B}_i$ can be extended to include the probability of observing the given event under the assumption of a specified source spectrum (usually a power law of the form $\propto E^{-\gamma}$).

4

Atmospheric muon veto techniques

Neutrino telescopes such as IceCube have been devised to mainly look for high energy neutrino events that have passed through the large matter of the Earth. In this way the background of atmospheric muons is rejected efficiently. Only at the highest energies (>PeV), where the atmospheric muon background can be neglected, it is possible to search for a signal from above. Other neutrino detectors however, such as Super-Kamiokande [50] or Borexino [38], which aim for the detection of neutrinos of significantly lower energies, have ever since also employed active vetoes against the atmospheric muon background. Thereby they are able to detect neutrinos also from the hemisphere of their own location. These detectors consist generally of a closed tank filled with water (or a scintillating fluid) which is equipped with photo-multiplier tubes. Thus they have clearly defined, opaque, borders. Such a clearly defined detector volume allows for a separation of events that are through-going (i.e. leaving also light outside the volume) and events that start within the fiducial volume. This enables a separation of the atmospheric muon background from the neutrino induced signal if the interaction vertex is within the fiducial volume. IceCube has no such clearly defined border, but the intriguing ability of the mentioned experiments triggered thoughts on how such a muon veto might be established in a km-scale neutrino telescope. If such a veto could be realized it would eventually open a complete new window of observations.

The main approach to realize an atmospheric muon veto in IceCube is to use a part of the detector to identify and reduce the muon background. It has already been investigated using AMANDA, but the position of AMANDA w.r.t. IceCube, in the

top and off center, is not ideal for such an approach. DeepCore, on the other hand, will be positioned at the center and bottom of the detector, which is ideal for such a veto technique in IceCube. In the complete IceCube volume about 10^6 times more background atmospheric muon events are observed then events induced by atmospheric neutrinos. When a simple multiplicity trigger with 3 hits (SMT3) in DeepCore is required, this number is reduced by about an order of magnitude, setting the challenge to any muon veto technique to a background reduction by a factor of at least 10^5. The basic principle of all this techniques is to look for hits within the veto region. In the ideal case all hits caused by a (potentially) incoming muon and only these hits will be considered for the veto. In reality there is also a, relatively low, noise component (~ 500 Hz per DOM, see section 3.3.5) and a hit cleaning has to be applied previously to remove as many noise hits as possible, at a minimal loss of signal related hits.

In this chapter we first present the available hit cleaning techniques and then go on to discuss the muon veto algorithms. These consist of two parts. A hit veto and a cut on a reconstructed interaction vertex.

4.1 Hit cleaning

In the current data taking mode of IceCube (see chapter 3) all DOM launches within the detector read-out time are recorded. However, only launched DOMs fulfilling the HLC condition have the full waveforms recorded (SLC mode). Although the noise rate of IceCube modules is very low in comparison to a typical event duration (a muon needs $< 5\,\mu$s to cross the full detector volume), some tenths of noise related DOM launches are typically recorded per event. These noise hits are, in first order, distributed randomly throughout the detector (the correlated noise component is typically low), while signal related hits typically cluster along a track or cascade position. It is therefore sufficient to use relatively simple procedures to get rid of the noise component.

The set of HLC launches, provided by the hardware, represents an extremely "clean" sample which typically has only few percent of noise content. On the other hand a restriction to HLC Launches removes all single signal related launches, which amounts to an average fraction of lost signal hits of $\sim 30\%$. While for high energetic muon events, which leave a lot of light in the detector, this loss may be acceptable, these launches are essential for many other tasks, like e. g. the energy reconstruction of cascades. For a veto of atmospheric muons, every trace left by such a muon is of great importance. On the other hand a noise related launch may cause a veto of the desired signal events. Therefore an efficient hit cleaning is needed to both reduce the noise component and

also keep a maximum of the signal related hits.

In this section, we present two algorithms designed to fulfill this task. Both make use of the expected clustering of signal related launches in time and space. The first method is called the "R-T-cleaning" and is a classic method that has already been in use for AMANDA, for which no HLC information was available from the hardware side. The second algorithm has been developed in the course of this thesis and has been named the "Seeded R-T-cleaning". As the name suggests, it is based on the classic method and is aimed mainly at aiding low energy track- and cascade-reconstructions, rather than improving the veto technique. Both methods can therefore be considered complementary.

4.1.1   Classic R-T-cleaning

This cleaning is based on the assumption that noise hits are uncorrelated and therefore randomly distributed in time and space. On the other hand, hits induced by an actual physics event are mostly clustered in time and space. Therefore only hits are kept which have an accompanying hit within a distance **R** and a time **T** (see figure 4.1). The default settings which have been used throughout the DeepCore design study are

- R = 150 m

- T = 1000 ns

4.1.2   Seeded R-T-cleaning

The seeded R-T-Cleaning is based on the, previously discussed, classic R-T-Cleaning, but also makes use of the HLC information. It is an iterative method which, instead of applying the R-T condition to every hit, starts out by only keeping all HLC hits. In a second step, SLC hits which lie within the R-T range of the already kept (HLC) hits are added to the list of kept hits. This step is repeated iteratively until stability.

4.1.3   Time-window cleaning

In addition to the cleaning of isolated hits, a time-window cleaning is often applied. With this method only hits within a specified time window are preserved and all others are rejected. The length of the time window is usually an input parameter, while the start time of the window is optimized in away that a maximum number of hits is found in the time window.
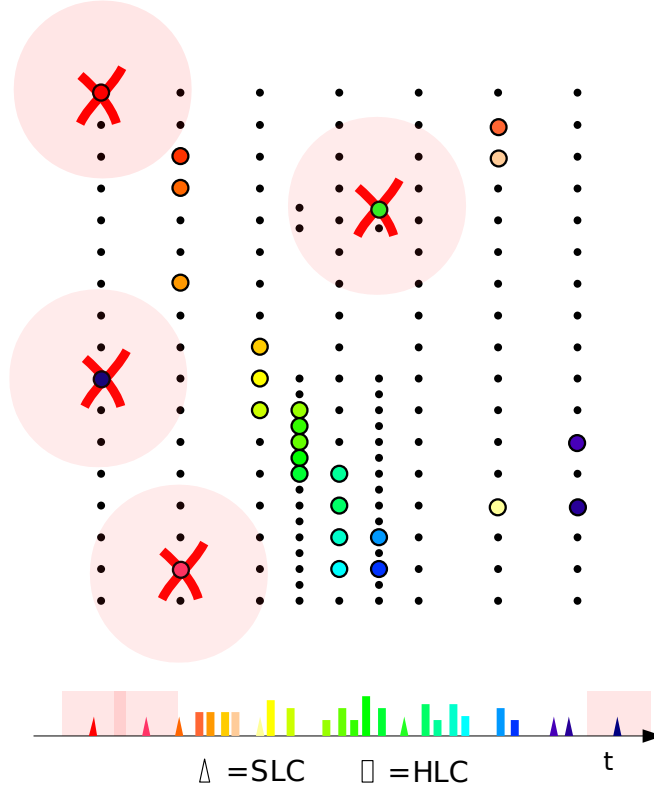
Figure 4.1: Classic R-T-Cleaning - Hits without a accompanying hit within a maximal distance R and maximal time difference T are cleaned out.

A typical time window size in IceCube is 5 μs, which roughly corresponds to the time a relativistic muon needs to travel the full diagonal of the detector.

4.1.4 Performance tests

The performance of the classic and new seeded R-T-Cleaning can be seen in figure 4.2 in comparison to the HLC hits. The spatial distance limit R and maximal time-difference T used for the classic and seeded R-T-Cleaning are in both cases R=150 m and T=1000 ns. The figure shows that the fraction of signal related hits that is kept by the algorithms is much improved w.r.t to the set of HLC hits for both methods, with a slightly better performance of the classic R-T-Cleaning. The fraction of noise hits in the finally kept hit sample however is much improved for the Seeded R-T-Cleaning w.r.t. the classic one. It becomes comparable to the cleanliness of the HLC hits, with a large majority of events having a noise hit fraction of less then 10%. However, there are much more signal related hits saved then for HLC. These results are quantified in
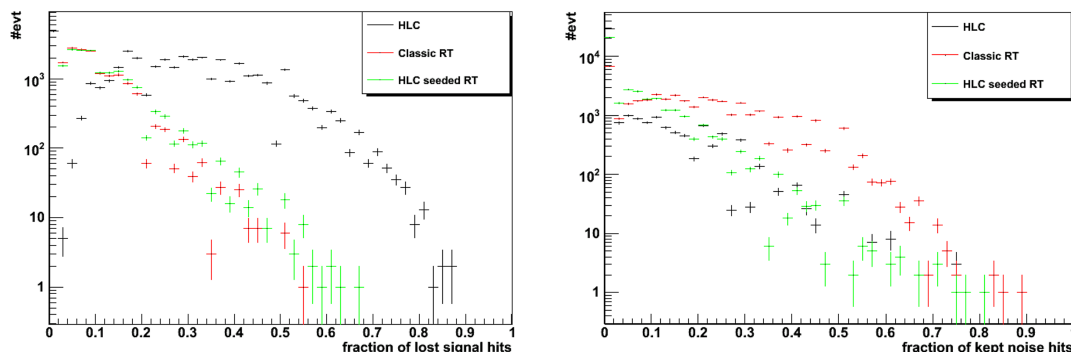
Figure 4.2: Performance of the different hit cleaning methods - Left: Fraction of lost signal hits; Right: Fraction of kept noise hits in all kept hits. Black: HLC hits, red: Classic R-T cleaned hits, green: Hits cleaned with seeded R-T-Cleaning.

	HLC	Classic R-T	Seeded R-T	SLC (no cleaning)
Kept noise hits (in all)	3%	17.8%	5.2%	71.0%
Kept signal hits	72.7%	95.9%	95.2	100%

Table 4.1: Hit cleaning performances: Fraction of lost signal (physics) related hits and fraction of noise hits among all kept hits for HLC, classic and seeded R-T-Cleaning. Produced from unweighted neutrino-generator data with a spectrum E^{-2}.

table 4.1, where the mean of the distributions from fig. 4.2 are given (in case of the signal hit fraction it is 1 - mean). The seeded R-T-Cleaning is a new powerful tool for noise hit cleaning, however, with this method the signal hits, which are still lost, are not randomly distributed anymore, as is (mostly) the case for the classic cleaning. The lost signal hits are mainly isolated hits, far away from the core of the event (e.g. the HLC hits). This has been shown to be a limitation for the veto algorithms (described below) where even single and far away hit can be of key importance for the rejection of atmospheric muons.

4.2 Basic veto algorithms

In order to distinguish a downwards-moving neutrino induced signal event from the large background of atmospheric muons, it is necessary to observe the interaction vertex of the neutrino or, in other words, it is necessary to ensure that the light emission in an event starts in the ice and is not coming from the surface. For IceCube, without
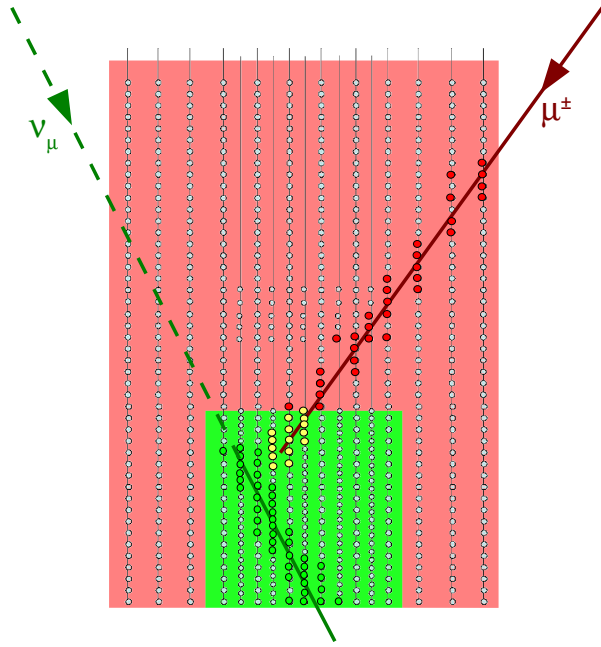
Figure 4.3: Basic principle of all veto algorithms - By definition of a fiducial volume (green) and a veto volume (red) a starting, neutrino-induced muon (green line) can be separated from atmospheric muon background (red line).

a detector border that optically separates the sensitive volume, this means that the interaction vertex has to be deep inside the detector volume. With 10^5 times more atmospheric muon events, the rare cases where a muon "sneaks" into the detector without leaving a hit on the outer detector layers, become the major challenge for a muon veto procedure. The basic idea of all veto algorithms presented here is therefore to divide the detector volume into an inner "fiducial volume" and an outer "veto volume", which is used to identify and reject the muons entering the detector from the outside. The principle is schematically shown in figure 4.3. The first and simplest approach to such a veto algorithm is to trigger only on the modules within the fiducial volume and to count the hit DOMs in the veto region. By rejecting events with more than a maximum number of allowed veto region hits the background can be reduced by a reasonable amount. However, such an algorithm fails to provide the necessary rejection power at an acceptable signal passing rate. To give the proof of feasibility for an atmospheric muon veto in IceCube, this ansatz has been developed further and combined with a newly developed likelihood based vertex reconstruction technique. The

improved veto penalizes veto volume hits according to their distance to the fiducial volume and together with the vertex reconstruction algorithm, which was run on the events surviving the veto, the first proof of principle was provided. Since then the veto algorithm has been further improved and a new algorithm has been devised, taking into account also the hit timing. Thereby the signal efficiency has been significantly improved. In this section we will first describe the geometrically penalized veto and the vertex reconstruction method. These are used in a first performance study, discussed thereafter, providing the proof of principle that an atmospheric muon veto in IceCube is feasible. Finally, we will describe the current improved veto algorithms and show the expected performances.

4.2.1 Geometrically penalized veto
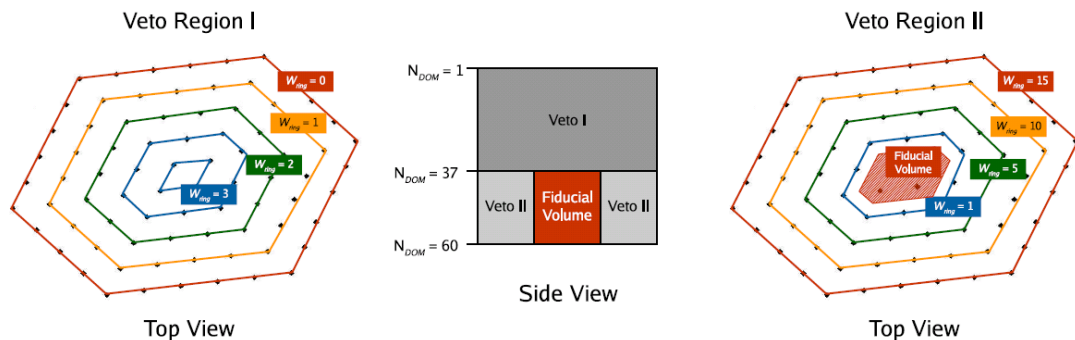
Figure 4.4: Veto regions in the geometrically penalized veto algorithm - The veto weight part given by the string layer as assigned in version A of the geometrically penalized veto is shown for the two separated detector veto regions. Picture from [43].

As the light attenuation in ice decreases exponentially with distance to the light source, an event that starts and stops in the DeepCore fiducial volume should primarily have hits in this region. The probability that a hit in the outer veto region is associated with such an event decreases likewise. In the reversed argument, this means that a hit in the outer region of the detector has a higher probability of being background induced. The geometrically penalized veto algorithm assigns a weight to each hit in the veto region depending on its distance to the fiducial volume.
Two versions of this algorithm, employing different weights, have been used during the veto and DeepCore design studies.

- **Version A:** The veto region itself is divided into two parts (see Fig. 4.4). A

"cap" (Veto I) consisting of all modules located higher than the fiducial volume (i.e. with OM numbers 1 to 37), and a "ring" part (Veto II), build from all veto DOMs surrounding the fiducial volume on the same height. In the cap region the weight W is assigned according to

$$W = 1000 \cdot \exp \left(-\sqrt{W_{ring}^2 + W_Z^2} \right) \quad , \tag{4.1}$$

where W_{ring} is depending on the veto ring layer as depicted in the left sketch of Fig. 4.4 and W_Z gives a weight depending on the depth of the veto hit according to $W_Z = (N_{DOM} - 1)/10$. N_{DOM} denotes the OM number. In the lower ring region the weight does not depend on the depth, but only on the veto ring layer. These numbers are optimized by performance tryouts and their absolute scale is arbitrary, although the exponential dependence in the top layer veto resembles roughly the light attenuation in ice.

- **Version B:** In this improved version the weights depend directly on the distance d to the surface of the DeepCore fiducial volume.

$$W = \exp \left(\frac{d}{75 \ m} \right) \tag{4.2}$$

The length 75 m corresponds roughly to the photon attenuation length in ice.

Events which trigger DeepCore are cut depending on the sum of weights of the hits in the veto regions.

The version B of the algorithm performs very similar to the version A and has been created to reduce directional biases, which are potentially introduced by the two-part veto volume, with two different weight assignments. Version A has been used in the first full veto study presented in this chapter. Version B was used extensively in the DeepCore design study (see chapter 5).

4.2.2 Vertex reconstruction

The final reduction of the atmospheric muon background is done by a cut on a reconstructed vertex position and a likelihood value, which estimates the degree of belief that the track is actually starting at this vertex. This algorithm has been devised by. J.-P. Huelss at the RWTH Aachen [64].

The algorithm requires the input of a track hypothesis, ideally given by track reconstruction algorithms. To reconstruct a vertex position, we trace back from each hit DOM to the reconstructed track using the Čerenkov angle of 41° in ice (see Fig. 4.5).
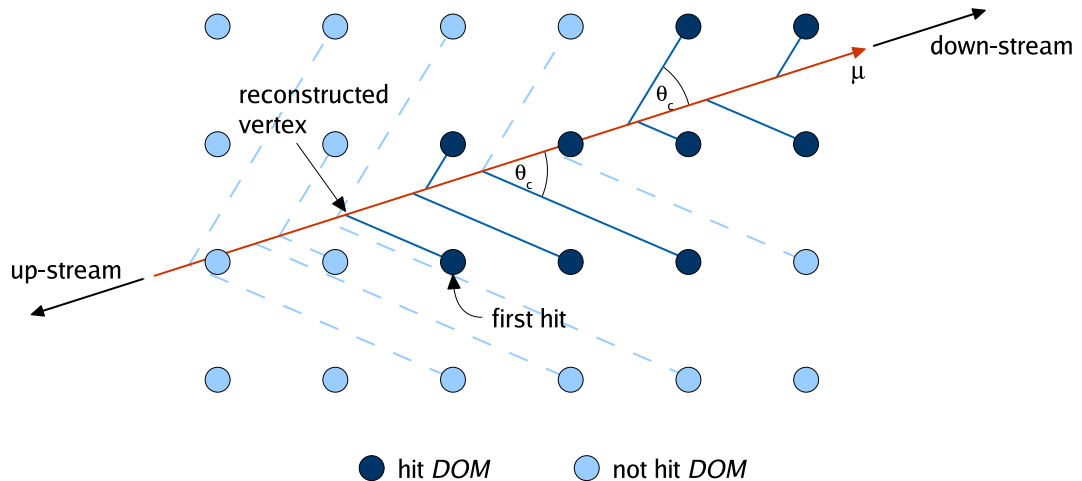
Figure 4.5: Vertex reconstruction - each hit is projected on to a (reconstructed) track under the characteristic Čerenkov angle. The first projected position on the track is considered as event vertex. Picture from [43]

This projection is calculated for all DOMs within a cylindrical volume of radius 200 m around the track and the DOMs are ordered according to this position. (Note that 200 m is large enough to contain virtually all photons produced by the track.) The projection of the first hit DOM in the up-stream direction defines the neutrino interaction (reconstructed) vertex. A reconstructed vertex inside IceCube indicates a potential starting (neutrino-induced) track.

Due to the large distance between neighboring strings, atmospheric muons may leak through the veto, producing their first hit deep inside the detector and thus mimicking the signature of a starting track. Therefore it is necessary to quantify for each event the probability of actually starting at the reconstructed vertex. To determine this starting likelihood, one first selects all DOMs without a hit and with a projection on the assumed track up-stream of the first hit DOM. The probability that each of these DOMs did not receive a hit is calculated assuming two track hypotheses: a track starting at the reconstructed vertex and a track starting outside the detector volume. Under the assumption of an external track, $p(\text{noHit}|\text{Track})$ is calculated. Here, for each DOM the probability of not being hit (in spite of the passing track) depends on track parameters (energy of the light emitting particle, position and direction of the track) and ice properties. The probability is calculated from the expected number of photo-electrons, taken from *Photorec* tables of the *Photonics* package [74], assuming Poisson statistics:

$$p_\lambda(\text{noHit}) = p_\lambda(0) = \frac{\lambda^0}{0!}e^{-\lambda} = e^{-\lambda}. \tag{4.3}$$

λ is the expected number of photo-electrons. Under the assumption of a starting track $p(\text{noHit}|\text{noTrack})$ is calculated, which is equal to the probability of a noise hit and can therefore be calculated from measured noise rates.
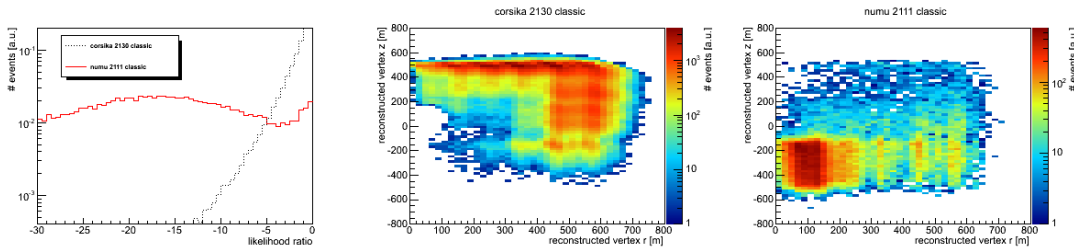
Figure 4.6: Distributions of the cut parameters of the vertex reconstruction - Likelihood ratio (left) and position of the reconstructed vertex for atmospheric muons from CORSIKA (middle) and atmospheric neutrinos (right) after L1 causal hit veto (see section 4.4).

The likelihood for the observed pattern of hit DOMs may now be constructed as the product of the individual hit probabilities. A track is classified as starting in the detector according to the probability given by the ratio of the likelihoods. For a clearly starting track this ratio is a negative number, and the larger the absolute value, the higher the starting probability for the track. To select tracks starting inside the detector, cuts are applied on the position of the reconstructed vertex and on the likelihood ratio. The distributions of the cut parameters are shown in Fig. 4.6. These distributions reflect the latest results at the time this thesis was written. The likelihood calculation involved with the vertex calculation has been under development when the first veto study started and following from that, the cut parameter values have changed and can only be compared to the values presented in the following study in terms of signal and background efficiency.

Preliminary studies are up to now utilizing the true simulated track, since dedicated low energy track reconstructions are still under development. Even though idealized, these studies strongly indicate that an overall background rejection of $> 10^6$ can be achieved at a reasonable signal passing rate.

Figure 4.7: Early 12 string layout of DeepCore - This layout has been used in the first full veto study with the geometrically penalized hit veto and the vertex reconstruction technique.

4.3 Performance study of the geometrically penalized veto and the vertex reconstruction method

The first study of the combined capabilities of the geometrically penalized hit veto (in its version A) and the vertex reconstruction technique has been done with a 12 string DeepCore design, which was considered in the early stages of the DeepCore design study (see chapter 5). Each of the 12 strings in this geometry was equipped with 40 standard IceCube DOMs (standard quantum efficiency PMT) at an inter-modular distance of 10 m from the bottom of the detector upwards (-2450 m to 2060 m). The strings are positioned in a 72 m spacing in the center position of the triangles formed by the central baseline IceCube strings (see figure 4.7). For the purpose of this study $\sim 2 \cdot 10^7$ atmospheric muon events were simulated using CORSIKA (see section 3.4.1), and $\sim 2 \cdot 10^5$ downwards-going signal muon neutrino events were generated using NeutrinoGenerator (see section 3.4.2). The latter were simulated with an E^{-2} spectrum

and later re-weighted for an atmospheric neutrino spectrum according to the Bartol model [9]. The detector response was simulated assuming a SLC data taking mode, which recorded the full waveform also for launches not fulfilling the HLC condition[1]. Events were triggered by an SMT 10 counting only launches in DOMs associated to DeepCore. A hit cleaning was performed using the R-T-cleaning algorithm ($R = 150$ m, $T = 1\,\mu$s) and a time-window cleaning keeping only launches within a 5 μs time window. With this setup and a cut on the sum of veto weights, rejecting all events with $W_{tot} > 60$, the background rejection factor was found to be $5 \cdot 10^{-4}$. This number is relates to all simulated background events and thus includes a reduction due to the triggering in DeepCore. The signal retention, on the other hand, was at about 13% of all simulated events. Note that many rejected signal events are actually passing through the veto volume and are thus removed necessarily. Thus the actual signal efficiency of events with an interaction vertex in the fiducial volume is significantly larger.

For the surviving events the interaction vertex was reconstructed using the algorithm discussed in the previous section, employing the true MC muon direction information. The distribution of this reconstructed vertices are shown in Fig. 4.8. For the surviving signal events the vertices are found to be in or close to the fiducial volume, as one would expect. However, for the surviving background events the vertex distribution shows unexpected features. For one, it was somewhat surprising to see the amount of events with a first hit deep in the detector volume (remember that the reconstructed vertex is the first Čerenkov-projection of all hits along the muon track). This emphasized the need to have three outer layers of strings and the complete upper half of the detector in the veto volume. Secondly, the vertices of the surviving background muons are not uniformly distributed around the DeepCore volume, but can be divided into two groups. One class of event vertices is clustered in a ring-like structure in the outer string layers and at a height corresponding to the top of the DeepCore volume, shortly below the dust layer. The second class of vertices is clustered above the fiducial volume in the center of IceCube. This "sombrero-hat"-like structure is explained by two different event classes, which are less effectively rejected by the veto. The first class, the "rim of the sombrero", is caused by events that have zenith angles of about 50°. These enter the detector from the side, in the region of the largest dust layer in the ice (see section 3.2). In this region the scattering and absorption lengths of light are reduced strongly and the probability to detect or reconstruct these events decreases. Some of these events leave their first hit only after leaving the dust layer again, resulting in the

---

[1]At the time of this study the growing detector was only reading out HLC launches and feasible SLC options were still under investigation
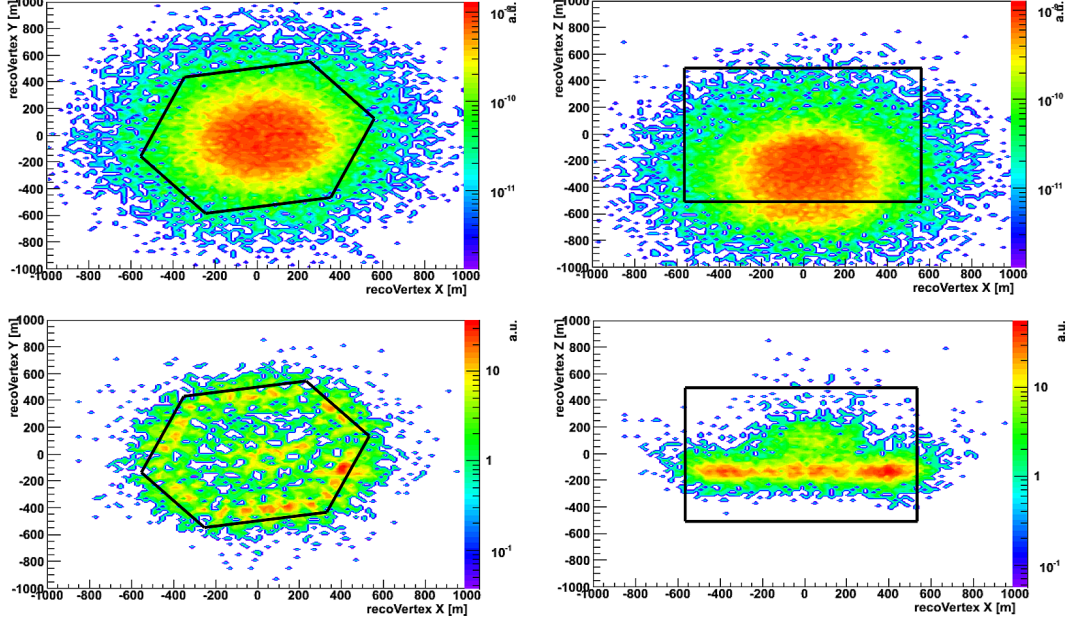
Figure 4.8: Vertex position of events surviving the geometrically penalized veto - Left panels: y- vs. x-position of reconstructed vertex; Right panels: z- vs. x-position of reconstructed vertex; Top: Downwards-going neutrino signal, Bottom: Atmospheric muon background. From [43].

observed structure. The second class of events, the "cap of the sombrero", are almost vertical events which enter the detector far away from any string and which do not come near to a string and give a hit until they are deep in the detector. This interpretation is backed up by the zenith distribution of the surviving events given in figure 4.9. The first peak at $\cos(180 - \theta) = -1$ (i.e. vertical downwards-going) is associated with the vertices reconstructed in the sombrero cap, whereas the second peak corresponds to the events coming in through the main dust-layer.

To finally reduce the muon background below atmospheric neutrino level, cuts on the vertex position and likelihood-ratio ($LLHR$) were chosen to reduce the background to 10 (1) remaining muon event (corresponding to an overall rejection factor of $2 \cdot 10^{-6}$ ($2 \cdot 10^{-7}$)) at an optimal signal retention. The restrictions on the vertex position consist of a cut on the height z_{vert} and the radial distance to the DeepCore center r_{vert}[1]:

- cut 1: $r_{vert} < 230$ m; $z_{vert} < -130$ m and $LLHR < -4.5$

---

[1]Note, that the here given cut values do not correspond to the parameter distributions shown in fig. 4.6. Due to coding changes in the likelihood method the cut parameter values were shifted.
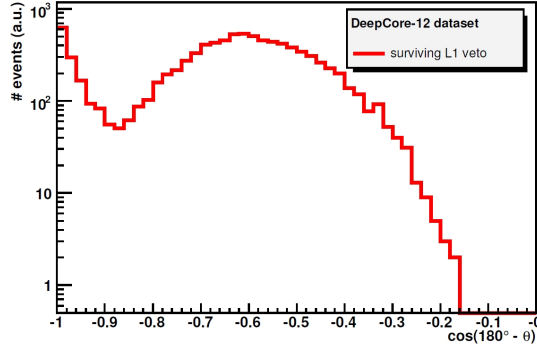
Figure 4.9: Zenith distribution of events surviving geometrically penalized veto - cos(180-θ)=-1 corresponds to a vertically downwards-going event. Plot from [43].

	all	geo. pen. veto	vertex cut 1	vertex cut 2
# background μ events	$\sim 2 \cdot 10^7$ (1.0)	9259 ($5 \cdot 10^{-4}$)	10 ($2 \cdot 10^{-6}$)	1 ($2 \cdot 10^{-7}$)
# signal ν_μ events	$\sim 2 \cdot 10^5$ (1.0)	25264 (0.126)	5383 (0.027)	3984 (0.020)

Table 4.2: Veto study - Numbers of atmospheric muon background and downwards-going muon neutrino events at the different stages of the veto process.

- cut 2: $r_{vert} < 220$ m; $z_{vert} < -150$ m and $LLHR < -6.5$

Table 4.2 shows the surviving signal and background event numbers (and fractions) at the different veto stages.

On the final veto level only 2.5% of all signal events could be retained, but this number is relative to all simulated down-wards going signal events. When only events which start within the DeepCore volume are considered the signal efficiency is at $\sim$ 6%.This corresponds to a muon neutrino rate of $\sim 2 \cdot 10^4$ Hz and ~ 6300 events per year.

This study marked the first proof that an atmospheric muon veto in IceCube is feasible and that a sensitivity for the southern hemisphere could be established. It thus added a strong argument for the construction of DeepCore and had a major impact on the design of the DeepCore extension.
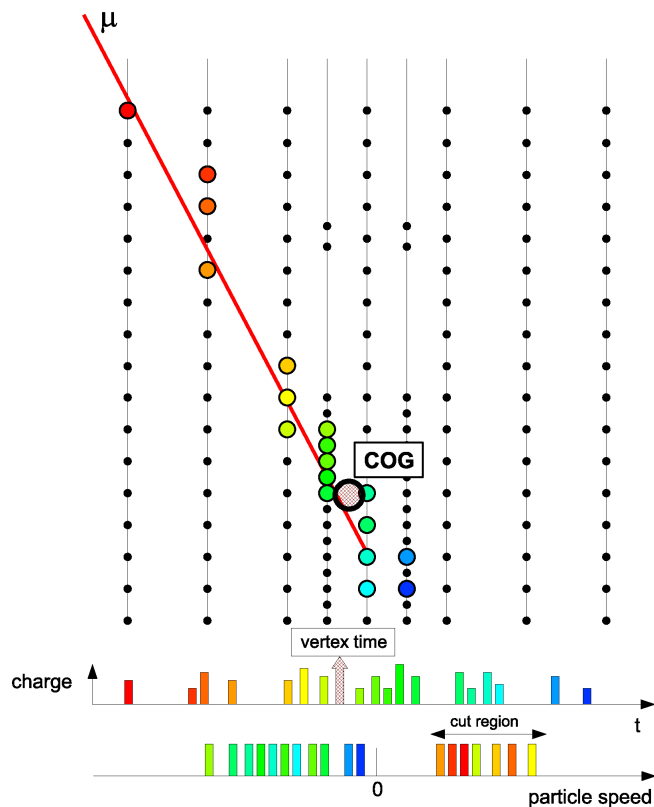
Figure 4.10: Causally related hits veto - Illustration of the DeepCore hit center of gravity (COG), vertex time and particle speed per hit.

4.4 New algorithm: Causally related hit veto

After the first proof that an atmospheric muon veto in IceCube with DeepCore was feasible, a further development of the veto techniques started. The aim was mainly to increase the signal efficiency, which was not optimal in the first algorithms. These previously described veto algorithms exclusively utilize the hit positions for event rejection. But also the time of a given hit holds important information on whether it could be associated with a DeepCore event. A new algorithm, which involves the timing information, was based on the assumption, that hits induced by a downwards-going muon are causally related by their distance and time, since the muon travels at the constant vacuum light speed. In this section we describe this new causally related hit veto algorithm, which marks the state-of-the-art for muon hit veto techniques in IceCube today. We will show its improved performance also after the full veto chain, including the vertex reconstruction technique, was applied, thereby giving the current status of

4. ATMOSPHERIC MUON VETO TECHNIQUES

IceCubes veto capabilities for DeepCore.

The causally related hit veto can be run with the raw information provided by a DOM launch, but also with pulses, extracted from the launches waveform. In the latter case, typically only HLC hits are taken into account. The numbers presented in this chapter all relate to the latter configuration, as this will be used in the filtering algorithms of IceCube in the upcoming data-taking period (see chapter 7).

Cosmic-ray air-shower induced muons move at speeds very close to the light speed in vacuum (c) and thus hits considered in the veto algorithm should be consistent with a particle moving downwards with $v = c$. To determine whether or not an event is rejected the average hit PMT position and an approximate start time (vertex time) of the DeepCore fiducial volume hits is computed (see Fig. 4.10). The interaction position is determined by using the subset of those hit DOMs that have times within one standard deviation of the first guess vertex time. This has the benefit of reducing the contribution from PMT dark noise and, by weighting the DOMs by their individual charge deposition[1], a reasonable center of gravity (COG) for the event is computed. By making the assumption that roughly all light in the DeepCore volume originates from the COG a more thorough estimation of the vertex time is possible. For each individual hit the time, light would have needed to travel from the COG to the hit module, is calculated and subtracted from the original PMT hit time. The average of these corrected PMT hit times is then considered as the vertex time.

Each hit in the veto region gets assigned a particle speed, defined as the spatial hit distance to the DeepCore COG divided by the time difference to the DeepCore vertex time. This speed is defined to be positive if the hit occurred before the vertex time and negative if it appeared after. Causally related hits in the veto region are generally expected to have a speed close to the speed of the muon, which is very close to the speed of light in vacuum (0.3 m/ns). Smaller speeds occur for hits that have been scattered and thus arrive late. Larger speeds are in principle acausal, but since the vertex time represents the start of a DeepCore event, whereas the COG defines its center, the particle speeds for early hits are slightly overestimated. Late hits on the other hand have typically lower speeds. Fig. 4.11 shows the probability of the occurrence of a particular particle speed per event. The dotted curve describes the simulated muon background from air-showers (CORSIKA) and the solid curve the atmospheric neutrino signal [9] with an interaction vertex inside DeepCore. The peak for the CORSIKA muons is slightly above +0.3 m/ns while muons induced by neutrinos in DeepCore

---

[1]Note, that this information is only available for extracted pulses, not for the raw launches.
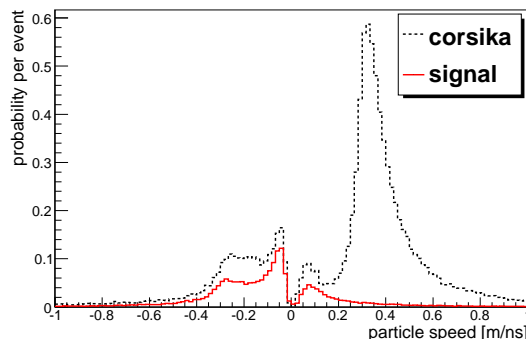
Figure 4.11: Causally related hits veto - Particle speed probabilities per event for atmospheric muons (dotted line) and muons induced by atmospheric neutrinos inside Deep-Core (solid line).

mainly give hits with negative particle speeds. The peak at positive speeds close to zero is mainly due to early scattered light. By cutting out all events with more than one hit within a particle speed window between 0.25 and 0.4 m/ns we achieve an overall background rejection on the order of $5 \cdot 10^{-3}$. If data taken in SLC mode are used, the additional information improves the veto efficiency by an order of magnitude, decreasing the signal efficiency only by a few percent. However, since the vertex reconstruction algorithm can fully compensate for the worse veto performance with HLC pulses, this configuration is currently favored.

	atm. μ (CORSIKA)	rejection	atm. ν_μ (Bartol)	eff.
main IceCube trig.	1900 Hz	-	-	-
DeepCore SMT 3	109 Hz	$5.7 \cdot 10^{-2}$	$4.98 \cdot 10^{-3}$ Hz	100%
veto L1	7.25 Hz	$3.8 \cdot 10^{-3}$	$4.95 \cdot 10^{-3}$ Hz	99.3%
veto L2	$1.55 \cdot 10^{-3}$ Hz	$8.15 \cdot 10^{-7}$	$1.82 \cdot 10^{-3}$ Hz	36.5%

Table 4.3: Background and signal rates after DeepCore trigger and causal hit veto

A study on the combined veto power of the causally related hit veto and the vertex reconstruction technique has been done using the final DeepCore design without the additional strings number 79 and 80. The rates and rejection factors for background and atmospheric neutrino signal (Bartol flux) are given in table 4.4. The rates at DeepCore trigger level are obtained with an SMT 3 trigger, the trigger condition currently running with the detector at South Pole. The signal has been defined as all neutrino events

with an interaction vertex inside the DeepCore fiducial volume, defined by a cylinder of 400 m height and 200 m radius around string 36, at the very bottom of the detector. The background rejection factor is related to the full IceCube trigger rate, given in the first row of table 4.4. The cuts on the reconstructed vertex position are given by

$$r_{vert} < 120m \quad , \qquad z_{vert} < -300m \qquad \text{and} \qquad LLHR < -12.$$

These numbers correspond to the parameter distributions shown in fig. 4.6.

With a background rejection as effective as for the geometrically penalized veto (see above) a much improved signal retention of about 51% (compared o 6% in the first study) is achieved. This improvement will be reflected in the sensitivity of any analysis looking for starting downwards-going muon events.

5

DeepCore design study

The history of the DeepCore project is by many means a remarkable one. As the low energy extension of the IceCube neutrino telescope, DeepCore adds a range of new research topics to the IceCube science scope and enhances the discovery potential of the entire project IceCube. But it is also a remarkable project because of the short time scale on which it has been developed. From the first proposal to the collaboration to the deployment of the first DeepCore string it has been less then 2 years. Given the hardware preparation needs only about a years time was left for the detector design. This short time scale was mainly a consequence of the demand to deploy the additional DeepCore strings within the already planned out IceCube deployment seasons. Once the physics motivation and capabilities of a low energy extension were given, it was apparent that a deployment along with the standard IceCube strings would be by far the most cost-effective solution. The fact, that fund raising for the DeepCore hardware and a compelling DeepCore design study have been achieved in this time, is a result of an intense collaboration among the participating (mainly European) institutes. Six of the eight dedicated DeepCore strings are now installed in the ice and fully enclosed at the center of the almost complete IceCube detector.

In this chapter, we summarize the main steps in the design study of DeepCore. First we discuss shortly the various physics motivations of a low energy extension to IceCube. The parameters and constraints which guided the study are presented next, followed by a summary of the first proposal of DeepCore which served as a baseline for the following intensive design study. We discuss and explain the decisions taken on the DeepCore layout starting from the baseline proposal up to the current 8 string DeepCore design.

5.1 Physics motivations

IceCube has been optimized for the detection of neutrinos at energies of a few TeV and above. Following from that, IceCubes energy detection threshold is at ≈100 GeV. In the energy range of a few hundreds of GeV the number of hit optical modules in IceCube is typically small and the capabilities to reconstruct such events are limited. On the other hand, there are various very interesting physics cases at this lower energies. These cover both astro-physical and particle-physics topics.

- **Weakly interacting massive particles (WIMPs):** Muon neutrinos originating in Neutralino decays in the sun or the Earths core have typically low energies, depending on the original Neutralino mass (see section 2.5.1). By lowering the energy threshold of IceCube, lower Neutralino masses become available for testing.

- **Galactic neutrino sources:** Galactic sources of Gamma-Rays observed by Cerenkov-Air telescopes often show steep spectra and exponential cut-offs at typical gamma-ray energies around 10 TeV. Correspondingly, the (potential) neutrino spectra of such sources would also show this cut-off feature, at neutrino energies typically a factor 2 lower (see section 2.4.3). A lowered energy threshold increases IceCubes sensitivity to these sources. Furthermore, the possibility of using a large part of the detector as a veto against atmospheric muons opens the southern hemisphere for observation with IceCube. Thus the central region of our galaxy including the galactic center become observable, although at a much reduced effective volume, comparable to ANTARES [17]. Most of the observed gamma-ray sources lie in this region.

- **Neutrino oscillations:** Standard vacuum neutrino oscillations are principally not accessible to IceCube. The diameter of the Earth imposes a limit on the oscillation length for atmospheric muon neutrinos and thus also on the energy of oscillating neutrinos. The highest neutrino energy for which a maximum of oscillation probability, on the length scale of the Earths diameter, occurs is at ≈28 GeV (see section 2.6). With a low energy extension this energies may become accessible and neutrino oscillation studies become possible that would be complementary to low-energy neutrino experiments such as SuperKamiokande. Additionally, it may even be possible to measure oscillation parameters such as the mass hierarchy [76].

- **Atmospheric air shower neutrino studies:** Until today no cascades from

atmospheric electron neutrinos with energies above 100 GeV could be detected. With a densely instrumented core within IceCube and the use of the surrounding detector volume as a veto, the reconstruction of such cascades is thought to be significantly improved.

Furthermore the spectrum of atmospheric muon neutrinos in the region below 100 GeV is not well measured. In this region falls the transition from the dominance of neutrinos originating in pion decay to those originating in kaon decay. This yields interesting particle and air-shower physics topics.

- **Gamma ray bursts** In fireball models of gamma-ray bursts (GRBs) a flux of ν_μ and ν_e is predicted from neutron - proton interactions[7]. The expected energies of these neutrinos are at ~ 10 GeV (ν_μ) and ~ 5 GeV (ν_e). In [7] a rate of 7 events per year is expected in a km^3-scale detector. With DeepCore this number might be significantly increased.

5.2 Parameters and constraints

The detection energy threshold of a neutrino telescope depends mainly on

- the optical properties (scattering and absorption) of the detection medium (in this case ice, see section 3.2).

- the geometry of the modules in the instrumented volume. Neutrino interactions at lower energies produce secondary particles of less energy. These radiate less Cerenkov light and travel shorter distances, which yields the need of a denser instrumentation.

- the detection efficiency of the individual modules.

Therefore the major tuning parameters throughout the DeepCore design study are

- DOM positions and DOM-to-DOM spacing

- string-to-string spacing

- number of additional strings and their positions

- use of improved high quantum-efficiency photo-multiplier tubes (HQE PMTs)

The constraints on the DeepCore design are, apart from the costs, both technical and logistical. Technical, because the string hardware and deployment have to rely

on the already existing infrastructures and logistical, because the planned deployment season imposed a tight schedule on the DeepCore design phase.

5.2.1 Time constraints: Deployment and hardware

A deployment of additional strings for the DeepCore extension within the already laid out and financed South Pole deployment seasons was, even though challenging, a well motivated plan, which is now demonstrated to have been the winning strategy. It was the most cost-effective solution, but also guaranteed the longest possible detector lifetime. With DeepCore as an integral part of IceCube it would certainly be decommissioned along with IceCube, so that a later deployment would also shorten the overall DeepCore detector lifetime.

The deployment seasons of IceCube have been shortly discussed in section 3.3.10. At the time of the first DeepCore proposal, 22 standard IceCube strings had been deployed with a seasonal maximum of 13 strings per season. The baseline for the following years was to deploy a minimum of 14 strings per season with a possibility of deploying up to 20. This left the possibility of deploying more than the remaining 58 standard Ice-Cube strings within the 4 planned deployment seasons if no major problem was to significantly delay the drilling and deployment process. Taking into account that the last season had to be shorter due to the decommissioning of the drill equipment, an optimistic upper limit of about 12 extra strings was assumed. Drilling was planned in a way that all holes of one season could be reached from one drill camp position. Any movement of the camp within a season would cost precious time and was clearly disfavored. Thus the deployment of the additional strings was to be done within the upcoming two deployment seasons 2008/09 and 2009/10. With the time needed for hardware acquisition and preparation, as well as the time needed for its shipping to the South Pole, a decision on the layout of the DeepCore strings was bound to be taken in May 2008. A final decision on the exact number of additional strings could be made later, depending on the deployment progress. When this decision was taken and the 6 additional DeepCore strings deployed today were envisaged, a new option became possible. Two strings of the IceCube baseline layout (number 79 and 80) could not be deployed at the planned position and after the success of the first DeepCore design studies and its promising physics cases, it was proposed to use these strings in Deep-Core instead. On the other hand, there were also plans for a high energy extension that involved these strings. A new design study was started and a final decision had to be taken by spring 2009. At this time, after the successful deployment of the first DeepCore string in January 2009, the high energy extension plans were dropped and a

deployment of the two strings in DeepCore was decided.

5.2.2 Technical constraints: String layout

The standard IceCube cables are capable of supporting up to 60 DOMs. This is the case on a standard IceCube string and imposes the limit for the number of DOMs to be deployed to a DeepCore string. More modules per string would require new developments and tests on the support and data cables, not feasible in the available time. A cheaper cable holding a maximum of 40 DOMs was also available.

Technically the DOM-to-DOM spacing on a string has to be at least 2 m due to the size of the DOM support structure. The string-to-string spacing has to be at a minimum of about 10 m for reasons of drilling and surface cable arrangements. The already installed surface cables also give some constraints on the exact positions of additional strings.

5.3　1st step: Initial proposal

The need for a low energy extension was especially strong among the working groups focusing on the detection of dark matter WIMP induced neutrinos. The module spacing of IceCube would only deliver a relatively small number of hits for muons induced by neutrinos of a few 100 GeV, which is typically not sufficient for muon track reconstruction. Furthermore the trigger threshold of IceCube would not permit detection of neutrinos with energies below 100 GeV, which are generally interesting to test the yet unexplored neutralino mass regions (see section 2.5.1). A step to mitigate this problem was the full integration of AMANDA into the IceCube data taking. With its much denser spacing, AMANDA formed a compact core that was fully enclosed by the surrounding IceCube detector. This imposed another advantage, as the instrumented IceCube volume around AMANDA could be used as a veto against the background of atmospheric muons. But not only the WIMP searches benefited from the integration of AMANDA, also dedicated low energy point source searches, as performed at the Heidelberg IceCube group, showed the power of a compact core.
However, several problems were connected with a prolonged maintenance of AMANDA. The AMANDA optical modules are of a different kind, with analogue signal output and much higher intrinsic noise rates, and the AMANDA data acquisition system (DAQ) imposed continuous problems, including difficulties in the synchronization of the two

DAQ systems[1]. The maintenance became even more difficult and expensive, when also the snow accumulation around the building which housed the AMANDA DAQ (the Martin A. Pomerantz (MAPO) building) required it to be raised in order to safely continue operation. Finally, the position of AMANDA in the top and on the border of IceCube was not ideal for the veto of atmospheric muons, as to one side only one layer of IceCube strings was available for the veto.

Given the above reasons, a more cost-effective and scientifically attractive solution was to build a new instrument at the bottom center of IceCube. Even more so, as the ice in the bottom of the detector is the clearest ice available with absorption lengths almost twice as long as in the top.

Consequently, the idea of DeepCore was presented to the IceCube collaboration by the Swedish collaboration member institutes at the Universities of Stockholm and Uppsala for the first time in spring 2007. At this time IceCube had 22 strings installed and AMANDA was fully integrated into the IceCube data taking. The idea found a wide resonance within the collaboration and soon many other institutions from Germany, Belgium and the U.S. got involved. The IceCube collaboration board and project office gave their agreement to prepare for a deployment of up to 9 additional strings.

Since additional strings were not covered by the original IceCube budget, additional funds were needed. The Swedish collaboration groups therefore handed in an application to the Swedish Wallenberg foundation.

This application proposed 6 additional strings located around a central IceCube string (string 36) at distances of ≈72 m also to the surrounding 6 standard IceCube strings. Each string was planned to hold 40 standard IceCube DOMs in a 10 m spacing at depths from -500 m to -110 m, w. r. t the center of the detector.

In agreement with the main science goals followed by the Swedish IceCube groups, the application was mainly focused on the improvement to be achieved in the search for solar WIMP dark matter. Effective volume improvements for two different neutralino annihilation channels given in the proposal [82] are shown in fig. 5.2. A clear improvement can be seen for energies of a few 100 GeV and below. Below 100 GeV DeepCore can improve the effective volume for WIMP searches by an order of magnitude. Atmospheric neutrino effective areas were also calculated and found to have comparable improvements.

At the end of November 2007 the application was accepted by the Wallenberg foundation and funds for the proposed 6 strings were granted.

---

[1]The author has contributed to the efforts for a smooth combined data taking by successfully installing new soft- and hardware to the AMANDA DAQ at the South Pole in November 2007.
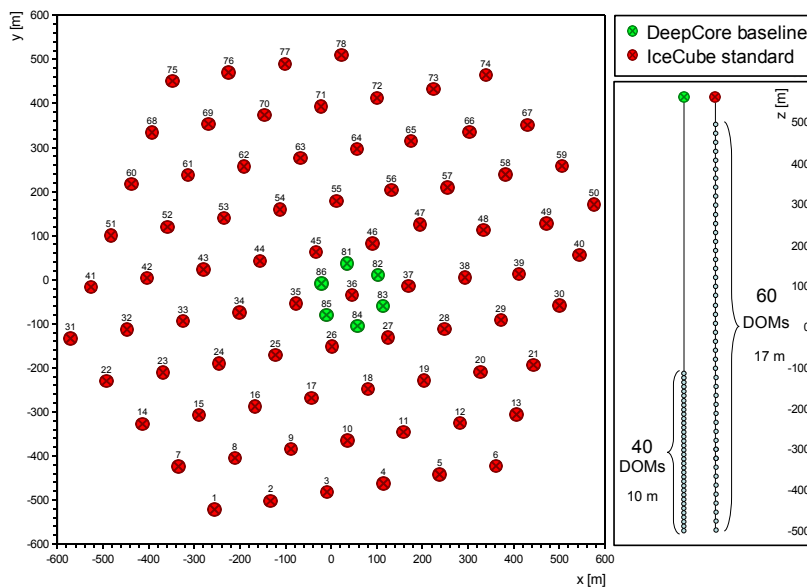
Figure 5.1: Initially proposed DeepCore geometry - x- and y-positions of the standard IceCube strings (red) and the additional six DeepCore strings (green) as proposed in the fund application to the Swedish Wallenberg foundation. The z-positions of the DOMs are shown schematically on the right.

5.4 2nd step: German and Belgian proposals for additional strings

The intriguing abilities shown by the first DeepCore simulations and the unique situation given by the on-going IceCube deployment which potentially left room for additional strings triggered discussions on how DeepCore could be further improved from the given baseline layout. A larger number of DeepCore modules in the ice, either on the already proposed or on newly added strings, were sure to enlarge the effective volume of DeepCore. Thus the physics capabilities and discovery potential of Deep-Core could be increased substantially in all projected physics channels. This was the main motivation for a group of German IceCube member institutions[1] to make a joint application for additional funds to the German Bundesministerium für Bildung und

---

[1]These were: Rheinisch-Westfälische Technische Hochschule Aachen, Humboldt Universität zu Berlin, Technische Universität Dortmund, Max-Planck Institut für Kernphysik in Heidelberg, Johannes-Gutenberg-Universität Mainz und Bergische Universität Wuppertal
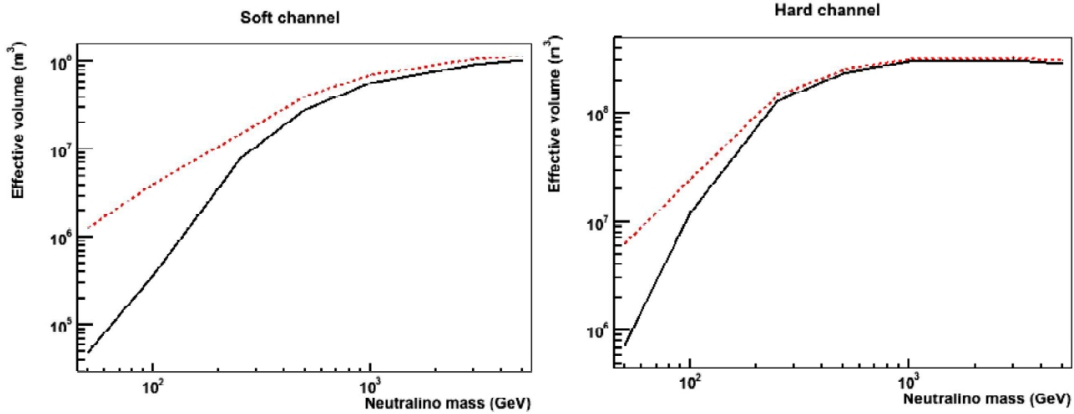
Figure 5.2: Initial DeepCore proposal - Effective volume vs. neutralino mass for muons induced by neutrinos origining in neutralino annihilations. The simulated time corresponds to the six months of the year where the Sun is below the horizon. The dashed line corresponds to full IceCube augmented by the six Deep Core strings. The full-drawn line corresponds to full IceCube without DeepCore. Soft and hard channel correspond to neutralino decays into bb or WW, respectively, which result in different spectral shapes of neutrino spectra. From [82].

Forschung (BMBF). This application asked for additional 4 strings in the standard configuration with 40 DOMs.

At the same time the Belgian collaboration member institutes applied for funds to buy the hardware of 2 more strings, so that a maximum of 12 strings would become possible. In spring 2008 the BMBF granted funds worth 2 strings which could be used for any enhancement to DeepCore as would seem feasible. A few months later the Belgian groups were granted funds worth one additional string.

These additional funds opened the possibility for a more thorough design study with an extended DeepCore detector geometry.

5.5 Main design studies

The initial DeepCore proposal already included a baseline layout which had been developed following the basic demands on the position of the dense array in the bottom center of IceCube, within the clearest ice. The number of 6 additional strings was a natural choice given the hexagonal geometry of the surrounding strings in IceCube. The positions of these strings were chosen to be around a central IceCube string at the centers of the 6 triangles formed by this central string and its 6 nearest neighbors. The

decision to lay out each DeepCore string with 40 standard DOMs is connected to the intended DOM-to-DOM spacing of 10 m. 40 modules thus give an instrumentation of the string from the detector bottom just up to the strongest dust layer. At that point a more sophisticated design study was postponed to get initial simulation results in time for the funding applications.

With the funds granted to build this baseline geometry and expectations on additional funds a more extensive design study was started to optimize DeepCore. This optimization of the detector performance was relying mainly on simulation results on a lower analysis level. The final optimization thus was based on the available tools which allowed us to determine signal efficiencies and effective volumes at trigger level in a conservative way, as well as atmospheric muon veto capability studies.

An "optimal" detector layout will always refer to a special physics channel. For instance, an optimization for neutrino oscillations calls for a denser instrumentation to lower the energy threshold, whereas galactic point source searches might benefit more from an increased geometrical volume. So, to test different possible layouts of DeepCore for their possible benefits to the different physics channels, a number of full detector simulations were produced. These included atmospheric background muons (CORSIKA, see section 3.4.1) and signal neutrinos. Within all of the tested layouts the string positions of the six baseline strings were the only constant. Apart from this all basic parameters have been under investigation:

- the number of additional strings on top of the baseline 6 and their positions

- the number of modules per string

- the positions and spacing between the modules on a string

- the optional use of standard or HQE photomultiplier tubes in the DeepCore DOMs

The last point came up with the development of new photo-multiplier tubes with an increased quantum efficiency by the producer Hamamatsu. This new PMT (Hamamatsu R7081MOD) promised a 40% increased quantum efficiency which would lead to a significant improvement to the effective volume at low energies, although at the expense of a $\approx 33\%$ higher noise rate. Since these new PMTs were to be similar in built to the standard IceCube PMTs, except for the cathode material, there would be no additional development necessary on the layout of the DOMs. The costs of the

new PMTs were at that time substantially higher than for the standard PMTs, which imposed a limit on the number of additional strings depending on the granted funds. At the beginning of 2008 the IceCubes group at the Chiba university in Japan and at the University of Wisconsin in Madison had tested a number of the new PMTs and verified the improved performance. When installed into the standard IceCube DOM, the optical sensitivity of the complete structure was found to be raised by $\sim$30%.

5.5.1 DeepCore geometries

Following the constraints given above up to 12 DeepCore strings and up to 60 DOMs per string were analyzed with different string and DOM positions. Based on the anticipated fundings, layouts with a larger number of strings were simulated to have less modules per string and vice versa. We give here an overview over those simulated geometries which had a major influence on the design decisions.

5.5.1.1 String numbers and positions

In the course of this design study mainly 4 string position layouts have been tested. An early layout, a 12 string geometry simulated with 40 standard DOMs per string, was used intensively in the development and testing of the first sufficient atmospheric muon veto (see previous chapter). But since the funding and deployment of 12 additional strings was the most optimistic scenario, the focus was put on what seemed more realistic scenarios at that time (early 2008). The four intensively studied geometries are depicted in fig. 5.3. Along with the baseline 6 string geometry (A, fig. 5.3, top left panel) two configurations were simulated which extended the densely instrumented volume with additional strings at the same string spacing and DOM positions as in the baseline configuration. One of these added 4 more strings to the baseline, located around a nearest neighbor IceCube string (number 35, see Fig. 5.3, top right panel). The other had 9 DeepCore strings, where the additional 3 were located all in the same distance to the baseline central string (number 36, see Fig. 5.3, bottom left panel). Both of these geometries, named string geometry B and C, respectively, aim to improve the effective volume in the same energy range as the baseline geometry. Geometry C has been simulated to test a more symmetric layout, w.r.t. geometry option B. Finally a configuration of 9 DeepCore strings of which 3 strings were positioned in an even denser string-to-string spacing of $\approx$42m within the baseline layout. This layout aimed to improve the effective volume especially at the lowest neutrino energies, below a few tens of GeV (string geometry D, see Fig. 5.3, bottom right panel).
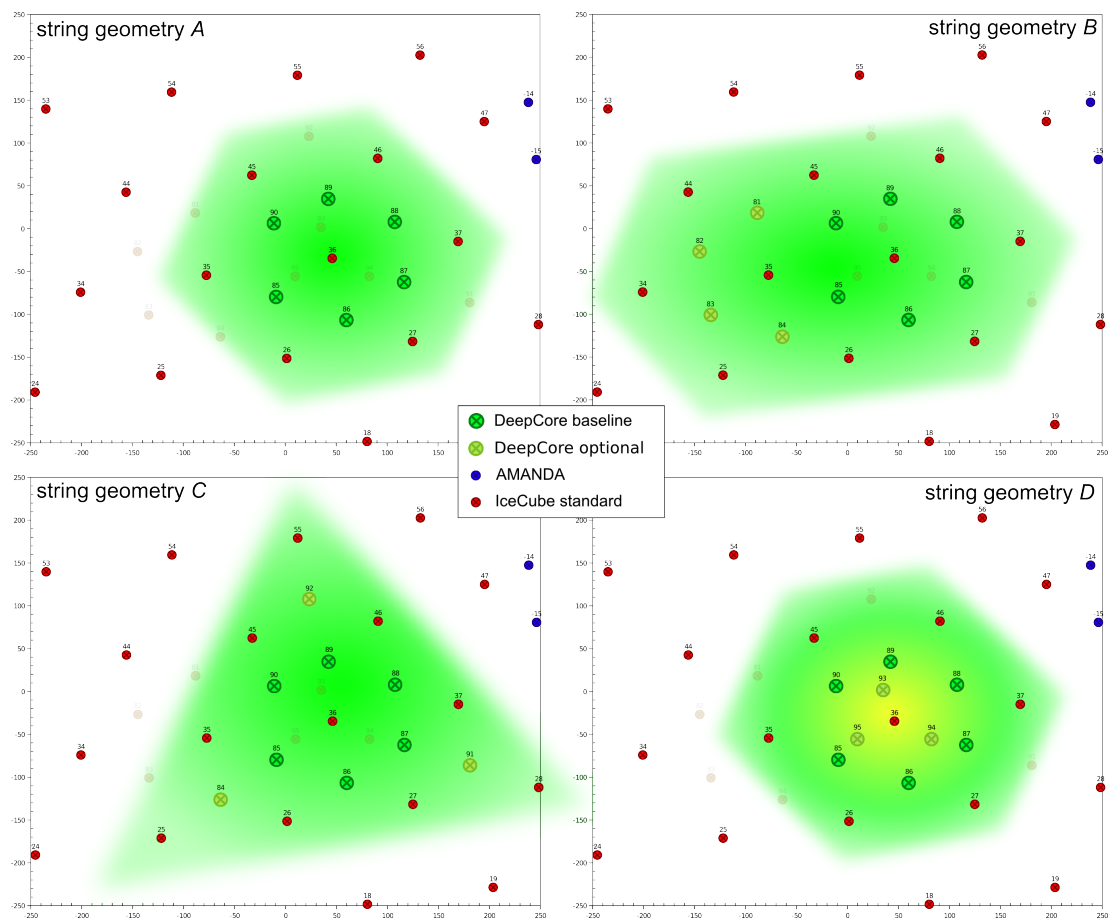
Figure 5.3: Possible string layouts with additional DeepCore strings - Four different subsets of an overall number of 15 simulated DeepCore strings (81-95) are shown. Upper left: Baseline 6 string geometry (*A*); Upper right: Four additional strings around string 35 (*B*); Lower Left: 3 additional strings surrounding the baseline configuration (*C*); Lower right: 3 additional strings at closer string spacing within the baseline volume (*D*).

5.5.1.2 DOM positions and spacings

Apart from the string positions also the number of DOMs per string and their positions were varied. The main points under discussion were the DOM-to-DOM spacing, as a key to the final energy threshold, and a placement of a fraction of DOMs in the upper half of the detector, which might potentially improve the veto capabilities. In fig. 5.4 the primarily studied DOM positions are shown. Note that these different layouts were mainly simulated with the baseline 6 string layout (*A*). In the following we will refer to the various layouts by giving the letter associated with the string and the number

corresponding to the DOM positions, e.g. *A0* for the DeepCore baseline layout.
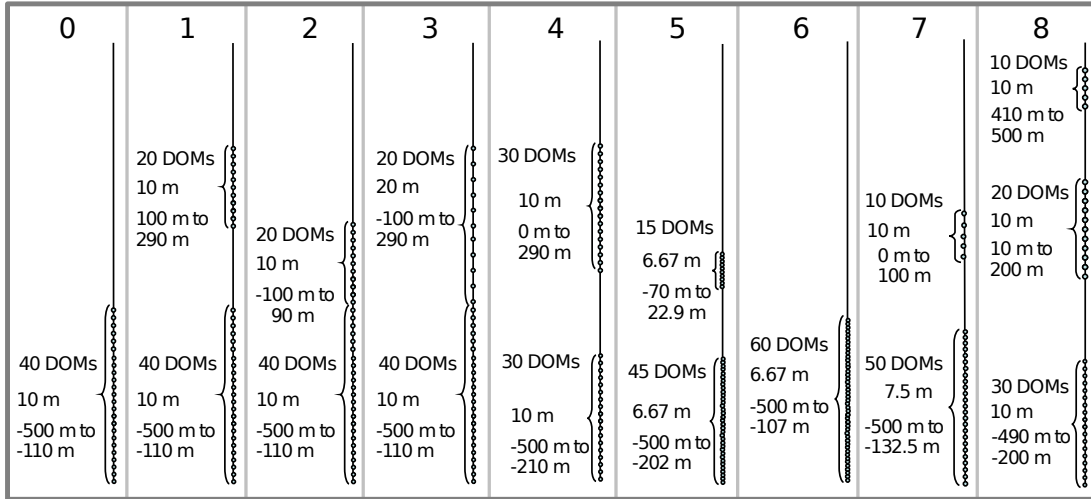

Figure 5.4: Possible DOM positions on DeepCore strings - *0:* Baseline string layout. *1 - 3:* Baseline layout with additional 20 DOMs in different positions used for initial veto studies. *4 - 6:* Different DOM positions and DOM-to-DOM spacings used in initial trigger level studies. *7 - 8:* Hybrid geometries combining benefits found from configurations *1 - 6.*

5.5.2 Additional strings vs. additional DOMs per string

The layout of the DeepCore strings was the first main decision that had to be taken on the final DeepCore design. It was however strongly connected to the number of additional strings. With limited funds more strings would supposedly not allow for installation of more than the baseline 40 DOMs per DeepCore string and vice versa. While the final decision on this point was to be made upon the simulation results, a first decision was nevertheless taken before that. The cable of the first DeepCore string had to be bought in the beginning of 2008, a couple of months before the final decision date. To leave all options of string design open, it was decided to purchase a standard IceCube string cable, capable of holding up to 60 DOMs. Anyhow, this decision strengthened the arguments for a 60 DOM per string design.

The first point to be addressed by the simulations was a comparison between extended geometries with more then six DeepCore strings and a six string geometry with 60 instead of 40 DOMs per string. This was done by comparing signal efficiencies after

triggering. In parallel to that, the effect of replacing the standard PMTs on the Deep-Core strings by HQE PMTs was estimated and compared to the improvement gained by alternative geometries. In the final step, the optimal position of the DOMs on a string was studied. Additional DOMs in the upper part of the detector have the potential to increase the veto capabilities against the less effectively vetoed class of vertical downwards-going atmospheric muons. So, a full veto study has been performed here along with the trigger level efficiency study.

The three considered geometries holding more than 6 DeepCore strings were simulated with the baseline DOM positions on all strings (*B0*, *C0*, *D0*). The (atmospheric muon neutrino) signal efficiencies of these layouts at trigger level are given in fig. 5.5 relative to the nominal baseline layout of 6 strings with 40 DOMs (*A0*). The results are compared to a 6 string geometry with 60 standard DOMs (*A4*). In this geometry 30 modules are positioned above and 30 modules below the main dust-layer. Signal efficiencies are defined as the number of triggered events divided by all events that have been simulated. A triggered event requires 4 hits in hard local coincidence within the DeepCore fiducial volume.
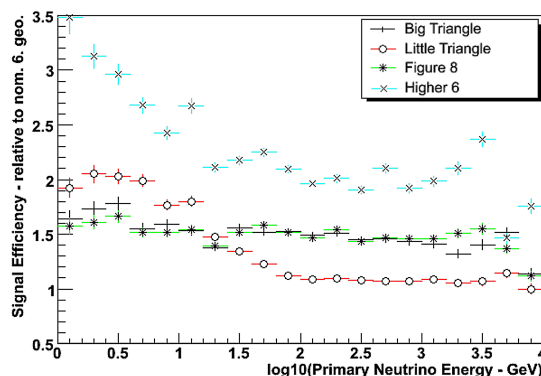
Figure 5.5: Signal efficiency of extended geometries relative to baseline geometry I - Figure 8 (B0), big triangle (C0), small triangle(D0): 40 DOMs at 10 m spacing. Higher 6 (A4): Baseline 6 strings with DOM layout 4 (see fig. 5.4). From [57].

Fig. 5.5 shows clearly that the 6 string/60 DOM geometry performs at least 30% better at all studied energies than the geometries adding more strings. The two geometries with the standard spacing perform more or less equally well, which is remarkable since configuration *C0* has one string less then *B0*. They give an almost constant improvement of ≈50%, which roughly corresponds to the increase in densely instrumented volume. As expected, configuration *D0* with its denser string spacing gives best results at the lowest energies, but adds no efficiency whatsoever above 100 GeV.

99

The performance of the 60 DOM per string configuration *A4* is remarkable, since the overall densely instrumented volume in this case is comparable to that in the *B0/C0* scenarios, but with a large part located in the dustier ice. The reason for this is the effective splitting in two separate densely instrumented volumes which increases the effective volume of the detector. This makes this configuration the best option for upwards-going events which need no muon veto, but for downwards-going events, where a vertex inside the fiducial volume is required, the improvement will be considerably smaller. The additional DOMs in the upper part of the detector would, in that case, improve the veto so that the fiducial volume could be enlarged, but the volume won by this would not be densely instrumented.
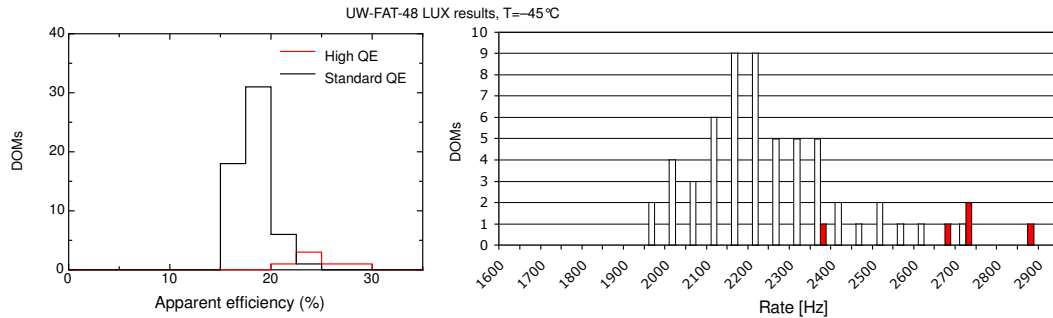
5.5.3 HQE PMTs

Figure 5.6: Final acceptance test (FAT) results of standard and 5 HQE DOMs - Left: Optical efficiency at 405 nm; Right: Noise rate. White column: standard DOM, red column: HQE DOM. Measurements made at the University of Wisconsin, Madison [92].

The laboratory performance of the Hamamatsu R7081MOD PMT has been discussed already in section 3.3.5. At the time of this design study the full statistics shown in Fig. 3.9 were not available and only a handful PMTs had been tested with 4 DOMs. The results can be seen in Fig. 5.6. They are in good agreement with the later measurements, giving a 40% increased optical efficiency and 35% higher noise rate.

To estimate the effect of the increased performance of these devices in different Deep-Core configurations, simulations have been done with the enhanced PMTs on all Deep-Core strings. These simulations invoke the same geometries as have been discussed in section 5.5.2.

The upper left plot in fig. 5.7 is similar to fig. 5.5, except for the use of the HQE PMTs. It thus includes the improvements both given by the extended geometry and
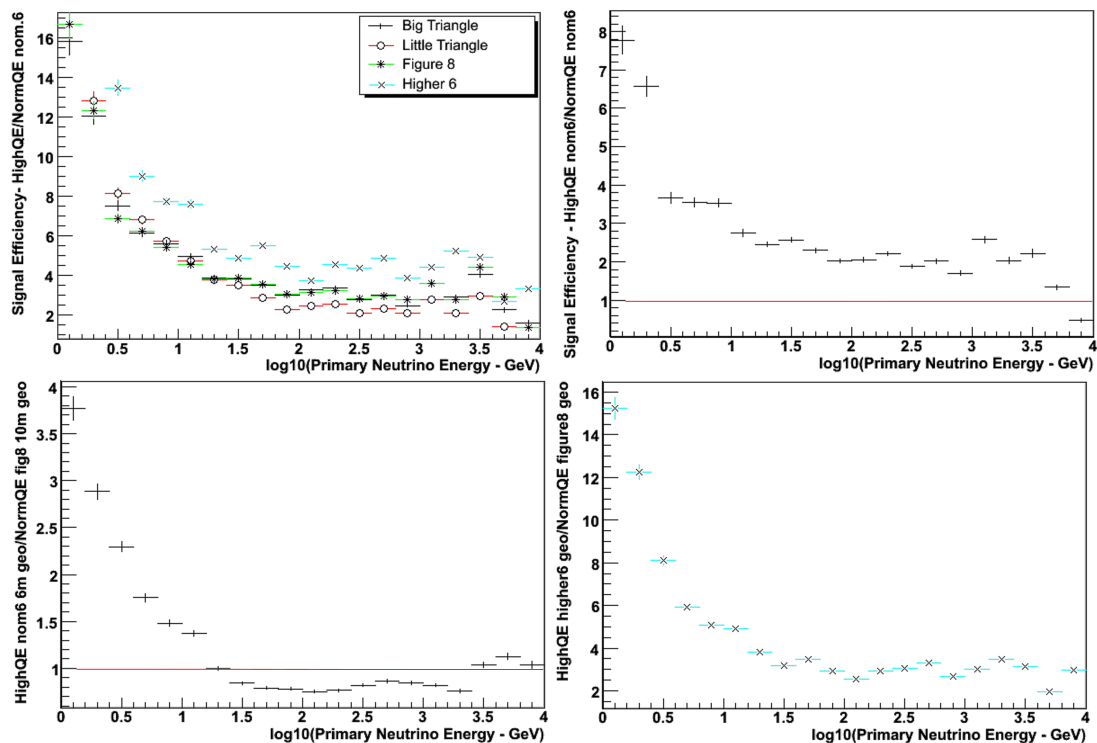
Figure 5.7: Signal efficiency improvement by use of HQE PMTs - Upper left: Improvement factor of extended geometries using HQE PMTs w.r.t. baseline layout. Upper right: Improvement factor of HQE PMTs over standard PMTs for the baseline layout. Lower left: Improvement factor of HQE PMTs in a 6 string/60 DOMs/6 m spacing over standard PMTs in "figure 8 - B0" geometry. Lower right: Improvement factor of HQE PMTs in the "higher 6 - A4" layout over standard PMTs in "figure 8 - B0" geometry. From [57].

the enhanced PMTs. A comparison to the given fig. 5.5 shows strongly enhanced signal efficiencies at all energies. Especially at the lowest energies below 10 GeV. This can also be seen in the upper right plot of fig. 5.7. Here the gain in signal efficiency is given for the baseline geometry of 6 strings and 40 DOMs using HQE PMTs relative to the use of standard PMTs. The effect of the enhanced PMTs is clearly largest at the lowest energies, but there is a significant gain over the whole energy range up to 10 TeV. In the most relevant spectral region for DeepCore, below a few hundred GeV, the gain is at least 100%.

The two lower plots in fig. 5.7 show signal efficiency improvements of geometries with 6 strings and 60 HQE DOMs with respect to configuration *B0* and standard DOMs. On the lower left, it is given for a layout with all 60 DOMs below the dust-layer in a

6.67 m spacing (configuration *A6*) and on the right for configuration *A4* which had shown the most promising performance with standard DOMs. It is apparent, that at the very lowest energies, below 10 GeV the HQE PMTs give the best improvement of all options. However, at these energies the abilities to sufficiently reconstruct an event are very uncertain. The better performance of configuration *A4*, seen in the lower right plot is partially due to the effect described in section 5.5.2, i.e. it is mainly the upwards-going events that profit, while the fiducial volume for downwards-going events can only be enlarged through a better veto performance.

The shown improvements by the use of HQE PMTs, and the fact that at trigger level these PMTs give signal efficiencies comparable or better than the extended geometries employing additional strings, impose a strong argument for their use. Furthermore, this improvement can be achieved without the additional costs and uncertainties involved with deploying additional strings.

Following this argumentation a decision for the deployment of the tested HQE PMTs was made in early spring 2008.

5.5.4 DOM positions

With the decision for the use of HQE PMTs the number of additional strings that could be financed was already limited. Also the above given studies showed clear advantages of deploying additional modules on the DeepCore strings in the upper half of the detector, even though this was not shown for down-wards going events. To estimate the use of 60 DOMs per string geometries and the optimal positions of these DOMs, we tested the signal efficiencies and veto capabilities of various possible layouts.

5.5.4.1 Initial veto studies with dedicated veto DOMs

A comparison of the veto performance, with 3 different string layouts and the baseline 6 strings, is shown in fig. 5.8. The extended geometries are based on the baseline layout and add 20 additional DOMs at different positions on the string. Either above the dust layer in a 10 m spacing ("1-20", *A1*), or directly above the fiducial volume within the dust layer ("21-40", *A2*) or in a 20 m spacing from directly above the fiducial volume upwards ("Odd/Even", *A3*).

The initial veto studies with a 40 DOM per string geometry (see section 4.3) had shown that one of the background event classes that manage to penetrate deep into the veto layer were vertically down-going muon tracks (recall Fig. 4.8 and Fig. 4.9).
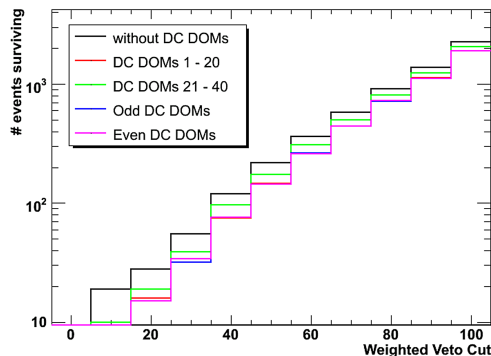
Figure 5.8: Veto study of additional DOMs per string - Number of events surviving the geometrically penalized veto with a cut value of 60. Black line corresponds to a veto without DeepCore DOMs in the upper part of the detector. The red and green curves refer to string layouts 3 and 4 in fig. 5.4, respectively. The blue and magenta curves represent layout 5 and a similar layout with DOM positions shifted by 10 m. From [44].

This introduced the idea to enhance the veto performance for this class of events, by deploying a number of DOMs, dedicated to the veto, above the dust-layer.

Fig. 5.8 shows the abundance of atmospheric muon background events with a given cumulative veto value, as produced by the geometrically penalized veto in its version A (see section 4.2.1). One can see that any of the extended geometries improves the veto capabilities, although it is evident that the improvement is largest if the additional DOMs are placed above the dust-layer. The fact that the layouts with a 20 m DOM spacing (and half of the DOMs within the dust-layer) performs as well as the layout with all 20 DOMs in the clear ice hints that the given improvement might be achieved also with less DOMs above the dust-layer.

A higher number of modules on a string might also be used to increase the module density in the region of the clear ice. A smaller DOM-to-DOM spacing will eventually lead to a lower energy threshold. This is actually the case, as illustrated in fig. 5.9. The left plot of this figure shows the energy spectra of atmospheric muon neutrino events surviving the geometrically penalized veto in version A (cut events with $W_{tot} > 60$). The spectra are given for a DOM layout with a dense DOM-to-DOM spacing of 6.67 m where all modules are located in the clear ice below the dust layer (*A6*, red curve) as well as for configuration *A1*. In the latter configuration, only the 40 modules in the deepest ice contribute to the fiducial volume. The improvement by the denser layout

seen here is quantified by the plot shown in the right panel of fig. 5.9. It gives the ratio of the two spectra and thus the gain in signal efficiency at this analysis level. A clear improvement is achieved at energies below 100 GeV, which is the energy region DeepCore is aiming to improve most. Note that the peak in gain at a few TeV is due to low statistics.
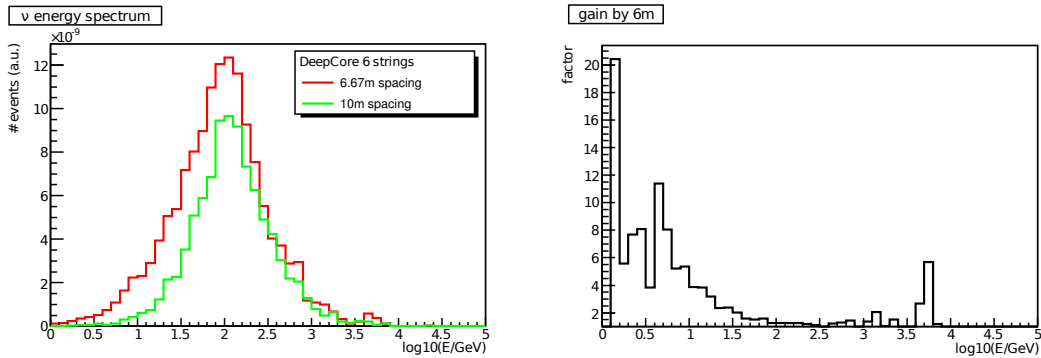

Figure 5.9: Lowered energy threshold by denser DOM spacing - Left: Down-going atmospheric neutrino energy spectra after L1 veto (geometrically penalized veto, version A) with configuration *A1* (green) and *A6* (red). Right: The ratio of the two spectra on the left giving the gain by using the denser geometry *A6*. From [44].

Following the results given so far a decision for the deployment of 60 modules per string was made. The increased performance for upwards-going tracks with configuration *A4*, the lowered energy threshold by a denser DOM-to-DOM spacing and the increased veto capabilities against vertically downwards-going muon background events imposed convincing arguments. This decision, in conjunction with the drilling efforts, also ensured the most cost-effective way to improve on the original DeepCore design.

5.5.4.2   Final veto studies with dedicated veto DOMs

A final decision on the DOM-to-DOM spacing was a decision based on the physics cases of DeepCore. Essentially three layout options were considered for final decision. These layouts sought to combine the benefits found in the previous signal efficiency and veto studies. The first geometry, motivated by the veto studies and the effect of a denser DOM spacing, had 50 DOMs at a 7.5 m spacing in the bottom of the detector and 10 DOMs in a 10 m spacing above the dust layer to improve the veto capabilities (*A7*). The second geometry was the already studied configuration *A4* with 30 modules above and 30 modules below the dust-layer. It was mainly motivated by the

	Configuration *A7*						Configuration *A4*					
	Veto 0			Veto 1			Veto 0			Veto 1		
	R [m]	z [m]	llh	R [m]	z [m]	llh	R [m]	z [m]	llh	R [m]	z [m]	llh
cut parameter values	260	-100	-6	265	-100	-6	310	-200	-6	185	-200	-4
resulting volume ($10^6 m^3$)	84.95			88.25			90.57			32.26		
Atm. Muon background at veto L1	3710			26472			2717			85796		
Atm. Muon background at veto L2	1			1			1			1		
Atm. Muon neutrino signal at veto L1	562			769			354			714		
Atm. Muon neutrino signal at veto L2	142			145			90			70		

	Configuration *A8*					
	Veto 0			Veto 1		
	R [m]	z [m]	llh	R [m]	z [m]	llh
cut parameter values	265	-115	-6.5	220	-170	-5.5
resulting volume ($10^6 m^3$)	84.94			50.18		
Atm. Muon background at veto L1	2789			60186		
Atm. Muon background at veto L2	1			1		
Atm. Muon neutrino signal at veto L1	391			749		
Atm. Muon neutrino signal at veto L2	91			75		

Table 5.1: Signal and background event numbers for configurations A4,A7 and A8 - L1: Geometrically penalized veto version B (cut $W_{tot} > 60$); L2: Vertex cut (parameters in table)

increased signal efficiency for upwards-going events and the first experiences in using the combined AMANDA and IceCube-22 detectors. The third option, configuration *A8*, had 30 DOMs in a 10 m spacing below the dust layer as in the 2nd option, but the 30 DOMs above were split into two parts. One part consisting of 10 DOMs being located directly at the top of the detector and aiming to improve the veto capabilities. The other directly above the dust-layer and holding the remaining 20 DOMs, thought to improve the effective volume. This last geometry was also created to have a final test on the thickness of the top veto layer necessary to distinguish downwards-going neutrino events from background.

Consequently, the geometrically penalized veto (L1, in version B and a cut of all events with $W_{tot} > 60$) has been applied to this simulations with two different definitions of the veto volume.

- **Veto 0:** A conservative approach with the complete top of the detector used as veto (i.e. all DOMs higher then -100 m, w.r.t. the detector center)

- **Veto 1:** The fiducial volume is extended to the upper part of the detector. Depending on the geometry, the thickness of the top layer veto varies. The exact configurations can be taken from fig. 5.10

The quantitative result of muon background and downwards-going atmospheric muon neutrino signal simulations (Bartol model [9]) is given in table 5.1. The events were
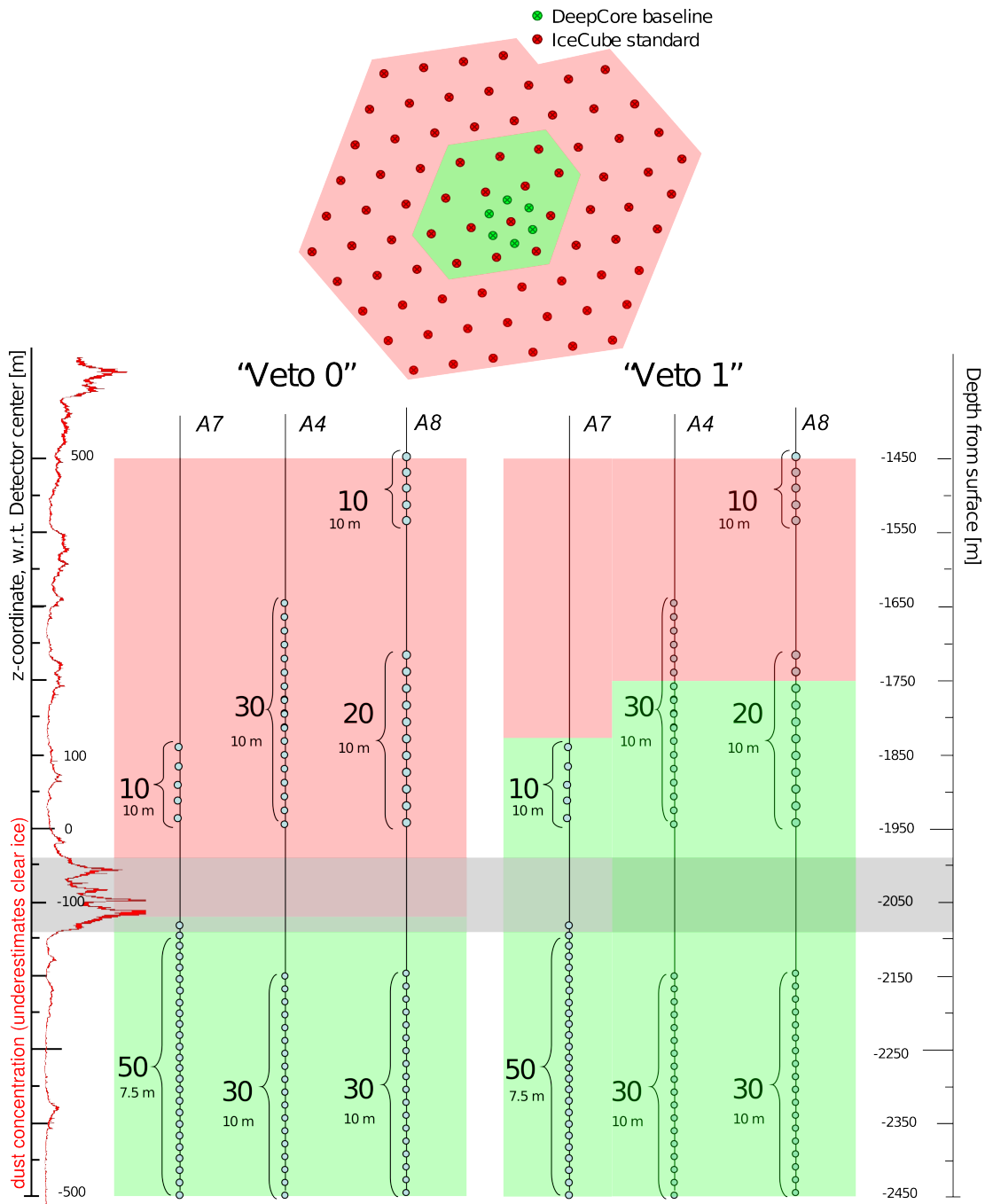
Figure 5.10: Veto volume definitions for final DOM spacing studies - Top: String assignment to the veto region. Strings in the fiducial (green) region have two different veto definitions shown below. Veto 0: All DOMs above detector coordinate z=-110 m belong to veto layer (left); Veto 1: In DOM configuration *A7* the fiducial volume incorporates all pure DeepCore string DOMs, all standard string DOMs above z= 120 m belong to the veto. In DOM configurations *A4* and *A8* only DOMs in the upper 250 m of the detector contribute to the veto.

triggered with an SMT 6 trigger and a R-T hit cleaning (see section 4.1.1) has been applied along with a time-window cleaning of 5 μs (see section 4.1.3).

The signal event numbers with veto 0 are largest with configuration $A7$, which is due to the dense DOM spacing that leads to more triggers at lower energies, as can be clearly seen from Fig. 5.14, left panel. With veto 1, significantly more signal events are kept especially with geometries $A4$ and $A8$, and the increase of the fiducial volume in these configurations matches the advantage of configuration $A7$, except at the very lowest energies below 10 GeV. The signal event vertices, after the L1 veto, are typically distributed in, and closely around DeepCore, as shown exemplary in Fig. 5.11 for the $A7$ geometry with veto 0.

Table 5.1 gives that the background rejection with the L1 veto 0 is more effective with configurations $A4$ and $A8$, as there are more additional DOMs aiding the veto in the top part of the detector. Fig. 5.12 and 5.13 show the reconstructed vertex position for configurations $A7$ and $A8$, respectively (Configuration $A4$ gives similar results as $A8$). Using 30 DOMs per string ($A8$) in the upper detector part for the veto removes vertical muon events almost completely. But, with just 10 DOMs ($A7$) also a good improvement is achieved in removing the "top of the sombrero hat" (compare: section 4.3, fig. 4.8). However, after the cuts on z, r and $LLHR$ of the reconstructed vertex (L2), the improvement of the veto for $A7$ and $A8$ is mostly lost, as the vertex cuts result in almost similar fiducial volumes.

The red spot in the upper part of fig. 5.12 and 5.13 is due to the absence of the undeployed strings 79 and 80 (see section 3.3.1) which result in a weaker veto in that direction. In later analyses the veto volume will be adjusted accordingly.

When looking at the numbers of muon background events surviving L1 in veto 1, it is evident that this is much less efficient in background rejection then veto 0. This is no surprise and an effect of the much thinner top veto-layer. In configuration $A7$, where the veto layer in veto 1 is ~ 100 m thicker than for the other configurations, the background rejection is found to be more effective. The reconstructed vertex positions for veto 1 and configurations $A7$ and $A8$ are shown in fig. 5.15 and 5.16, respectively. The string locations of IceCube are nicely mapped, as tracks passing close to a string are more effectively removed.

After application of the L2 cuts, the worse performance of L1 in background rejection is compensated, but at the cost of signal efficiency. When L2 is optimized in a way that the background is reduced to one event, the upper part of the detector is excluded from the final fiducial volume in all cases. In the case of configurations $A4$ and $A8$ the resulting volume is even significantly smaller than for veto 0, and hence also the signal
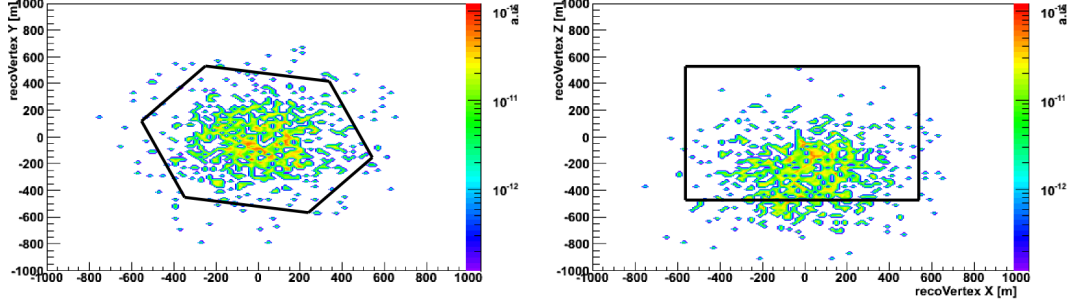
Figure 5.11: Reconstructed vertex of atmospheric neutrino signal in Configuration _A7_ with veto 0 - Left: Top view (x vs. y position of the vertex); Right: Side view (x vs. z). From [43].
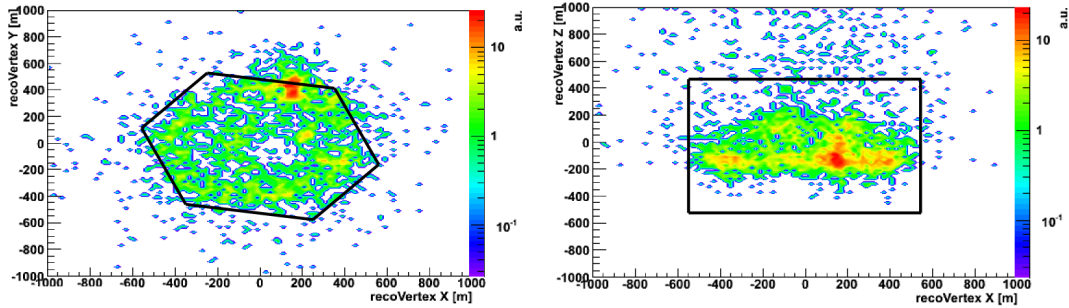

Figure 5.12: Reconstructed vertex of atmospheric muon background in Configuration _A7_ with veto 0 - Left: Top view (x vs. y position of the vertex); Right: Side view (x vs. z). From [43].

efficiency is worse. In configuration _A7_ with veto 1 the fiducial volume and signal efficiency are comparable to veto 0.

In summary it can be said that

- the veto studies favor configuration _A7_. The final fiducial volume created by the vertex cuts is not improved much by DOMs in the upper half of the detector. A denser spacing yields a higher signal efficiency, especially at low energies.

- the L1 veto algorithm has to make use of the complete upper half of the detector, as the L2 cuts remove too much signal when compensating for additional leaking background.
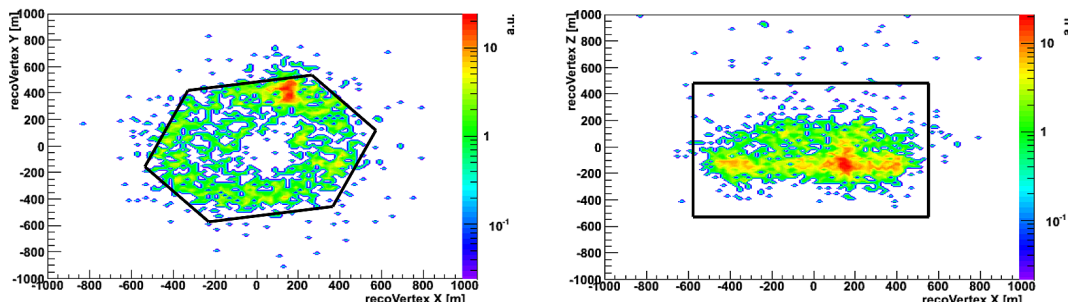
Figure 5.13: Reconstructed vertex of atmospheric muon background in Configuration _A8_ with veto 0 - Left: Top view (x vs. y position of the vertex); Right: Side view (x vs. z). From [43].
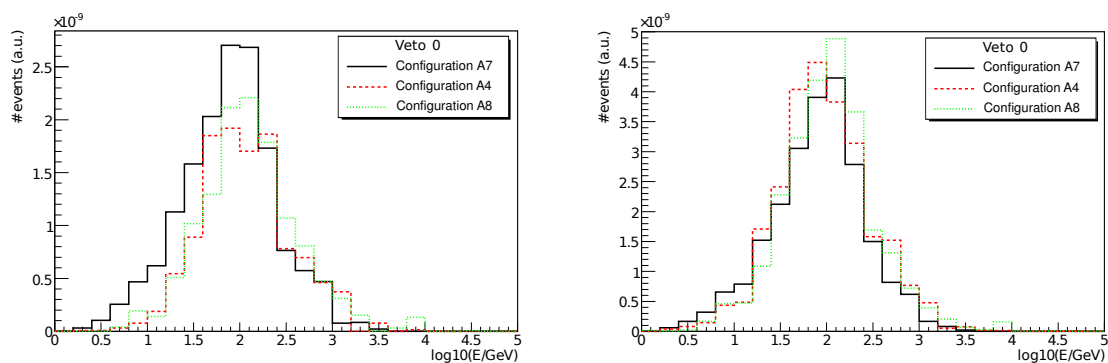
Figure 5.14: Energy spectra of atmospheric neutrino signal events surviving the L1 veto - Configurations _A7_ (black), _A4_ (red) and _A8_ (green); Left: Veto 0; Right: Veto 1. From [43].

5.5.4.3 Angular reconstructions

As a first, very conservative estimate of the reconstructability at the low energies DeepCore is aiming for, IceCube standard track reconstructions have been applied to muon neutrinos surviving the L1 veto 0 in configurations _A7_, _A4_ and _A8_. The angular reconstruction accuracy of a likelihood fit with 16 re-iterations is shown in fig. 5.17. The mis-reconstruction angle, defined as the angular distance between the true MC neutrino direction and the reconstructed one, is shown for muon neutrinos of energies greater then 30 GeV (left) and less then 30 GeV (right). While at the higher energies there is a clear indication of reconstructability (without any further quality cuts, a median of $\sim 30°$ is reached), there is no correlation between true and reconstructed direction

Figure 5.15: Reconstructed vertex of atmospheric muon background in Configuration _A7_ with veto 1 - Left: Top view (x vs. y position of the vertex); Right: Side view (x vs. z). From [43].

———
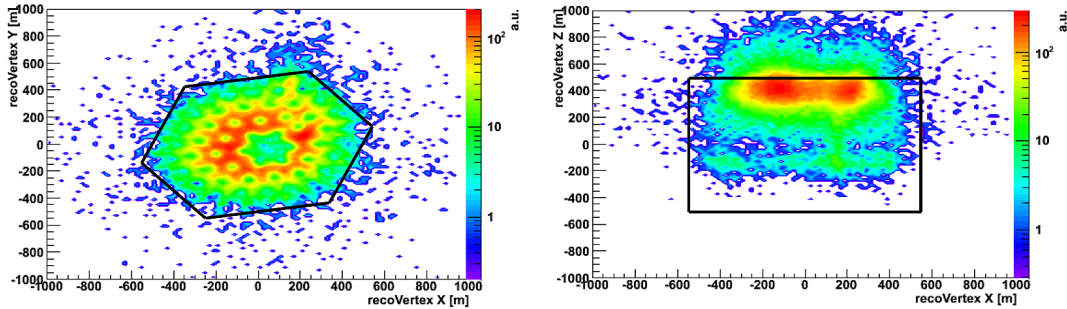
Figure 5.16: Reconstructed vertex of atmospheric muon background in Configuration _A8_ with veto 1 - Left: Top view (x vs. y position of the vertex); Right: Side view (x vs. z). From [43].
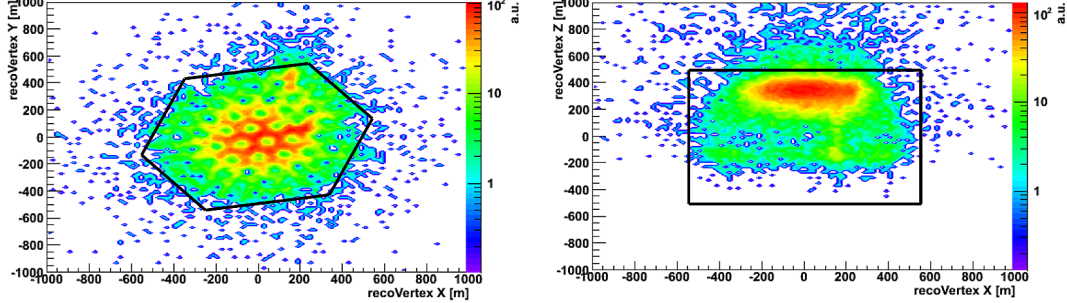
at the lowest energies. Note, that this is not completely unexpected. IceCubes reconstruction algorithms aim for high energetic events with much more hits then were used in this study. However, it goes to show, that dedicated low-energy reconstruction techniques are needed in order to study physics at energies below ~ 50 GeV. With the dense spacing and the clear ice, a larger fraction of unscattered hits are expected in DeepCore. Unscattered hits are typically increasing the quality of track reconstruction and thus such dedicated low-energy techniques seem feasible. Therefore this result has not been interpreted against the dense spacing of configuration _A7_, although, from reconstruction arguments, configurations _A4_ and _A8_ pose a more conservative approach, in enlarging the effective volume for events at a few 100 GeV and aiding classic track reconstructions at these energies.

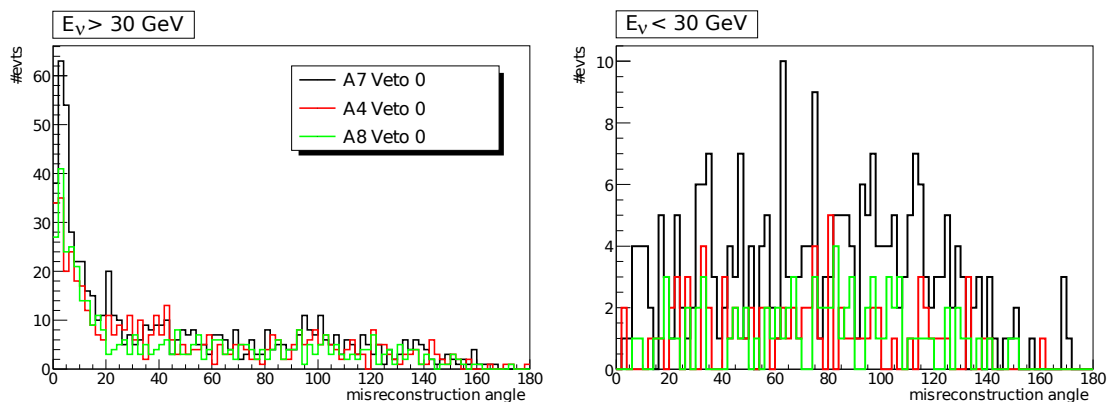**Figure 5.17: Angular mis-reconstruction of muon neutrino tracks in configu-rations _A7_, _A4_ and _A8_** - Left: Muon neutrino energies above 30 GeV; Right: below 30 GeV.

5.5.4.4 Final string layout

From the arguments presented above, a final decision was made to deploy the additional DeepCore strings with configuration _A7_. In summary, the arguments for this option are:

- Best atmospheric muon veto performance:
  - After all veto cuts the fiducial volume will be limited to the bottom part of the detector, below the dust layer, for all configurations
  - 10 extra DOMs in the upper half are sufficient to decrease the amount of leaking vertical muon background
  - the dense module spacing guarantees best signal efficiency for downwards-going neutrino events.

- The dense DOM spacing further lowers the energy threshold of the detector, potentially allowing for a wider range of physics cases

The increased efficiency in detection of the lowest energetic events at ~ 10 GeV and below, was confirmed also in an independent trigger rate study of configurations _A7_, _A4_ and _A8_ [58].
All DOMs on the DeepCore string have been decided to be equipped with the new high QE PMTs as the increased optical efficiency significantly enlarges the effective volume

and the larger noise rate is bearable.

The finally deployed strings have a small change in the DOM-to-DOM spacing of the bottom 50 DOMs. This is now at 7 m, instead of the 7.5 m used in the simulated configuration *A7*. This ensures that all 50 DOMs are positioned clearly below the main dust layer and the full potential of the increased quantum efficiency is used. In addition to the high QE DOMs on the additional DeepCore strings also the bottom of the central IceCube string (number 36) has been equipped with 14 high QE DOMs to have a more homogeneous instrumented central part of DeepCore.

5.6 Ultra high energy extensions and the impact on Deep-Core

In parallel to the plans and design of DeepCore as a low energy extension, also plans arose to improve IceCube at the highest energies. In contrast to the denser string spacing in DeepCore, a higher effective area at the largest energies can only be achieved by a larger geometrical volume, which results in a larger string spacing if the number of strings is fixed. Consequently, the plan involved the replacement of some of the outer baseline strings, as depicted in fig. 5.18. A consequence of such a spacing is that the moved strings do not contribute to the veto anymore, or only in a reduced way, as more events can sneak through the (wider) gaps between strings. To quantify the effect, the final veto studies performed to determine the DeepCore string spacing (configurations *A7*, *A4* and *A8*), have been partially repeated with the modified geometry given in fig. 5.18. In a first approach, the veto volume definition of the L1 veto (version 0) was kept as in the design study. Thus the outer veto is reduced to a 2 string layer for almost half of all directions. The effect is clearly seen fig. 5.19 for the configuration *A7*. In the regions of the 2 string layer veto a significantly increased number of events leak deep into the detector without being removed. This increased L1 background can be compensated for by the L2 vertex cuts, as seen from table 5.2, but at the expense of a reduced final fiducial volume and signal efficiency.
 By tightening the L1 fiducial volume to only the innermost 13 strings associated with DeepCore, the L1 veto performance can be mostly recovered, except for the directions to the bottom of the baseline detector in fig. 5.18, where two strings have been moved out from the outer baseline string layer. This can not be compensated for without further reducing the fiducial volume, a measure that would decrease the useable densely
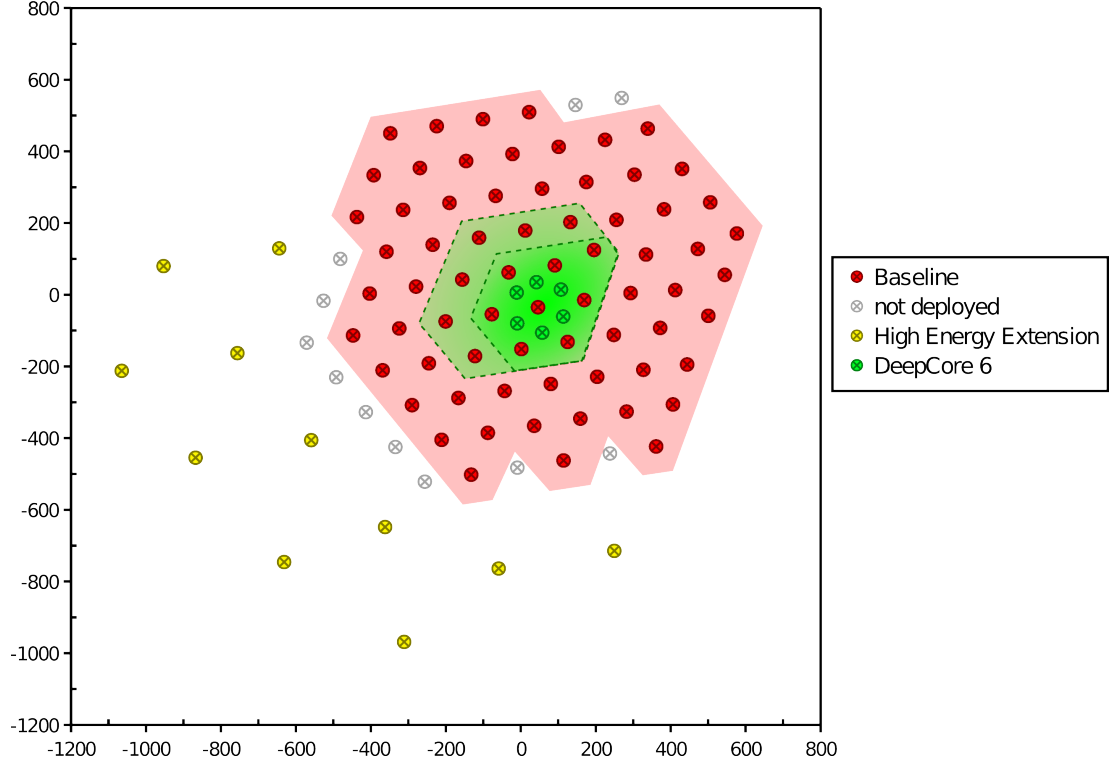
Figure 5.18: Layout and Veto volume definitions for the ultra high energy extension impact studies - DeepCore String Layout *A* with ultra high energy strings (yellow) (moved to greater string spacing) and original baseline position of moved strings (grey). Two possible veto volumes are indicated, a "thin" veto corresponding to the veto 0 definition (see fig.5.10) and a tighter veto to partially compensate the effect of the missing strings.

Figure 5.19: Reconstructed vertex of atmospheric muon background in Configuration *A7* with veto 0 and high energy extension - Left: Top view (x vs. y position of the vertex); Right: Side view (x vs. z). From [43].

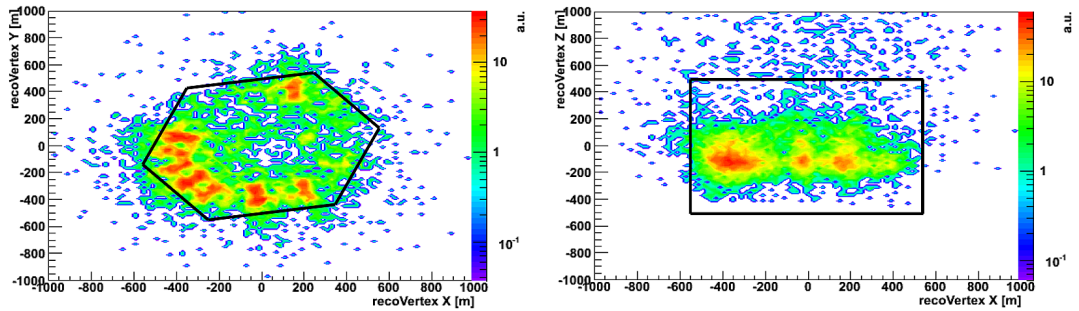|	Configuration *A7*			Configuration *A4*			Configuration *A8*		
	R [m]	z [m]	llh	R [m]	z [m]	llh	R [m]	z [m]	llh
cut parameter values	230	-115	-6.5	230	-195	-4	220	-200	-4
resulting volume ($10^6 m^3$)	63.98			50.69			45.62		
Atm. μ background (L1)	9644			7723			8023		
Atm. μ background (L2)	1			1			1		
Atm. ν_μ signal (L1)	845			603			590		
Atm. ν_μ signal (L2)	118			95			90		

Table 5.2: Signal and background event numbers for configurations A4,A7 and A8 with high energy extension and thin veto - L1: Geometrically penalized veto version B (cut $W_{tot} > 60$); L2: Vertex cut (parameters in table)

instrumented volume, which is clearly not desirable.

From these studies it was recommended that a high energy extension, if built, should be limited to 9 moved strings. Thus the movement of the 2 strings, which could not be compensated for by the veto definition, could be avoided.

At the end, a decision against a movement of baseline strings was made, strengthening the DeepCore performance not only through the veto, but also through the availability of strings number 79 and 80, which will now be part of DeepCore.

5.7 Relocation of strings 79 and 80: Design study for DeepCore

The two IceCube baseline strings with numbers 79 and 80 had to be relocated due to debris in the ice that endangered drilling at the original location. To show the impact these two strings could have, when deployed in DeepCore, and at the same time to find an optimal position for these strings, a new design study was started. Simulations of signal muon and electron neutrinos were done with the decided DeepCore geometry and three different positions for the two new strings. These strings were chosen to have the same DOM-to-DOM spacing as the other DeepCore strings (50 DOMs in the bottom of the detector at a 7 m spacing, 10 DOMs above the dust layer at a 10 m spacing). They were simulated with standard, non high QE DOMs, as such an upgrade would have required extra funds.

The three potential positions of the extra string pair are shown in fig. 5.20. Pair 1 (yellow dots) is the natural choice for an extension at the same energy range as the "standard" DeepCore. The two strings are positioned in a 72 m spacing to two of
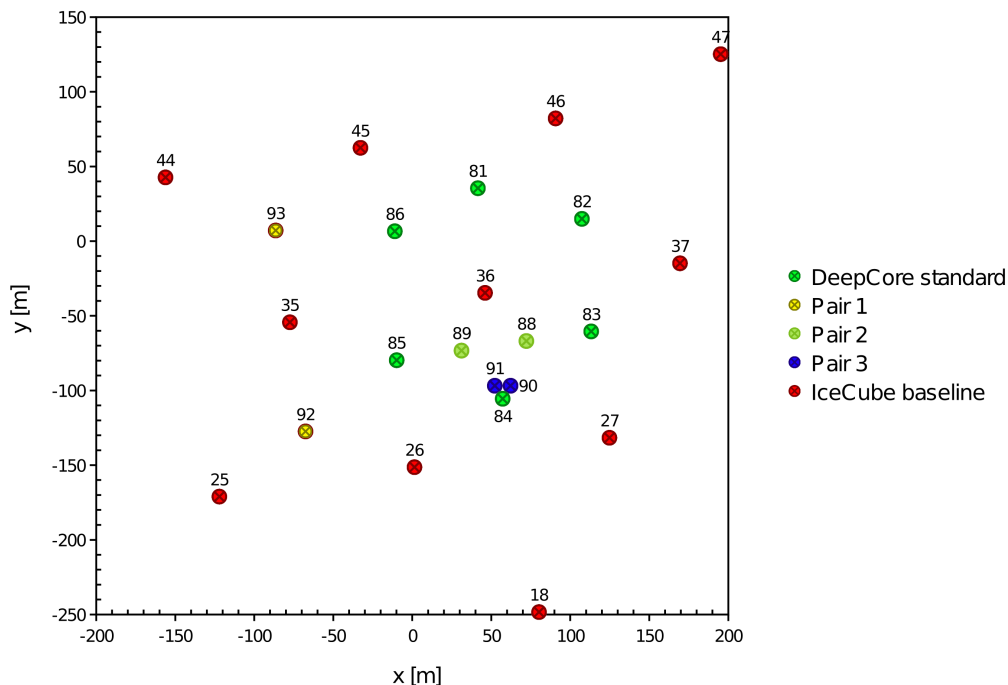
Figure 5.20: Potential positions of strings 79 and 80 in DeepCore - x and y positions of the DeepCore and inner IceCube baseline strings along with three pairs (1-3) of possible positions for strings 79 and 80 in DeepCore.

the baseline IceCube strings associated with DeepCore and the DeepCore neighbor string 35. Pair 2 and pair 3 aim for a lowering of the energy threshold and thus they are positioned within the central DeepCore fiducial volume. Pair 2 is located at the centers of two triangles formed by DeepCore strings and the central IceCube string, at a spacing of 42 m, while pair 3 is set in an extremely dense spacing of 10 m, forming an equilateral triangle with DeepCore string number 84.

The studies of these new geometries were performed on trigger level and were focused on signal efficiency and basic quality parameters for event reconstructions. No veto study was performed as the background rejection found in the previous study had already shown that an atmospheric muon veto is feasible, and additional strings could only strengthen the veto.

The basic event parameters looked at in this study are shortly explained here:

- **Nchannel:** The number of launched DOMs within one event. Nchannel is loosely correlated with the energy of an event. Typically only hard local coincidence

115

(HLC) launches are taken into account.

- **Nstring:** The number of strings with at least one launched DOM. Nstring gives a hint on the reconstruction quality of an event, as three strings are needed to have a good handle on the direction through triangulation.

- **Ndir:** The number of (potentially) unscattered hits. To calculate Ndir a track hypothesis is necessary. A hit is thought to be "direct" if it arrived within a designated time window around the arrival time of an unscattered photon, as expected from the track hypothesis. The time delay between the expected and the actual time of a launch is called "time residual". A typical time residual window for a hit to be regarded direct is -15 ns to $+75$ ns.

- **Effective area:** The effective area A_{eff} relates a measured event rate $\mathcal{R}_{exp}(\theta)$ to the total incident flux Φ:

$$\mathrm{d}\,\mathcal{R}_{exp}(\theta) = A_{eff}(\theta, E) \cdot \frac{\mathrm{d}\,\Phi}{\mathrm{d}\,E}\,\mathrm{d}\,E \tag{5.1}$$

Here θ is the event zenith angle. The energy dependence of A_{eff} is introduced through the energy dependence of the detector efficiency. In IceCube A_{eff} is typically given related to a neutrino or a muon flux. The concept of an effective area is based on the assumption of infinite tracks (where only the projection of the detector volume into the plane perpendicular to the event direction is of importance). This is well justified for muons with a few 100 GeV as these can cross the whole detector, but at the lowest energetic events effective volumes pose a clearer definition.

- **Effective volume:** The effective volume V_{eff} gives the relation between the measured event rate $\mathcal{R}_{exp}(\theta)$ and the true total event rate per unit volume $\mathcal{R}_{tot}(\theta)$:

$$\mathrm{d}\,\mathcal{R}_{exp}(\theta) = V_{eff}(\theta, E) \cdot \frac{\mathrm{d}\,\mathcal{R}_{tot}(\theta)}{\mathrm{d}\,E}\,\mathrm{d}\,E \tag{5.2}$$

If the signal events are restricted to a fixed volume the effective volume can approximately be calculated as the product of signal efficiency and the geometrical volume containing the signal.

Results for Nchannel, Nstring, Ndir and the effective area are shown in fig. 5.21 for muon neutrinos with an E^{-2} spectrum. The improvement seen for electron neutrino cascades are quite comparable and not shown here. The detector trigger condition is a simple multiplicity trigger asking for at least 4 HLC hits within the DeepCore volume
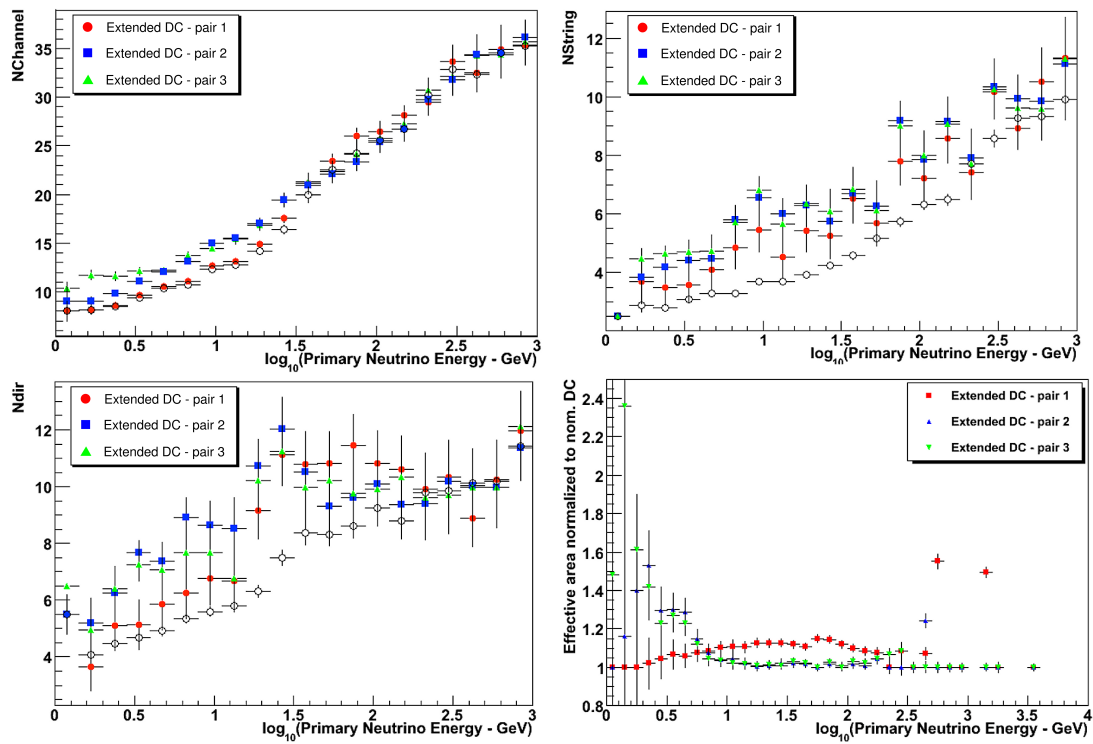
Figure 5.21: Basic event parameter improvements at possible DeepCore locations of string 79 and 80 - Top left: Mean Nchannel peer event vs. neutrino energy; Top right: Mean Nstring per event vs. neutrino energy; Bottom left: Mean Ndir per event vs. neutrino energy; Bottom right: Effective area vs. neutrino energy.

(SMT 4). The top left plot in fig. 5.21 gives the mean number of launched modules, Nchannel, in dependence of the incident neutrino energy. It shows a significant improvement only below 100 GeV and for pair 2 or 3. However, two effects are overlapping here. The additional hits in events that were already triggered without the extra strings pull the mean Nchannel up, but newly triggered additional events with Nchannel close to the trigger threshold pull it down. Thus the effect of additional information, aiding event reconstruction, is somewhat underestimated. A similar improvement as for Nchannel is seen for the mean number of strings with at least one launch per event, Nstring (top right plot in fig. 5.21). The improvement in Nstring is of special interest because events with more involved strings are typically better reconstructed as each additional string adds a new "viewing angle" on the event. This is especially true at the lowest energies where only few strings are involved.

As unscattered hits give unperturbed information on the light emitting particles they

are of special value for reconstructions. The improvement in this variable, Ndir, is seen in the bottom left plot of fig. 5.21. Also here, an improvement is mainly seen below 100 GeV. The observed structure, with a clear rise of the number of direct photons up to $log_{10}(E_\nu) \approx 1.5$ and a flattening of the rise above this energy can be explained by event topologies. Low energetic, short tracks radiate less light and thus they predominantly trigger nearby DOMs, which increases the chances of the light being unscattered. Therefore, at these energies, Ndir rises along with Nchannel. As the muon energies rise, more light is radiated and further away placed DOMs are being hit. But for these the probability of an unscattered hit is much smaller and thus the fraction of direct hits in all hits decreases as the energy rises and accordingly the increase of Ndir with neutrino energy gets flatter.

The effective areas of the three optional detector configurations with strings 79 and 80 are shown in the bottom right plot of fig. 5.21. They are normalized by the effective area of the nominal DeepCore without the additional two strings to illustrate the improvement. Here also an increased efficiency with pair 1 is seen, which is strongest in the energy range between 10 and 100 GeV. This is consistent with the improvement in the nominal DeepCore, which has the same string spacing. Pair 2 and 3 improve the effective area exclusively below 10 GeV (the apparent rise at ~ 3 GeV is a statistical artifact and should not be regarded).

Even though the effective area is not an ideal parameter at the lowest energies, the results are overall consistent with an independent effective volume study. For this study, the signal efficiency of all downwards-going muon neutrino events with an interaction vertex inside the DeepCore fiducial volume, has been calculated and scaled with the water equivalent mass of this volume. The chosen volume is a hexagonal cylinder with the corners formed by IceCube baseline strings not associated with DeepCore (see fig. 5.22). With a diameter of $\sim$500 m and a height of 350 m this volume corresponds roughly to the fiducial volume defined by the reconstructed vertex cut used in the previous design study (see tab. 5.1). The resulting volume is $\sim$52 megatons of water equivalent. Results are shown in fig. 5.23. In addition to the 3 configurations used before, a configuration has been considered in which also the lower parts of two more IceCube baseline strings add to the DeepCore trigger for pair 1. This option is reasonable, as these two strings are close to strings 79 and 80 in this configuration. The top left plot of fig. 5.23 shows the effective volume for energies up to 10 TeV, where almost 100% signal efficiency is reached[1]. Here mainly the improvement by pair 1 is visible, which is seen at all energies above 10 GeV until the signal efficiency saturates. The top

---

[1]Remember: the signal is formed by events with an interaction vertex in DeepCore.
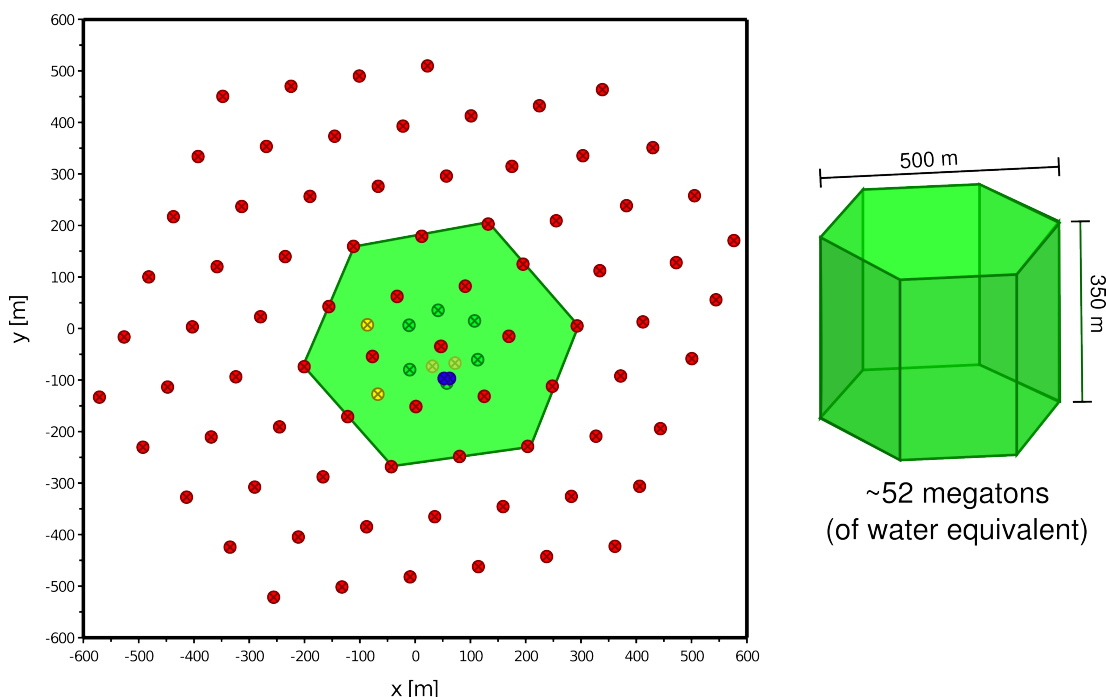
Figure 5.22: Geometric volume definition for effective volume calculation - Left: Top view; Right: sketch of the geometric volume size and shape.

right plot shows V_{eff} at the lowest energies in a logarithmic scale, which illustrates the improvement at the lowest energies gained by pair 2 and 3. As for the effective area, this improvement is only observable at energies below 10 GeV. The bottom plots show the ratios of the effective areas to the effective area of the nominal configuration and thus illustrate the above described improvements.

In summary, pair 1 gives the best improvement in the shown event parameters at energies above 10 GeV, which are already accessible with the nominal DeepCore. It improves the effective volume at these energies, but there is only little to no gain in Nchannel or Nstring per event. So, we do not expect a big gain in event reconstruction capabilities from this configuration. Pair 2 and 3 improve the performance mainly at the lowest energies below 10 GeV, with pair 3 reaching even lower energies than pair 2. Both options add new information to existing events which could be crucial for the development of dedicated low energy event reconstructions. However, pair 2 seemed to be the most promising configuration. It shows good improvements of the relevant parameters in the range from several GeV to some tenths of GeV, which are especially

119
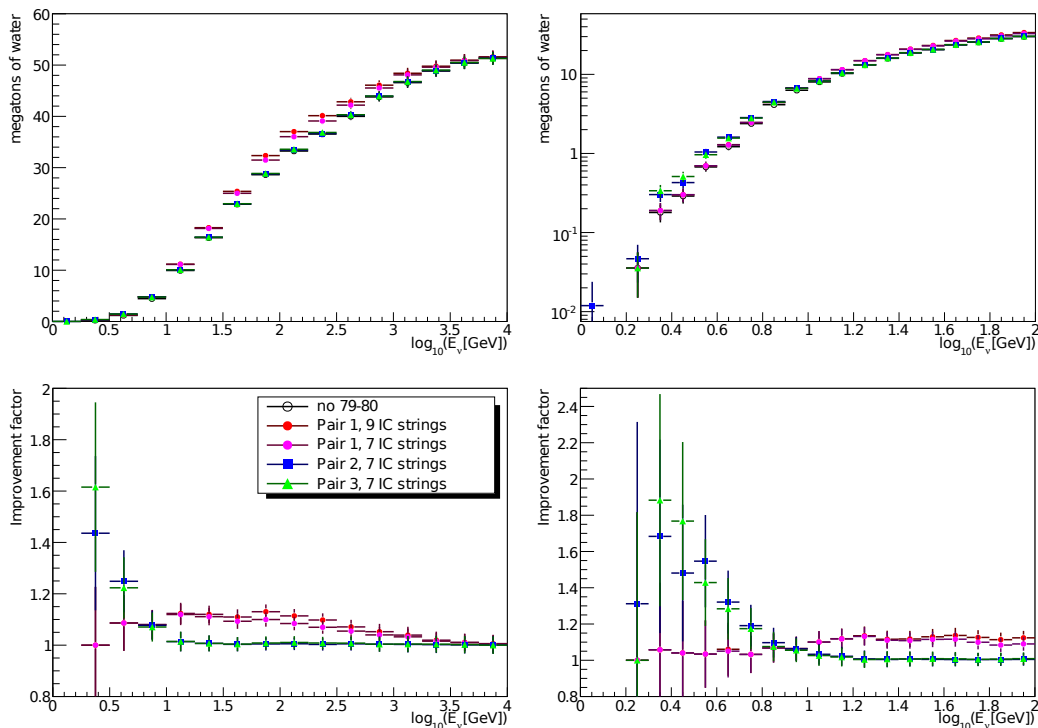
Figure 5.23: Effective volume of DeepCore with optional locations of strings 79 and 80 - Top left and right : Effective volume vs. neutrino energy at all relevant and the lowest energies, respectively. Bottom: the corresponding improvements, defined by the ratio to the effective volume of the nominal DeepCore 6 string configuration

relevant for neutrino oscillation physics, thus improving DeepCores capabilities in this challenging, but highly interesting research field.

Following these arguments the pair 2 locations were proposed to the collaboration as new positions for strings 79 and 80. The decision to deploy these strings at the proposed position was made in 2009 and the deployment will take place in the upcoming final IceCube deployment season 2010/11.

6

Vetoing atmospheric neutrinos in a high energy neutrino telescope

In chapter 3 we have illustrated how high energy telescopes, such as IceCube, search for muon neutrinos from extra-terrestrial sources by using the large mass of the Earth as a filter to suppress the large background of atmospheric muons. By thus looking primarily for upward or horizontally moving muons induced by neutrino interactions ($\uparrow\nu_\mu$- $\uparrow\mu$), the downward-going atmospheric muons ($\downarrow\mu$) are prevented from being mis-identified as being neutrino-induced.

This detection principle implies the limitation of the field of view to the hemisphere opposite to the detectors location. Furthermore, as another consequence, the upward-going atmospheric neutrinos become an irreducible background. The standard approaches to separate a potential astro-physical neutrino signal from this background are the point-source and diffuse searches (see section 3.6), focusing on the neutrino direction and energy, respectively.

In the previous two chapters it has been described how, in the course of the DeepCore design study, the veto against atmospheric muons for IceCube has been developed. By using a large part of the detector volume to identify the ($\downarrow\mu$), a central nested array, DeepCore, can be used to look for ($\downarrow\nu_\mu$) which interact within the fiducial volume. This technique opens the possibility to extend the searches for extra-terrestrial neutrinos to the hemisphere of the detector location, i.e. for IceCube, the southern hemisphere.

In the course of this development we discovered a new, unlooked-for, opportunity to reduce the background of atmospheric ($\downarrow\nu_\mu$). For IceCube this reduction follows naturally from the veto-technique and the kinematics of the cosmic ray air-shower, which produces this background. Both, the atmospheric ($\downarrow\mu$) and ($\downarrow\nu_\mu$) predominately arise

from the same decays of pions and kaons within the air-shower. At the very high energies involved at neutrino telescopes, the ($\downarrow\mu$) and ($\downarrow\nu_\mu$) have a high probability of traversing the atmosphere quasi aligned (see section 2.2.3). Thus it is possible that a atmospheric ($\downarrow\nu_\mu$) will arrive at the detector along with its partner ($\downarrow\mu$), assuming the muon has sufficient energy to reach the required detector depth. If the ($\downarrow\mu$) is identified by the muon veto, it can "tag" the ($\downarrow\nu_\mu$) as being of atmospheric origin.

In this chapter we present an analytical approach to estimate this effect independently from any given detector setup or veto technique. We will derive the probability that an atmospheric ($\downarrow\nu_\mu$) is accompanied by its partner ($\downarrow\mu$), based on the approximate descriptions of the atmospheric neutrino flux derived in section 2.2.2. We find, that the probability depends mainly on the neutrino energy and zenith angle, as well as the depth of the detector and will illustrate the respective dependencies. This work has been published in [85].

6.1 Calculation of the atmospheric neutrino veto probability

The general idea of this estimation is to calculate the spectrum of all atmospheric ν_μ (as has been done in section 2.2.3) as well as the spectrum of neutrinos which have an accompanying muon of some minimal energy $E_{\mu,min}$, needed to reach a certain detector depth. The ratio of the latter with the full neutrino spectrum then gives the fraction of neutrinos with an accompanying muon at depth in dependence of the neutrino energy. We define this fraction as the atmospheric neutrino veto probability:

$$P_{\text{veto}}(E_\nu, \theta_\nu) \;=\; \frac{\phi_{\nu, E_{\mu,\text{min}}}(E_\nu, \theta_\nu)}{\phi_{\nu,\text{full}}(E_\nu, \theta_\nu)} \tag{6.1}$$

For a real detector the muon veto and signal efficiency, as well as the capabilities in energy and directional reconstruction may limit this veto effect. So, in this respect one may interpret our approach as assuming a perfect detector, which will fulfill all this tasks with 100% efficiency.

The approximate atmospheric neutrino spectrum from decay of pions and kaons can

be taken from equation (2.36) as the sum

$$
\begin{aligned}
\phi_\nu(E_\nu) &= \phi_{\nu\pi}(E_\nu) + \phi_{\nu K}(E_\nu) \\
&= N_0(E_\nu)\frac{\Lambda_N}{\lambda_N} \sum_{j=\pi,K} \frac{A_{\nu j}}{1 + B_{\nu j}\,\xi_j^{-1}(E_\nu)}
\end{aligned}
\tag{6.2}
$$

$$
\text{with} \qquad A_{\nu j} = Z_{Nj}\,(1-r_j)^{-1}\,(\gamma+1)^{-1} z_{min}^{-(\gamma+1)}
$$

$$
\text{and} \qquad B_{\nu j} = \frac{\gamma+2}{\gamma+1}\,\frac{z_{min}^{-(\gamma+1)}}{z_{min}^{-(\gamma+2)}}\,\frac{\Lambda_j - \Lambda_N}{\Lambda_j\,\ln\frac{\Lambda_j}{\Lambda_N}}
$$

Here we already applied the upper integral bound for the neutrino spectrum $z_{max} = \infty$. The lower bound for the full atmospheric spectrum is given in equation (2.32). If a minimal muon energy is also required the lower limit on the parent meson energy becomes $E_j \geq E_\nu\left(\frac{1}{1-r_j}\right) + E_{\mu,min}$ which leads to $z_{min} \geq \frac{1}{1-r_j} + \frac{E_{\mu,min}}{E_\nu}$. However, this relation only governs as long as the required muon energy is larger than the kinematically enforced lower muon energy limit, given in equation (2.24). So the lower bound is fully defined by

$$
z_{min} = \begin{cases}
\frac{1}{1-r_j} + \frac{E_{\mu,min}}{E_\nu} & , \text{if } E_\nu < E_{\mu,min}\left(\frac{1-r_j}{r_j}\right) \\
\frac{1}{1-r_j} & , \text{if } E_\nu \geq E_{\mu,min}\left(\frac{1-r_j}{r_j}\right)
\end{cases}
\tag{6.3}
$$

The muon energy losses in matter are, strictly speaking, stochastic losses, which are usually best described by Monte-Carlo simulations. In IceCube the "Muon Monte-Carlo" (MMC) [22] is used for the simulation purposes, as introduced in section 3.4. For the case of estimating the atmospheric ($\downarrow\nu_\mu$) veto effect however, it is sufficient to use the parametrization of the muon energy losses given in section 3.1.2, equations 3.6 3.7. This parametrization can be rewritten in terms of the minimal muon energy required to reach depth X, as

$$
E_{\mu,min} = 0.73\,\text{TeV} \cdot \left(e^{\frac{X}{2.8\,\text{km.w.e.}}} - 1\right)
\tag{6.4}
$$

This parametrization is valid for muon energies $> 20\,\text{GeV}$.

6.2 Results: The performance of the atmospheric neutrino veto

The behavior of the proposed veto of atmospheric ($\downarrow\nu_\mu$) is depicted in figure 6.1. The lower panel shows the veto probability as defined in equation (6.1) in dependence of the neutrino energy for vertical ($\downarrow\nu_\mu$) ($\cos\theta_\nu = 0$). The various curves represent different
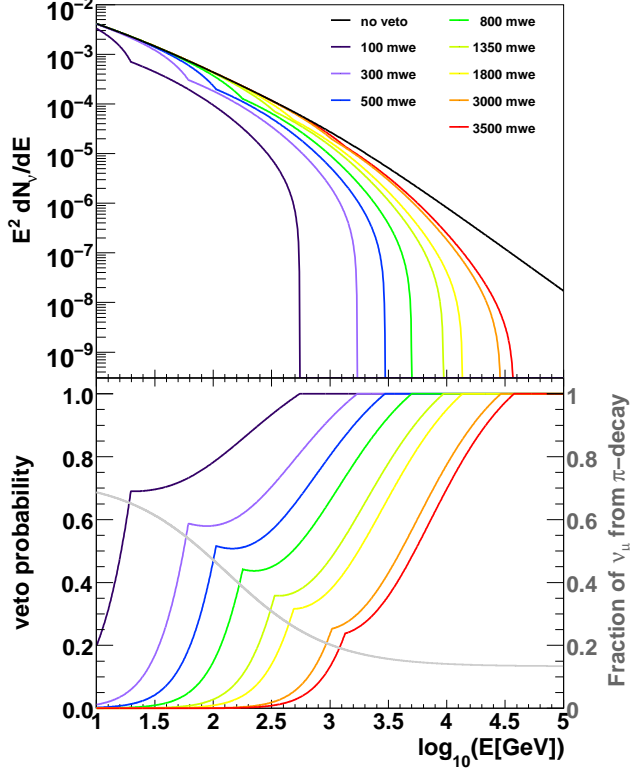
Figure 6.1: Veto probability and resulting spectra for vertical neutrinos - Upper
panel: Flux of vertical atmospheric ($\downarrow\nu_\mu$) without an accompanying muon at eight different
depths; Lower panel: Probability of accompaniment of vertical ($\downarrow\nu_\mu$) for the same eight
depths. The gray curve is the fraction of ($\downarrow\nu_\mu$) from pion decay.

depths in water from 100 m to 3500 m. Once the veto effect kicks in, the probability rises
rather strongly up to a shoulder, where it may even drop again by a small amount. At
increasing energy the probability then rises again, even though less steeply then before,
up to 100%. The explanation for this behavior is found in the different contributions
from pion and kaon decay. As discussed in section 2.2.3, a ($\downarrow\nu_\mu$) from pion decay
will always have a partner muon with, at least, 34% more energy then itself. On the
other hand, the corresponding muon energy in the kaon decay can be as low as 5%
of the neutrino energy. Thus, for neutrinos from pion decay, the probability of an
accompanying muon is rising already at lower energies then for neutrinos from Kaon
decay. Accordingly, the first part of the curves gives the pion contribution to the veto,
saturating at the shoulder of the curve. The second part gives the contribution from
kaon decay. At larger depths, where a higher muon energy is required, the contribution

from kaons rises, leading to a shift of the shoulder to lower probabilities. This is nicely illustrated by the gray curve in the lower panel of figure 6.1, which gives the relative contribution of neutrinos from pion decay defined by:

$$R_\pi = \frac{\phi_{\nu,\pi}}{\phi_{\nu,\pi} \, + \, \phi_{\nu,K}} \tag{6.5}$$

The depths chosen for display in figure 6.1 correspond to the depth of the center of Ice-Cube (1800 m.w.e.), its upper border (1350 m.w.e.) as well as the related depths for a possible km^3-scale detector at the NEMO site, which is the deepest candidate location for Km3NeT (3500 m.w.e./3000 m.w.e.) [18]. Four shallower depths have been chosen, to illustrate the behavior of the veto in this regime, which might be relevant for future experiments.

The upper panel of figure 6.1 shows the atmospheric ($\downarrow\nu_\mu$) spectrum that would remain if all ($\downarrow\nu_\mu$) with an accompanying ($\downarrow\mu$) were removed. One can see that IceCube (lemon-green curve, 1800 m.w.e.) could be virtually "background-free" for neutrino energies just above 10 TeV. For a deeper detector at 3500 m.w.e. this limit is reached at $\approx$35 TeV. On the other hand, a detector with a shallow veto of just a few hundred meters depth could be practically freed from the atmospheric ($\downarrow\nu_\mu$) background at energies as low as 1 TeV. Keep in mind though, that these numbers hold only for vertical ($\downarrow\nu_\mu$).

The zenith dependence of the veto effect is shown in figure 6.2. Each panel displays the veto probability (color scale) in dependence of neutrino energy and cosine of the zenith angle for a different depth. The veto probability drops with increasing zenith angle due to the larger amount of matter that has to be traversed by the muon to reach the designated depth. At the horizon the probability approaches infinity due to the assumption of a flat surface, made in the calculation of the spectra. Note however, that this assumption is nevertheless valid up to $\approx 89°$ ($\cos\theta_\nu \approx 0.02$).

The 90% confidence limit for an accompanying muon is shown in figure 6.3 for the various depths discussed before. For the center of IceCube one can take from this plot a 90% veto probability above $\approx$8 TeV for vertical ($\downarrow\nu_\mu$) and $\approx$23 TeV for ($\downarrow\nu_\mu$) incident at a zenith angle of 60° ($\cos\theta_\nu = 0.5$).

From these results, we conclude that it is principally possible to reduce the background of atmospheric ($\downarrow\nu_\mu$) in a neutrino telescope. Depending on the depth of the detector, the veto effect becomes relevant at different neutrino energies and zenith angles, with a general favor for less deep located detectors.
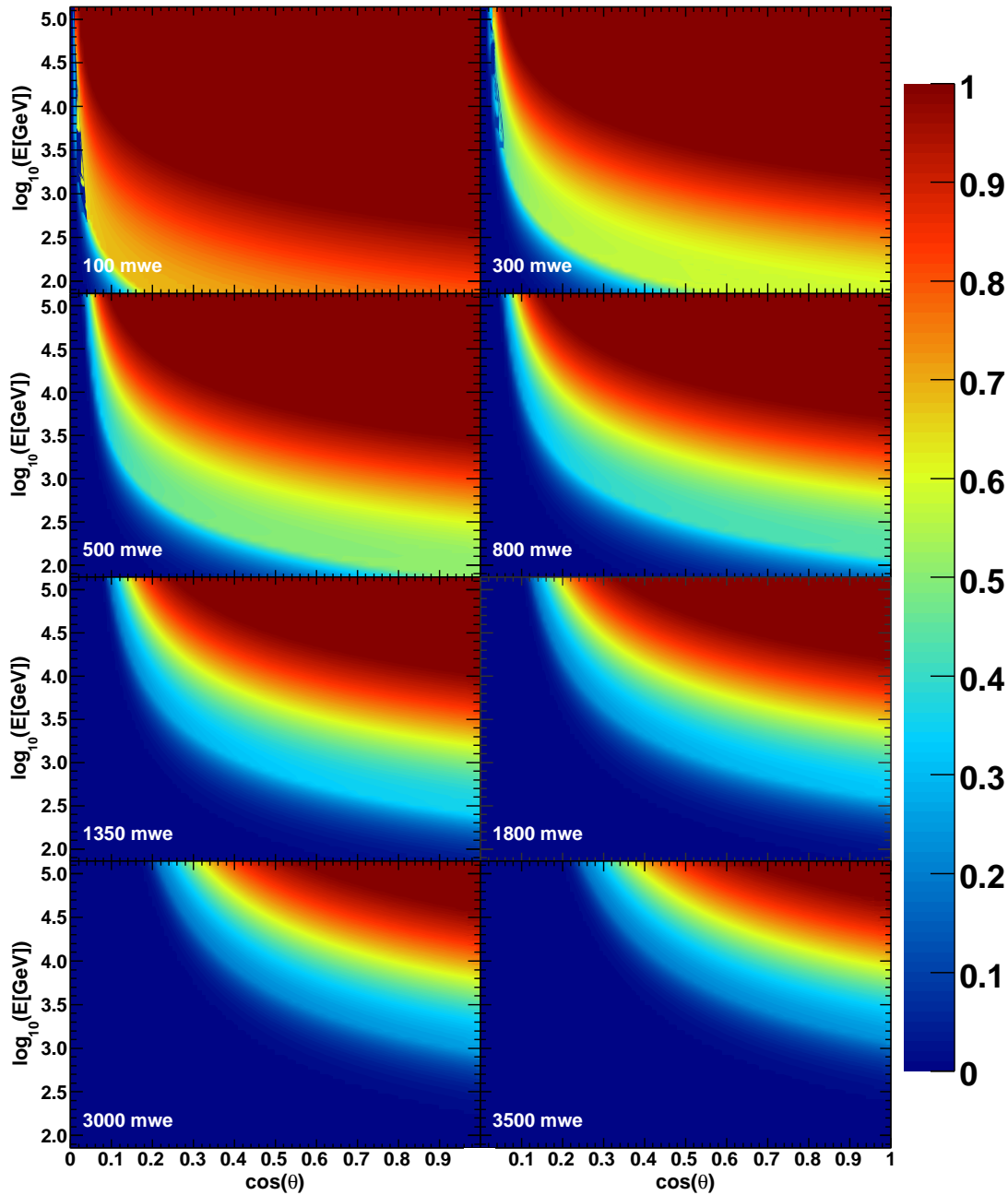
Figure 6.2: Zenith dependence of the atmospheric ($\downarrow\nu_\mu$) veto - The probability is shown (colors scale) in dependence of neutrino energy and zenith angle for 8 different depths in water.
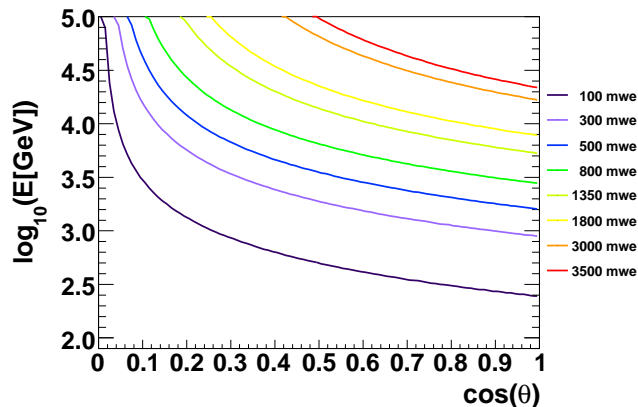
Figure 6.3: 90% confidence level of atmospheric ($\downarrow\nu_\mu$) veto probability - The level of 90% ($\downarrow\nu_\mu$) veto probability is given for 8 different depths in water.

6.3 Contributions from minor channels

Up to now we have restricted ourselves to the most abundant sources of atmospheric ($\downarrow\nu_\mu$), namely the decays of pions and kaons via a two-body decay. In this section we want to assess the effect of other ($\downarrow\nu_\mu$)-producing channels on the veto probability. We therefore estimate the influence of ($\downarrow\nu_\mu$) from three-body kaon decay, muon decay and decay of charmed particles.

6.3.1 Three-body kaon decay

The two most common three-body kaon decays with ($\downarrow\nu_\mu$) in the final state are:

$$K^\pm \rightarrow \pi^0 \ \mu^\pm \nu_\mu(\bar\nu_\mu) \qquad (3.4\%)$$
$$\text{and}$$
$$K_L^0 \rightarrow \pi^\pm \mu^\mp \bar\nu_\mu(\nu_\mu) \qquad (27.0\%) \qquad\qquad (6.6)$$

The branching ratio is given in brackets behind the respective decay. The least favorable situation for the veto is, as before, when the ($\downarrow\mu$) is produced in the opposite direction of the parent boost ($\cos\theta_\mu = -1$). But in contrast to the two-body decay the remaining energy will be distributed over two particles and thus the neutrino energy will be lower. Therefore this channel does not weaken the veto probability. Actually, it is even potentially improving it.

6.3.2 Neutrinos from muon decay

This is the most extreme case from the veto point of view, since there is no chance of an accompanying partner muon. Thus the veto effect will be weakened by the same part as this channel takes in the overall flux of $(\downarrow \nu_\mu)$. The contribution of muon decay to the $(\downarrow \nu_\mu)$ flux can be estimated, as has been done in [73] and is found to be small at large energies. At 10 TeV neutrino energy and zenith angles $< 60°$ the contribution is less than one per mil.

6.3.3 Neutrinos from decay of charmed particles

Neutrinos from the decay of hadrons containing a charm or anti-charm quark are called "prompt", because the lifetimes of such hadrons are so short that interactions with air nuclei hardly ever happen before decay. Thus neutrinos from such channels have harder spectra up to much higher energies (~ 10 PeV) and therefore they contribute stronger at the higher energies.

The relevant decay processes for this assessment are:

$$
\begin{aligned}
D^+ &\rightarrow \bar{K}_0 \; \mu^+ \; \nu_\mu & (9.3\%) \\
D^+ &\rightarrow K^- \; \pi^+ \mu^+ \; \nu_\mu & (3.9\%)
\end{aligned}
\tag{6.7}
$$

and

$$
\Lambda_c^+ \rightarrow \Lambda \; \mu^+ \nu_\mu \qquad (2.0\%)
\tag{6.8}
$$

The masses of the D^+ meson and the Λ_c^+ baryon are significantly higher than that of the kaon (1.86 GeV and 2.29 GeV, resp.). Thus the kinematic situation is even worse than for the kaon decay and the muon can have even lower relative energies in the laboratory frame. On the other hand there are several particles in the final states of this decays and thus the neutrino energy required to see the partner muon is lowered as well.

The contribution from charm decay to the flux of $(\downarrow \nu_\mu)$ can be estimated in the Recombination Quark Parton Model (RQPM) [12]. This model imposes a good estimate, since it nearly saturates the existing upper limits on charm production [54]. At 10 TeV the charm contribution is estimated within this model to be less than 10% and becomes dominant over the ordinary channels just above 100 TeV.

Given the branching ratio and the upper limits on charm contribution, we estimate the weakening of the veto effect by unaccompanied neutrinos from charm decay to be less than 1%.

6.4   Challenges to high energy neutrino telescopes

We have shown that the background of atmospheric $(\downarrow\nu_\mu)$ in the multi-TeV range can be reduced with an efficiency of up to, or more than 99%. The primary requirement to a high energy neutrino telescope in order to use this effect, is an efficient veto system to identify and reject the accompanying muon. It has been shown in previous chapters that such a veto system is existing for IceCube and DeepCore, but a similar system may work for the planned Km3NeT detector. The rejection of events with a muon track in the veto volume in this case inherently implies that also an atmospheric neutrino interacting in the fiducial volume would be vetoed, without any further efforts to be taken. But even though the atmospheric $(\downarrow\nu_\mu)$ veto comes somewhat naturally along with the atmospheric $(\downarrow\mu)$ veto, it is rather difficult to estimate the individual probability of a measured neutrino to be of atmospheric origin. This probability depends primarily on the neutrino energy and zenith angle. The latter can be measured with an accuracy of $\mathcal{O}(1°)$ at the multi-TeV energies where the veto effect is most relevant. The energy on the other hand is much more difficult to determine. Typically energy measurements are on the order of 50% accurate, but since the events in this case are starting within the detector volume, a better energy estimate may be possible by measuring the light from the initial hadronic cascade, which is also proportional to the neutrino energy. Anyhow, due to the steep neutrino spectra most interactions will be near the nominal threshold and thus smearing effects of fluctuations are enhanced. Furthermore, even if the angular reconstruction works well. it is necessary to have very good knowledge of the surrounding detector material (water or ice) and a good understanding of the muon energy losses on the way to the detector.

In reality, detailed Monte-Carlo simulations, including full detector response, are needed to assess the veto effect. Such simulations can also include the additional veto effect from $(\downarrow\mu)$ in other branches of the air-shower. Such muons can potentially increase the veto effect considerably.

It should be noted, that this veto effect imposes not only a (generally welcome) possible reduction of the background to searches for neutrinos of extra-terrestrial origin, but also a systematic effect to any analysis of atmospheric $(\downarrow\nu_\mu)$ fluxes, including neutrino oscillation analyses.

Apart from the already existing or planned experiments, the possibility to reduce the background of atmospheric $(\downarrow\nu_\mu)$ might also influence detector concepts of future neutrino telescopes. In the past it was generally considered more favorable to built

neutrino telescopes with larger overburdens to stronger reduce the background of atmospheric $(\downarrow\mu)$. The proposed veto effect on the other hand calls for detectors at shallower depths as the $(\downarrow\mu)$ can actually provide the information to get rid of the $(\downarrow\nu_\mu)$ background. In principal it is only the veto system which takes benefit from shallower depths and thus the fiducial volume could be detached and at larger depths. This would also have the additional benefit of increasing the effective volume of such a detector. Admittedly though such a shallow veto system imposes several difficulties at this time:

- With increasing distance to the fiducial volume the veto detector needs to cover an ever wider area or the veto will be limited to the near vertical events.

- lower depths in ice or water call for different detection techniques or denser instrumentation as the optical properties get worse near the surface.

Surface air-shower arrays, such as IceTop, could in principle provide the veto of atmospheric $(\downarrow\mu)$ (and thus $(\downarrow\nu_\mu)$), but they would also need to be rather dense and large, leading to potentially irrational costs.

Nevertheless, it may well be that future techniques will allow for a shallow (or surface) veto detector to be build which would be both effective in the veto performance and instrumentation cost. A neutrino telescope almost free of the $(\downarrow\nu_\mu)$ background is certainly an objective that is most attractive to an astro-particle physicist and worthwhile to be pursued.

7

First look on DeepCore data and a first sensitivity estimation to a southern hemisphere point source

By the time this thesis is written, six of eight DeepCore strings are deployed and the data taking with a dense fiducial, and a full veto volume is about to start. In this chapter we want to give a first look on the data collected by the deployed dedicated DeepCore strings and we will review the involvement of these strings in dedicated triggers and filters. We show that they are taking data smoothly, and in an expected manner.

As the data taken from this point, is planned to be used to perform the first low-energy, muon neutrino point source search in the southern hemisphere with IceCube, we present also a first result of the on-going analysis developments, a sensitivity to southern sky point sources at a low analysis level.

7.1   DeepCore strings in the ice: A first look study

The first DeepCore string (number 83) was deployed in January 2009 and was fully integrated into the data taking of the following season with a total of 59 strings. At the time of the writing of this thesis, there are 79 strings deployed and six of them are dedicated DeepCore strings. The full data taking with this configuration is going to start soon.

This section comprises a short summary of the running data taking mode with one DeepCore string and a look into the first strings performance, as well as an outlook on

the upcoming data taking period.

7.1.1 First DeepCore string: The IceCube configuration with 59 strings

The data taking with a 59 string detector configuration was started in April 2009 and was still ongoing at the time this thesis was written. The configuration incorporates the first dedicated DeepCore string (number 83) which was fully integrated in the data taking. Three of the surrounding baseline IceCube strings associated with DeepCore were also deployed, giving effectively four strings in a dense module spacing. Due to the deployment plan, the center of IceCube was still completely open to one side and no veto, of the form discussed in chapter 4, could be applied. The DeepCore string was included in the standard simple multiplicity trigger (SMT) of IceCube asking for 8 or more HLC hits in the whole detector (SMT8). Additionally a dedicated DeepCore SMT requiring a minimal multiplicity of 3 hits was established (SMT3).

This data-taking period was considered mostly a testing phase for DeepCore in which trigger and filter rates, as well as other direct observables could be measured, compared with Monte Carlo predictions, understood and eventually tuned. Therefore the filter applied to events which triggered the DeepCore SMT3 was simply down-scaling the event rate by sending only every 35th event to the North. This data amount was sufficient to fulfill the necessary tasks, and the full data stream was saved on tapes at pole. Apart from this, there were few more dedicated low-energy filters incorporating the first DeepCore string, but also these were down-scaled and mainly aimed to understand the data and develop and improve future analyses.

One of the first performance tests immediately done after the string deployment, is an occupancy check. The occupancy is defined as the rate at which each individual DOM contributes a launch to a triggered event. This rate changes strongly while the hole refreezes and it takes several weeks until it reaches a stable level. In fig. 7.1 we show the occupancy of the DOMs on the first DeepCore string in comparison to a baseline IceCube string (string 55) versus the deployment depth of the modules. In this case, the rates include the SLC launches, which nonetheless did not enter into the trigger logic.

As can be seen from fig. 7.1, the rates on both strings show similar peaks and dips, as these trace the optical properties of the ice. However, the occupancy of the DOMs on the DeepCore string are higher then on the standard string at all energies. This is expected, as the DeepCore string is equipped with high QE DOMs which increase the individual DOM launch rate approximately by the same amount as the quantum effi-
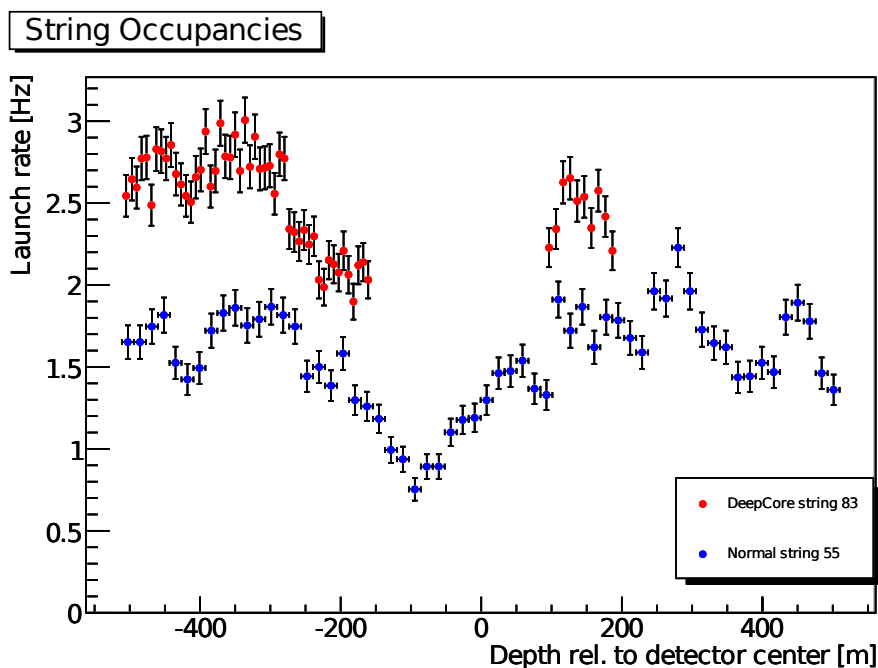
Figure 7.1: Occupancy of the first DeepCore string - The read-out rate (occupancy) of the first deployed DeepCore string (number 83, red) is shown in comparison to a standard IceCube string (number 55, blue). The x-axis gives the depth of the respective modules w.r.t. detector center, such that the dense DeepCore spacing and concentration to the bottom of the detector is clearly visible. The dip at ∼-100 m corresponds to the main observed dust layer.

ciency is increased with respect to a standard DOM (∼35%, see section 3.3.5). But this is not the only effect measured in the plot. In the bottom part of the detector (-500 m to -100 m) the rates are on average ∼ 60% higher, while on the 10 DeepCore DOMs in the top, the increase is smaller at ∼ 30%. This latter increase corresponds roughly to what is expected from the high QE DOMs, which is explained by the fact, that these upper DOMs take part in the IceCube SMT8, but not in the DeepCore SMT3 trigger. Furthermore they have a 10 m DOM-to-DOM spacing instead of 7 m as in the fiducial volume. This also decreases the occupancy in this part. The lower multiplicity of the SMT3, applied to the bottom 50 DOMs, leads to a larger number of triggers and read out events, which raises the occupancy of the fiducial volume modules to the observed value. Thus the behavior of the DOMs on the first DeepCore string is generally well understood and controlled, and no problems were found that could have stopped or delayed a deployment of the following DeepCore strings.

7.1.2   Six DeepCore strings: The IceCube configuration with 79 strings

With 79 strings deployed and 6 of them being dedicated DeepCore strings, DeepCore today has a full veto shield and a densely instrumented fiducial volume. After the successful deployment of the first DeepCore string, also the five new DeepCore strings were commissioned without complications and show reasonable rates. The detector is thus ready for dedicated low-energy data-taking and this is reflected in the triggers and filters planned to be run with this configuration, starting in spring 2010. At the time this thesis is written, the data-taking in this new configuration has not yet started, but first test-runs have been made to test the new triggers and filter algorithms.

DeepCore will be triggered, as before, by an SMT3 trigger now incorporating an overall of 13 strings and 454 modules. The measured rate of this trigger, at ~ 180 Hz, is slightly larger then expected from Monte Carlo, which is understood as an effect of the ice simulation at large depths. The interpolation of scattering and absorption coefficients via dust profiles (see section 3.2) somewhat underestimates the clear ice at the bottom of the detector, thus yielding lower trigger rates.

A filter employing the causally related hit veto algorithm (see section 4.4) will be run as a basis for low-energy analyses aiming for downwards-going neutrinos. To retain a maximum of signal, the algorithm will be run exclusively on HLC hits, as the resulting background rejection should be sufficient to reduce the filter rate in a way that only a reasonable amount of bandwidth for submission to the North is taken by this filter. This filter rate has been determined from Monte Carlo to be at ~ 20 Hz and preliminary test run results show that this goal is met. In fig. 7.2 we show a detector view of a potential signal event which survived the veto filter. The event was measured on the 20th of April 2010 within a test run. The optical modules are represented by white dots, while the larger colored blobs represent hit DOMs. The color denotes the timing of an event (red: early; blue: late) and the size of a blob the charge deposit. This can also be taken from the panel on the right side of the figure. In the given view, only the HLC pulses are shown which also were used in the veto algorithm. From the color code we can infer that this was a downwards moving event with no HLC hit on the outer three string layers or the top of the detector, which agrees with the topology of the envisaged signal events.

We conclude, that the deployed modules behave in the expected way, and that DeepCore is now ready for its first full data taking season.
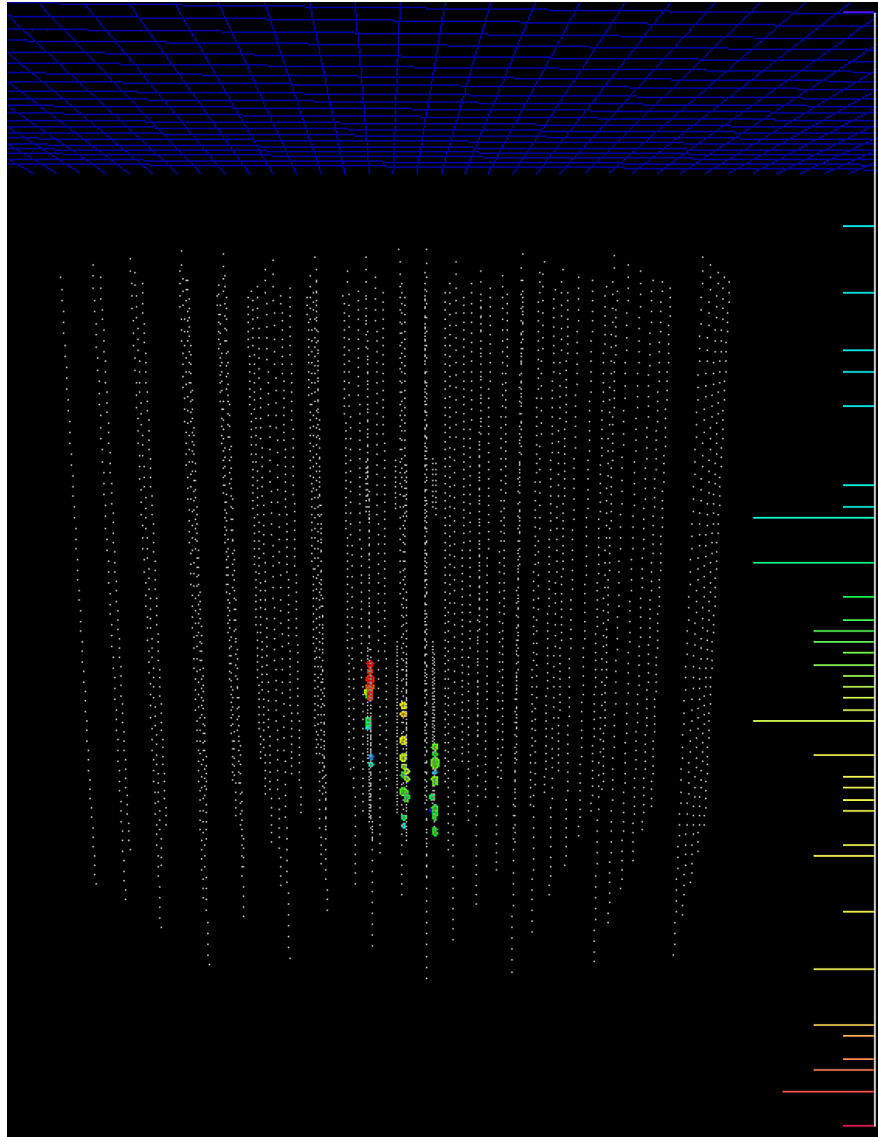
Figure 7.2: Event view of a downwards-going signal candidate event - The event was measured in a test run of the trigger and filter settings for the full deployed IceCube configuration with 79 strings. Only HLC pulses are shown. The color of the blobs denotes the timing (red: early; blue: late), while the size gives the relative charge deposition per DOM.

7.2 First sensitivity estimation to a southern hemisphere point source

With the upcoming data taking period, full veto capabilities are provided for a fiducial volume with six dedicated DeepCore strings. It is for this configuration that we estimate the sensitivity to the brightest source in TeV γ-rays in the southern sky, the supernova remnant RX J1713.7-3946 [28]. This source is located at

$$\alpha = 17:13:00\,\text{h}, \qquad \delta : -39:45:00\,\text{deg}. \tag{7.1}$$

The sensitivity is estimated on a low muon neutrino analysis level, which omits any muon track reconstruction and can therefore be seen as an optimistic, but realistic approximation. Moreover, the fiducial volume and muon veto efficiency have not been optimized for the best sensitivity yet.

We will first present the simulations on which the results are based and give the achieved muon veto performance. Then we explain the used parameters of the point source search and the sensitivity calculation. Finally we will apply the veto probability to atmospheric neutrinos as analytically calculated in chapter 6. This provides an estimate of the improvements to the sensitivity following this effect.

The work on the sensitivity is on-going and the results presented in this section mark only a first step in the first neutrino point source analysis that restricts exclusively to neutrino events which start inside the detector. The most important result can therefore be considered to be the found improvement to the sensitivity induced by the atmospheric neutrino veto.

7.2.1 Simulations

In this study $\sim 2 \cdot 10^7$ background CORSIKA air showers have been used to evaluate the veto efficiency. The signal simulations comprise $\sim 4 \cdot 10^8$ muon neutrino events generated with Neutrino Generator and a generic E^{-2} spectrum. This latter set is re-weighted to the source spectrum of RX J1713.7-3946 using a flux obtained in [68]:

$$\frac{\mathrm{d}\,N_{\nu_\mu}}{\mathrm{d}\,E_{\nu_\mu}} = 15.52 \left(\frac{E_{\nu_\mu}}{[1\,\text{TeV}]} \right)^{-1.72} \exp\left(\sqrt{\frac{E_{\nu_\mu}}{1.35\,\text{TeV}}} \right) \cdot 10^{-12}\,\text{TeV}^{-1}\text{cm}^{-2}\text{s}^{-1} \tag{7.2}$$

This flux was calculated using the method described in 2.4.3, to estimate a potential neutrino flux from the observed γ-ray flux. The fit to the γ-ray data, on which this calculation was based, is one of a couple of equally matching fits [30], and therefore the chosen flux can be considered as an exemplary, but maybe not the optimal, case. The

	atm. ν_μ	background μ
L1 (hit veto)	0.96	$4.0 \cdot 10^{-4}$
L2 (vertex cuts)	0.51	$9.8 \cdot 10^{-7}$

Table 7.1: Veto performance - Surviving event fractions of atmospheric muon background and downwards-going atmospheric muon neutrino events at the two levels of the veto process in the southern hemisphere sensitivity study.

resulting spectrum (equation 7.2)is based on a rather hard power law ($E^{-1.72}$), which is somewhat softened by the weak cut-off given by the exponential term.

About 130.000 of the simulated signal events have a vertex in the DeepCore fiducial volume, which we define as a cylinder around string 36 and at the bottom of the detector, with radius 200 m and height 350 m.

The simulated signal set is also used to estimate the background of atmospheric muon neutrinos. For this purpose it is re-weighted to the atmospheric neutrino flux as given by Honda et al. in 2006 [63].

The detector has been triggered with a DeepCore SMT3 condition and the recorded hits have been cleaned by the classic RT hit-cleaning algorithm (R=150 m; T=1000 ns) and a time-window cleaning of 5 μs (see section 4.1).

7.2.2 Atmospheric muon veto

For this study we used the causally related hit veto, as described in section 4.4. The cleaned launches are used as input, no pulse extraction has been performed.

The vertex reconstruction has been done based on the true MC track information and the following cut-variables have been chosen

$$r < 180\text{m}; \qquad z < -210\text{m}; \qquad LLHR < -16. \tag{7.3}$$

These cuts diminish the originally defined fiducial volume by $\sim 1/3$, which is reflected in the signal efficiency, given in table 7.1. In this table we give the fraction of surviving events for signal and background at veto L1 (hit veto) and L2 (vertex cuts). The achieved background rejection is sufficient to reduce the rate of atmospheric muon events to the level of the atmospheric muon neutrino rate. The signal efficiency corrected for the smaller fiducial volume defined by the vertex cuts is $\sim 80\%$.

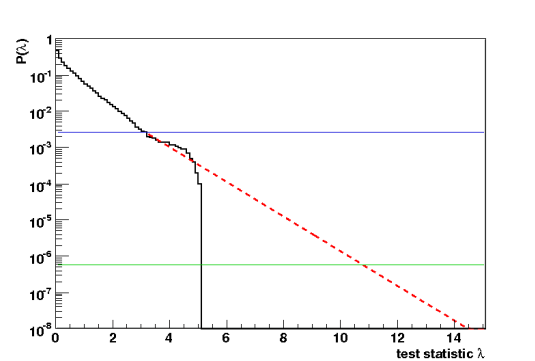# 7. FIRST LOOK ON DEEPCORE DATA AND A FIRST SENSITIVITY ESTIMATION TO A SOUTHERN HEMISPHERE POINT SOURCE

Figure 7.3: Integral probability distribution of the test statistic λ in the background-only hypothesis - The 3σ (blue line) and 5σ (green line) levels are shown. The distribution has been extrapolated to lower probabilities (dashed line).
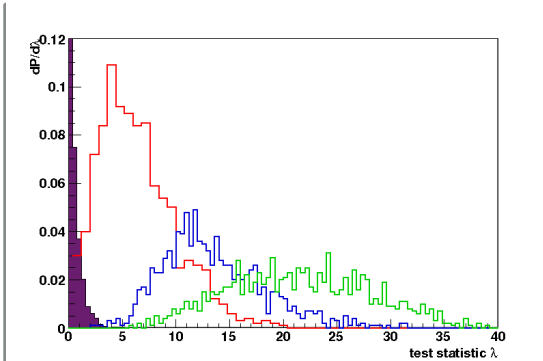
Figure 7.4: Distribution of λ for background alone (purple, filled) and with signal events added to the background - Three different source strengths are shown. Scaled by a factor f_s = 500 (red), 3000 (blue) and 4000 (green).

7.2.3 Point source search strategy

We base this analysis on the unbinned point source search method presented in section 3.6.1. Since we have done no track reconstruction studies, we use the true MC direction of the events and assume an angular resolution similar to the one obtained for AMANDA, $\sigma \approx 2°$. We also consider only events with a true neutrino energy larger then 100 GeV, as below this energy the vertex angle between the observed muon and the interacting neutrino becomes too large. Furthermore, we restrict the search to a declination band of 10° width, centered around the source location.

To determine the significance of an observed value of the test statistic λ, we first compute the probability of a given λ in the null-hypothesis of no signal being present. We therefore scramble the simulated background events 10.000 times in right ascension to obtain effectively independent background sets. Fig. 7.3 shows the integral probability distribution of the thus obtained λ values. The probabilities corresponding to 3σ and 5σ significance level are illustrated by the blue and green line, respectively. The λ value for 3σ can be read directly from the distribution as $\lambda_{3\sigma} = 3.2$, but as the statistics in 10.000 scrambled sky maps are not sufficient to reach to the 5σ level, we have extrapolated the probability distribution in fig. 7.3 with an exponential. From this extrapolation we obtain $\lambda_{5\sigma} = 10.8$.

The distribution of the test statistic λ, with an added signal at different strengths, can

be seen in fig. 7.4. To achieve different source strengths, the flux given in equation 7.2 is scaled by a factor f_s. In fig. 7.4 the λ distributions for factors $f_s = 500$, 3000 and 4000 are shown. These correspond to mean numbers of observed signal events of $\hat{n}_S = 5.3$, 34.1 and 44.8, respectively.

With a wider range of scale factors one can compute the detection probability as a function of the source strength for a given confidence level. This is shown for the 3σ and 5σ level in fig. 7.5 From this figure we can read the number of signal events to be observed for a 3σ (5σ) detection as $\mu = 15$ events (30 events).

By raising the scale factor of the flux f_s until the required number of $\hat{n}_S$ is reached, one can obtain the discovery fluxes after one year in units of the input spectral shape $\xi(E_{\nu_\mu}) = \left(\frac{E_{\nu_\mu}}{[1\,\text{TeV}]} \right)^{-1.72} \exp\left(\sqrt{\frac{E_{\nu_\mu}}{1.35\,\text{TeV}}} \right)$:

$$\Phi_{\text{disc}}(50\%, 3\sigma) = 1.90 \cdot 10^{-8} \cdot \xi(E_{\nu_\mu}) \, \text{TeV}^{-1}\text{cm}^{-2}\text{s}^{-1} \qquad \text{(after one year)} \qquad (7.4)$$

$$\Phi_{\text{disc}}(50\%, 5\sigma) = 3.82 \cdot 10^{-8} \cdot \xi(E_{\nu_\mu}) \, \text{TeV}^{-1}\text{cm}^{-2}\text{s}^{-1} \qquad \text{(after one year)} \qquad (7.5)$$

The corresponding scale factors are $f_s(3\sigma) = 1250$ and $f_s(5\sigma) = 2459$, respectively. These scale factors illustrate quite clearly, that a detection of RX J1713.7-3946 within one year, given the flux from equation 7.2, is not likely. However, that was not to be expected, since it is well known that km^3-scale detectors are needed to reach the necessary sensitivities for a detection of predicted neutrino source fluxes. The DeepCore fiducial volume is $\sim$20 times smaller then the IceCube geometric volume, and the effective volume difference is much larger at energies above a few 100 GeV. Nevertheless, there is room for improvement, especially by the atmospheric neutrino veto, as we will show below.

7.2.4   Sensitivity

We use the method proposed by Feldman and Cousins [45] to determine the sensitivity to RX J1713.7-3946. Since in this study the observable is the test statistic λ, we need to generate our own confidence belts, rather then using the precompiled ones given in [45]. These confidence belts provide the probability density functions $P(\lambda|\hat{n}_S)$ to observe λ at a given source strength $\hat{n}_S$. For each value of λ we estimate the value $\hat{n}_S^{best}$, which maximizes $P(\lambda|\hat{n}_S)$. Then we calculate the ratio

$$R = \frac{P(\lambda|\hat{n}_S)}{P(\lambda|\hat{n}_S^{best})} \qquad (7.6)$$

The confidence belt is then created by adding the values of λ to the acceptance region of a given mean source strength $\hat{n}_S$ in order of decreasing R until the sum of $P(\lambda|\hat{n}_S)$

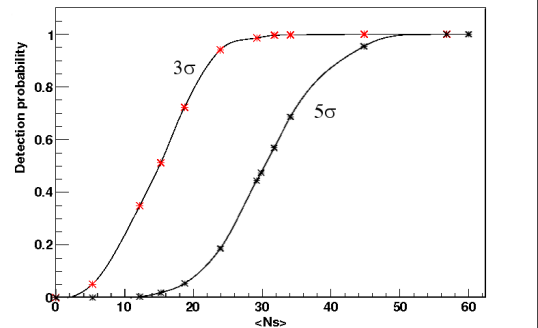# 7. FIRST LOOK ON DEEPCORE DATA AND A FIRST SENSITIVITY ESTIMATION TO A SOUTHERN HEMISPHERE POINT SOURCE

Figure 7.5: Detection probability in dependence of signal strength - The probability distribution is shown at the 3σ (red crosses) and 5σ (black crosses) level in dependence of the source strength, measured by the mean number of observed signal events $\hat{n}_S$.
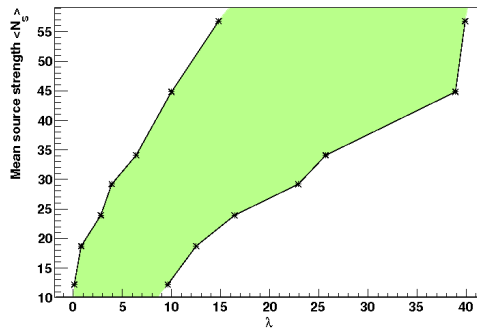
Figure 7.6: Feldman-Cousins confidence belt at the 90% confidence level - The black curves give the upper and lower limit, while the green shade shows the acceptance region.

meets or exceeds the required confidence level. The thus created 90% confidence belt is shown in fig. 7.6 The sensitivity is the average upper limit obtained from the probability distribution of λ for background alone, $P(\lambda|0)$. To get the upper flux limits following this result, the upper limits shown in fig. 7.6 are converted by making use of their corresponding scale factors f_s. For each value of λ the probability $P(\lambda|0)$ is scaled by the factor f_s corresponding to the upper limit of the mean source strength $\hat{n}_S$. Disregarding any systematic uncertainties, the upper flux limit, in units of the spectral shape $\xi(E_{\nu_\mu})$ given in equation 7.2, is

$$\Phi_{90\%} \leq 1.85 \cdot 10^{-8} \cdot \xi(E_{\nu_\mu}) \text{ TeV}^{-1}\text{cm}^{-2}\text{s}^{-1} \qquad \text{(after one year)} \qquad (7.7)$$

This sensitivity, as the discovery flux, is several orders of magnitude above the flux from RX J1713.7-3946 predicted in [68]. However, as mentioned before, this estimation is only a first, low level, step on the way to a point source analysis of the southern sky. On the one hand, higher analysis levels, including reconstruction quality cuts, will lead to lower efficiencies, on the other hand we have not optimized the veto efficiency and the fiducial volume size for best sensitivity. It seems reasonable to assume, that both effects will be of the same order and thus the presented result gives a realistic approximation on the order of magnitude of the sensitivity without the atmospheric

neutrino veto effect.

7.2.5   Sensitivity including the atmospheric neutrino veto

In order to estimate the effect of the atmospheric neutrino veto on the sensitivity of DeepCore to southern sky sources, we applied the analytically calculated veto probability (see chapter 6). Due to the unique position of IceCube at the geographical South Pole, the declination of the source, given above, directly translates to a constant zenith angle position of $50.25°$. The energy dependent atmospheric neutrino veto probability at this zenith angle, and the $10°$ band around it, is shown in the left panel of fig. 7.7 The right panel of the same figure shows the resulting atmospheric neutrino background
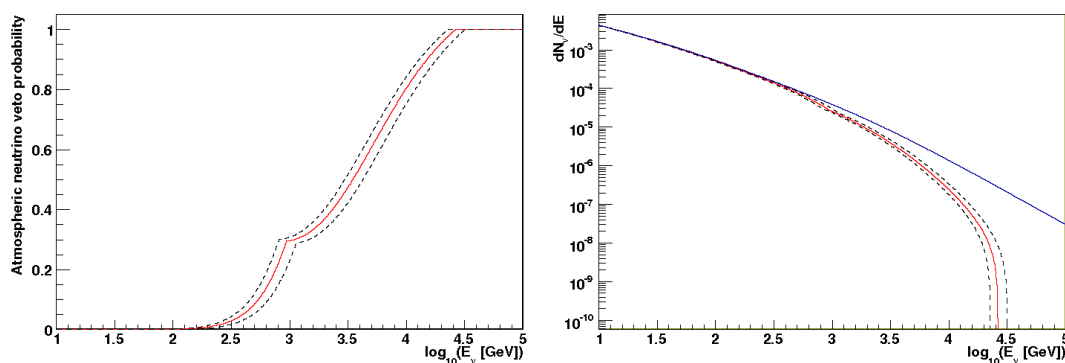

Figure 7.7: Atmospheric neutrino veto probability and resulting observed background spectrum at the position of RX J1713.7-3946 - Left: The red line gives the veto probability for atmospheric neutrinos at an incident zenith angle of $50.25°$, the position of RX J1713.7-3946. The dotted lines denote the probabilities on the borders of the considered zenith band. Right: The resulting observed atmospheric neutrino spectrum if all vetoed atm. neutrinos are removed

spectrum after the veto.

Repeating the above described analysis for the flux of RX J1713.7-3946 (equation 7.2) with the thus modified background flux, results in a sensitivity decreased by almost a factor 3:

$$\Phi_{90\%} \leq 6.64 \cdot 10^{-9} \cdot \xi(E_{\nu_\mu}) \text{ TeV}^{-1}\text{cm}^{-2}\text{s}^{-1} \qquad \text{(after one year)} \qquad (7.8)$$

The corresponding Feldman-Cousins confidence belt is shown in fig. 7.8. The obtained improvement is also reflected in the discovery fluxes for a 50% probability of 3σ (5σ)
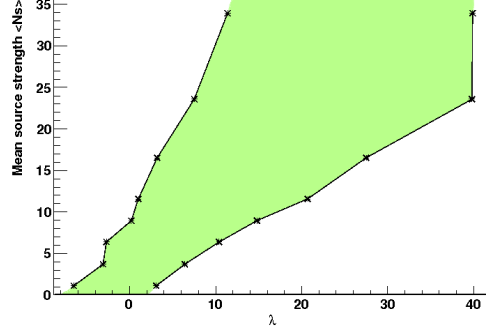
**Figure 7.8: Feldman-Cousins confidence belt at the 90% confidence level with
atmospheric neutrino veto** - The black curves give the upper and lower limit, while the
green shade shows the acceptance region.

detection:

$$\Phi(50\%, 3\sigma) = 5.5 \cdot 10^{-9} \cdot \xi(E_{\nu_\mu}) \text{ TeV}^{-1}\text{cm}^{-2}\text{s}^{-1} \qquad \text{(after one year)} \qquad (7.9)$$

$$\Phi(50\%, 5\sigma) = 1.1 \cdot 10^{-8} \cdot \xi(E_{\nu_\mu}) \text{ TeV}^{-1}\text{cm}^{-2}\text{s}^{-1} \qquad \text{(after one year)} \qquad (7.10)$$

.

This is a significant improvement that shows the impact of the atmospheric neutrino
veto and its importance in any southern sky point source analysis. As the declination
of RX J1713.7-3946 is such that it is not optimal for the atmospheric neutrino veto, we
can expect even larger improvements to the sensitivity on sources which are at larger
declinations (smaller zenith angle in IceCube).

8

Summary and outlook

8.1 Summary

In this thesis we have presented the design study of the low-energy extension to Ice-Cube called DeepCore. DeepCore significantly lowers IceCube's energy threshold and has been devised to provide IceCube with access to various new physics cases. This design study strongly contributed to the approval of the DeepCore project by the National Science Foundation (NSF) in 2008 and to an important part of its financing.

The design and development of atmospheric muon veto techniques, which have taken place in parallel to the DeepCore design, have been reported. This veto technique, for the first time, allows IceCube to gain access to neutrinos from the southern hemisphere. Furthermore, in the course of the atmospheric muon veto development, a new opportunity has been found, which enables a reduction of the flux of atmospheric muon neutrinos, coming from the hemisphere of the detector location. This flux is a background to searches for extra-terrestrial neutrinos and we have reported a first conservative estimation of this atmospheric neutrino veto effect, based on analytic approximations of air-shower cascade developments.

Finally, a first sensitivity estimate to a southern sky point source using DeepCore has been shown, incorporating also the improvement by the atmospheric neutrino veto effect.

The DeepCore design study and the development of the atmospheric muon veto technique have been closely interwoven, as the first DeepCore proposal triggered ideas on the veto and the veto in turn, once established, had substantial influence on the detector design and added another strong argument for the construction of the detector.

We have shown how the feasibility of an active veto against atmospheric muons has been proven for the first time in a two step veto procedure, where the basic idea is to separate neutrino induced muons starting deep inside the detector, from the through-going atmospheric muons. Both veto steps are based on a separation of the detector volume into a central "fiducial volume", basically represented by the densely instrumented DeepCore array, and a surrounding "veto volume", used to identify and reject muons entering the detector from outside. The first step, called "geometrically penalized hit veto", counts hits in the veto volume and assigns weights according to the distance to the fiducial region. It is capable of reducing the muon background by ~ 4 orders of magnitude at a reasonable signal passing rate. The second algorithm is based on a vertex reconstruction and a likelihood estimation of its correctness. By cutting on both, the vertex position and the likelihood value, we have shown that a background rejection on the order of 10^{-6} is feasible, which is necessary to reduce the background muon rate below the rate of atmospheric neutrinos.

Further code developments, done after the first proof of feasibility, have significantly improved the signal efficiency by including the hit timing into a new hit veto algorithm, also presented in this thesis.

The DeepCore design study has been presented in great detail to exemplify the decision making process, which led to the finally deployed layout. Apart from the financial conditions, the frame for the design study was mainly set by the short time from the first proposal of DeepCore, in spring 2007, to the time where the first DeepCore string layout and position had to be determined, in spring 2008. This timing was a consequence of the well-motivated solution to deploy all DeepCore strings within the already planned and financed IceCube deployment seasons.

From the start, the fixed basis of the DeepCore design was given by six additional strings that were to be deployed around a central IceCube string in an equal spacing to all surrounding standard strings. The parameters to tune were mainly the total number of strings and their locations, as well as the number, spacing and type of modules per string.

A decision on the DeepCore layout was, in essence, also a decision for an optimization for different physics cases. In this sense, the goal to improve the sensitivity to neutrino point sources from the Northern hemisphere (without a muon veto) at lower neutrino energies, called for a large, densely instrumented volume and thus eventually for a greater number of additional strings. On the other hand, the prospect to be able to study also neutrino particle physics, such as neutrino oscillations, would profit from

an even denser instrumentation, with more modules per string. The atmospheric muon veto technique, promising access to southern hemisphere point sources and all-year sensitivity to solar WIMP signals, requires a large part of the detector volume to be used in the veto. Thus it also favors a dense central core. Finally, the option to increase the light yield by deploying high quantum efficiency (QE) photo-multiplier tubes (PMTs) on the standard IceCube digital optical modules (DOMs), promised a higher efficiency at a lower risk of strings not being deployed due to missing deployment capacities. The (then unknown) construction progress was potentially limiting the number of additional strings. Thus a decision for less strings, with a denser and more effective instrumentation, was not only scientifically attractive, by the lower energy threshold, but also a safer solution in terms of construction feasibility.

The result of the main DeepCore design study was therefore to install the six additional dedicated DeepCore strings in a 72 m string spacing around a central IceCube string. Each additional string holds 60 DOMs with high QE PMTs, of which 50 modules are positioned at the bottom of the detector in a dense 7 m module spacing, and 10 modules are located in the upper part of the detector in a 10 m spacing. These latter DOMs have been shown to improve the muon veto efficiency for vertically downward-going muons.

It is this configuration, that has finally been deployed in the last austral summer and is now ready for data-taking.

In a later addition, two further strings have been assigned to DeepCore, which are relocated IceCube baseline strings that could not be deployed at their original positions. They will get the same string layout as the first six dedicated DeepCore strings, but have standard, instead of high QE PMTs. In an additional design study, presented in this thesis, the positions of these strings were optimized to provide an even denser string spacing, of ~ 42 m, which further lowers IceCubes energy threshold to well below 10 GeV and will provide additional information to aid low energy event reconstructions, which remain challenging. This last two DeepCore strings are planned for deployment in the upcoming austral summer, which marks the final IceCube construction season.

Apart from the veto and DeepCore design studies, which were embedded in the IceCube collaboration, we have also presented a more general estimation of the probability that an atmospheric muon neutrino can be vetoed in a high energy neutrino telescope. Such neutrinos originate in the same meson decays within cosmic ray air-showers in the atmosphere as do the atmospheric muons. In a neutrino telescope with an atmospheric muon veto capability, such as the one presented for IceCube DeepCore, the

atmospheric neutrino background to an extra-terrestrial neutrino point source search can be reduced. This is possible, if an atmospheric neutrino event is "revealed" to be of atmospheric origin by the detection of its partner muon from the same meson decay in the atmosphere. At the high energies relevant at neutrino telescopes, they have a high chance to reach the detector quasi aligned, assuming the muon has sufficient energy to reach the depth of the veto detector.

We have analytically calculated the probability that an atmospheric neutrino is accompanied by its partner muon, in dependence of the neutrino energy and zenith angle and the muon veto detector depth. We have found, that in principle, vertical downwards directed atmospheric neutrinos with $E_\nu > 10$ TeV can be vetoed with $>99\%$ efficiency at a detector depth comparable to IceCube. On the other hand the effect starts to be noticeable already at neutrino energies as low as 100 GeV.

As a consequence, sensitivities to astro-physical neutrino sources are significantly lowered, as we have shown in the final chapter of this thesis. Furthermore this result imposes a systematic effect for any analysis involving an atmospheric muon veto layer. And as a further impact, it may also influence future designs of high energy neutrino telescopes, as a shallower veto detector results in a higher veto efficiency and consequently an improved sensitivity.

The current status of DeepCore and a first look into DeepCore data was given in the final chapter of the thesis. The first deployed DeepCore string has been taking data for about one year now, and the recently deployed five more DeepCore strings are ready for the new data taking period with all 79 eployed strings, which is about to start. The launch rates of the DeepCore modules are substantially larger then the ones on standard strings, reflecting the use of high QE PMTs, the dense module spacing and the lower trigger threshold required in DeepCore.

We have also shown a first estimate of a sensitivity to the brightest southern sky source in TeV γ-rays, SNR RX J1713.7-3946. This sensitivity has been produced on a low analysis level and is therefore only a rough estimate. Nevertheless, it has been used to estimate the effect of the atmospheric neutrino veto on the sensitivity to southern hemisphere sources. We have found, that the sensitivity is lowered by almost a factor 3, if we employ the analytic calculations of the atmospheric neutrino veto probability derived in this thesis. The source neutrino flux has been taken from [68] and has been inferred from γ-ray observations.

8.2 Outlook

With the upcoming completion of the IceCube neutrino observatory, the age of neutrino astronomy is finally about to start. The discovery of a neutrino point source, 100 years after Hess' discovery of the cosmic rays, will eventually solve the long standing riddle of cosmic ray origin and mark a major step in our understanding of the universe. But IceCube has also a large potential to achieve science goals beyond cosmic ray physics. With the DeepCore extension, its energy threshold will be significantly lowered, potentially allowing to measure neutrino oscillation effects and constrain the oscillation parameters. The lower energy threshold will also extend the parameter space of solar WIMP models that can be tested with IceCube, an analysis complementary to direct dark matter searches and searches for new particles at collider experiments. Also, galactic neutrino point source searches, where softer cut-off spectra are often expected, can be improved by the lower energy threshold. All these cases will also profit from the new opportunity to make DeepCore a detector with full sky (4π) acceptance, given by the atmospheric muon veto.

The development and deployment of DeepCore have so far been a major success, but a lot of work is still to be done to make the above mentioned physics goals realizable.

A central missing piece in the development of analyzes aiming for these goals is a dedicated low energy event reconstruction technique. Such techniques have to be optimized for the denser spacing of DeepCore, which e.g. provides the possibility to measure the initial hadronic cascade that goes along with a starting neutrino induced muon track. These reconstructions are currently under rapid development and first results have shown promising results.

For the atmospheric muon veto the low energy muon track reconstructions are also of crucial importance, as a track hypothesis is needed in the vertex reconstruction algorithm. So far the idealization of the true muon track from the simulation has been used. The advent of new track reconstructions will thus require a re-tuning of the veto algorithms.

Any analysis which will employ the atmospheric muon veto will also need to handle the atmospheric neutrino veto effect correctly. The efforts to understand the full impact of this effect have only just started. In this thesis the atmospheric neutrino veto probability has been calculated analytically in a conservative fashion, but to incorporate the veto possibility provided by all high energy muons in an air-shower, detailed Monte

Carlo simulations are necessary. New, dedicated simulation techniques are needed for this, as the neutrino simulation has to be coupled to the air-shower muon simulation. Previously these have always been completely decoupled. First attempts to such simulations have shown that this needs a significantly increased computing power. However, development efforts of these simulations are underway and will form a significant part in the systematics checks of all analyzes which make use of the muon veto.

References

[1] **LHC research programme gets underway**. CERN press release, 30.03.2010, http://press.web.cern.ch/press/PressReleases/ Releases2010/PR07.10E.html. 3

[2] C. ADLOFF ET AL. **Deep-inelastic inclusive e p scattering at low x and a determination of alpha(s)**. *Eur. Phys. J.*, **C21**:33–61, 2001. 44

[3] K2K COLLABORATION: M. H. AHN. **Measurement of Neutrino Oscillation by the K2K Experiment**. *Physical Review D*, **74**:072003, 2006. 39

[4] E. K. AKHMEDOV, M. MALTONI, AND A. Y. SMIRNOV. **1-3 leptonic mixing and the neutrino oscillograms of the Earth**. *Journal of High Energy Physics*, **5**:77, May 2007. 40, 41

[5] R. B. ALLEY. **The two-mile time machine : ice cores, abrupt climate change, and our future**. *Princeton, NJ: Princeton University Press*, page 229, 2000. 51

[6] T. ANTONI ET AL. **The Cosmic ray experiment KASCADE**. *Nucl. Instrum. Meth.*, **A513**:490–510, 2003. 64

[7] JOHN N. BAHCALL AND PETER MÉSZÁROS. **5–10 GeV Neutrinos from Gamma-Ray Burst Fireballs**. *Phys. Rev. Lett.*, **85**(7):1362–1365, Aug 2000. 89

[8] C. BAIXERAS. **The MAGIC telescope**. *Nuclear Physics B - Proceedings Supplements*, **114**:247 – 252, 2003. Proceedings of the XXXth International Meeting of Fundamentals Physics. 33

[9] G. D. BARR, T. K. GAISSER, P. LIPARI, S. ROBBINS, AND T. STANEV. **Three-dimensional calculation of atmospheric neutrinos**. *Phys. Rev. D*, **70**(2):023006, Jul 2004. 80, 84, 105

[10] A. R. BELL. **The Acceleration of cosmic rays in shock fronts. I**. *Mon. Not. Roy. Astron. Soc.*, **182**:147–156, 1978. 29

[11] J. BRAUN, J. DUMM, F. DE PALMA, C. FINLEY, A. KARLE, AND T. MONTARULI. **Methods for point source analysis in high energy neutrino telescopes**. *Astroparticle Physics*, **29**:299–305, May 2008. 67

[12] E. V. BUGAEV, A. MISAKI, V. A. NAUMOV, T. S. SINEGOVSKAYA, S. I. SINEGOVSKY, AND N. TAKAHASHI. **Atmospheric muon flux at sea level, underground, and underwater**. *Phys. Rev. D*, **58**(5):054001, Jul 1998. 128

[13] THE ZEUS COLLABORATION S. CHEKANOV AND ET AL. **Measurement of the neutral current cross section and F2 structure function for deep inelastic ep scattering at HERA**. *Eur. Phys. J. C*, **21**(3):443–471, 2001. 44

[14] D. CHIRKIN. *"Cosmic Ray Energy Spectrum Measurement with the Antarctic Muon and Neutrino Detector Array (AMANDA)"*. PhD thesis, University of California at Berkeley, 2003. 64

[15] D. CLOWE, M. BRADAČ, A. H. GONZALEZ, M. MARKEVITCH, S. W. RANDALL, C. JONES, AND D. ZARITSKY. **A Direct Empirical Proof of the Existence of Dark Matter**. *The Astrophysical Journal*, **648**:L109–L113, September 2006. 38

[16] MINOS COLLABORATION. **Measurement of Neutrino Oscillations with the MINOS Detectors in the NuMI Beam**. *Physical Review Letters*, **101**:131802, 2008. 39

[17] THE ANTARES COLLABORATION. **A Deep Sea Telescope for High Energy Neutrinos**. *astro-ph/9907432*, 1999. 6, 88

[18] THE KM3NET COLLABORATION. **Conceptual Design Report**. http://km3net.org. 125

[19] THE PIERRE AUGER COLLABORATION. **Correlation of the Highest-Energy Cosmic Rays with Nearby Extragalactic Objects**. *Science*, **318**(5852):938–943, 2007. 12

[20] THE SUPER-KAMIOKANDE COLLABORATION. **Evidence for Oscillation of Atmospheric Neutrinos**. *Phys. Rev. Lett.*, **81**(8):1562–1567, Aug 1998. 6, 39

[21] THE SUPER-KAMIOKANDE COLLABORATION. **Determination of Solar Neutrino Oscillation Parameters using 1496 Days of Super-Kamiokande-I Data**. *Physics Letters B*, **539**:179, 2002. 39

[22] W. RHODE D. CHIRKIN. **Muon Monte Carlo: A new high-precision tool for muon propagation through matter**. In C. SPIERING K.-H. KAMPERT, G. HEINZELMANN, editor, *Proc. 27th Int. Cosmic Ray Conf.*, pages 1017–1020. Copernicus Gesellschaft, 2001. 47, 63, 123

[23] LUKE O'C. DRURY. **Acceleration of cosmic rays**. *Contemp. Phys.*, **35**:231–242, 1994. 26

[24] A. ACHTERBERG ET AL. **First year performance of the IceCube neutrino telescope**. *Astroparticle Physics*, **26**(3):155 – 173, 2006. 4

[25] A. ACHTERBERG ET AL. **Five years of searches for point sources of astrophysical neutrinos with the AMANDA-II neutrino telescope**. *Phys. Rev. D*, **75**(10):102001, May 2007. 5, 54

[26] A. GROSS ET AL. **Search for Sources of Astrophysical Neutrinos with IceCube**. *Proceedings to the 4th International Meeting on High Energy Gamma-Ray Astronomy, Heidelberg, Germany, 7-11 July 2008; AIP Conference Proceedings*, **1085**:779–782, 2008. 56

[27] D. HECK ET AL. *"CORSIKA: A Monte Carlo Code to Simulate Extensive Air Showers"*. Technical report, Forschungszentrum Karlsruhe. 63, 64

REFERENCES

[28] F. A. Aharonian et al. **High-energy particle acceleration in the shell of a supernova remnant**. *Nature*, **432**:75–77, November 2004. 136

[29] F. Aharonian et al. **Calibration of cameras of the H.E.S.S. detector**. *Astroparticle Physics*, **22**:109–125, November 2004. 33

[30] F. Aharonian et al. **Primary particle acceleration above 100 TeV in the shell-type supernova remnant RX J1713.7-3946 with deep HESS observations**. *Astronomy & Astrophysics*, **464**:235–243, March 2007. 5, 37, 136

[31] "F.Aharonian et al. **First detection of a VHE gamma-ray spectral maximum from a cosmic source: HESS discovery of the Vela X nebula**. *Astronomy & Astrophysics*, **448**:L43–L47, 2006. 5, 37

[32] "F.Aharonian et al. **Observations of the Crab nebula with HESS**. *Astronomy & Astrophysics*, **457**:899–915, 2006. 5, 37

[33] "F.Aharonian et al. **Spectrum and variability of the Galactic center VHE γ-ray source HESS J1745-290**. *Astronomy & Astrophysics*, **503**:817–825, 2009. 5, 37

[34] J. R. Petit et al. **Climate and atmospheric history of the past 420,000 years from the Vostok ice core, Antarctica**. *Nature*, **399**:429–436, 1999. 53

[35] M. Tegmark et al. **Cosmological constraints from the SDSS luminous red galaxies**. *Phys. Rev. D*, **74**(12):123507, Dec 2006. 38

[36] Q. R. Ahmad et al. **Measurement of the Rate of $\nu e + d \rightarrow p + p + e-$ Interactions Produced by $B8$ Solar Neutrinos at the Sudbury Neutrino Observatory**. *Phys. Rev. Lett.*, **87**(7):071301, Jul 2001. 39

[37] J. Ahrens et al. (AMANDA collaboration). **Muon track reconstruction and data selection techniques in AMANDA**. *Nuclear Instruments and Methods in Physics Research A*, **524**:169–194, May 2004. 66

[38] G. Alimont et al. (BOREXINO collaboration). **The Borexino detector at the Laboratori Nazionali del Gran Sasso**. *Nuclear Instruments and Methods in Physics Research A*, **600**:568–593, March 2009. 69

[39] M. Ackermann et al. (IceCube collaboration). **Optical properties of deep glacial ice at the South Pole**. *Journal of Geophysical Research (Atmospheres)*, **111**:13203–+, July 2006. 51, 52, 53, 63

[40] R. Abbasi et al. (IceCube Collaboration). **The IceCube data acquisition system: Signal capture, digitization, and timestamping**. *Nuclear Instruments and Methods in Physics Research Section A: Accelerators, Spectrometers, Detectors and Associated Equipment*, **601**(3):294 – 316, 2009. 59

[41] R. Abbasi et al. (IceCube Collaboration). **Calibration and Characterization of the IceCube Photomultiplier Tube**. *ArXiv e-prints*, February 2010. 58, 59

[42] C. Amsler et al. (Particle Data Group). Physics Letters B667, 1, 2008. "and 2009 partial update for the 2010 edition". 46

[43] S. Euler. *"On the detection of low energy neutrino events with full sky acceptance with the IceCube DeepCore detector"*. Master's thesis, Rheinisch Westfälische Technische Hochschule Aachen, 2008. 75, 77, 81, 82, 108, 109, 110, 113

[44] S. Euler, A. Gross, J-P. Huelss, E. Resconi, O. Schulz, and C. Wiebusch. **IceCube Deep Core Design Study - Fully Contained Events**. Presentation at the DeepCore Workshop in Stockholm, March 2008; unpublished. 103, 104

[45] G. J. Feldman and R. D. Cousins. **Unified approach to the classical statistical analysis of small signals**. *Phys. Rev. D*, **57**:3873–3889, April 1998. 139

[46] ENRICO FERMI. **On the Origin of the Cosmic Radiation**. *Phys. Rev.*, **75**(8):1169–1174, Apr 1949. 29

[47] H. Fesefeldt. **THE SIMULATION OF HADRONIC SHOWERS: PHYSICS AND APPLICATIONS**. PITHA-85-02. 64

[48] R. S. Fletcher, T. K. Gaisser, Paolo Lipari, and Todor Stanev. **sibyll: An event generator for simulation of high energy cosmic ray cascades**. *Phys. Rev. D*, **50**(9):5710–5731, Nov 1994. 34

[49] R. S. Fletcher, T. K. Gaisser, Paolo Lipari, and Todor Stanev. **sibyll: An event generator for simulation of high energy cosmic ray cascades**. *Phys. Rev. D*, **50**(9):5710–5731, Nov 1994. 64

[50] Y. Fukuda et al. **The Super-Kamiokande detector**. *Nucl. Instrum. Meth.*, **A501**:418–462, 2003. 69

[51] T. K. Gaisser. *Cosmic Rays and Particle Physics*. Cambridge University Press, 1990. xi, 14, 18

[52] R. Gandhi, C. Quigg, M. H. Reno, and I. Sarcevic. **Ultrahigh-energy neutrino interactions**. *Astroparticle Physics*, **5**:81–110, August 1996. 44

[53] Askhat Gazizov and Marek P. Kowalski. **ANIS: High energy neutrino generator for neutrino telescopes**. *Comput. Phys. Commun.*, **172**:203–213, 2005. 63, 64

[54] Graciela Gelmini, Paolo Gondolo, and Gabriele Varieschi. **Measuring the prompt atmospheric neutrino flux with down-going muons in neutrino telescopes**. *Phys. Rev. D*, **67**(1):017301, Jan 2003. 128

[55] Sheldon L. Glashow. **Resonant Scattering of Antineutrinos**. *Phys. Rev.*, **118**(1):316–317, Apr 1960. 44

[56] A. Gould. **Cosmological density of WIMPs from solar and terrestrial annihilations**. *The Astrophysical Journal*, **388**:338–344, April 1992. 38

[57] D. Grant. **DeepCore Geometry Studies**. Presentation at the DeepCore Workshop in Stockholm, March 2008; unpublished. 99, 101

[58] D. Grant. **Rate studies for neutrino oscillations in DeepCore**. Presentation at the IceCube spring collaboration meeting 2008 in Madison, Wisconsin, U.S.A.; unpublished. 111

[59] K. Greisen. *Extensive Air Showers*. North Holland Publishing Co., Amsterdam, 1965. 64

150

[60] V. F. HESS. **Über Beobachtungen der durchdringen-den Strahlung bei sieben Freiballonfahrten**. *Phys. Z.*, **13**:1084, 1912. 3

[61] A. M. HILLAS. **The Origin of Ultrahigh-Energy Cosmic Rays**. *Ann. Rev. Astron. Astrophys.*, **22**:425–444, 1984. 26

[62] JOERG R. HOERANDEL. **On the knee in the energy spectrum of cosmic rays**. *Astropart. Phys.*, **19**:193–220, 2003. 10, 64

[63] M. HONDA, T. KAJITA, K. KASAHARA, S. MIDORIKAWA, AND T. SANUKI. **Calculation of atmospheric neutrino flux using the interaction model calibrated with atmospheric muon data**. *Phys. Rev. D*, **75**(4):043006–+, February 2007. 137

[64] J.-P. HUELSS. **P-Hit/P-noHit Likelihood identification ofstarting muons**. Presentation at the IceCube spring collaboration meeting 2007 in Lake Geneva, Wisconsin, U.S.A.; unpublished. 76

[65] ICRU. **Stopping Powers and Ranges for Protons and Alpha Particles**, 1993. Tables and graphs of these data are available at http://physics.nist.gov/PhysRefData/. 46

[66] J.D. JACKSON. *Classical Electrodynamics*, **2010**. John Wiley and Sons, 1998. 48, 49

[67] N. N. KALMYKOV, S. S. OSTAPCHENKO, AND A. I. PAVLOV. **EAS and a quark - gluon string model with jets**. *Bull. Russ. Acad. Sci. Phys.*, **58**:1966–1969, 1994. 64

[68] A. KAPPES, J. HINTON, C. STEGMANN, AND F. A. AHARONIAN. **Potential Neutrino Signals from Galactic γ-Ray Sources**. *Astrophysical Journal*, **656**:870–878, February 2007. 136, 140, 146

[69] TAMAR KASHTI AND ELI WAXMAN. **Astrophysical Neutrinos: Flavor Ratios Depend on Energy**. *Phys. Rev. Lett.*, **95**(18):181101, Oct 2005. 32

[70] S. R. KELNER AND F. A. AHARONIAN. **Energy spectra of gamma rays, electrons, and neutrinos produced at interactions of relativistic protons with low energy radiation**. *Phys. Rev. D*, **78**(3):034013, Aug 2008. 34

[71] S. R. KELNER, F. A. AHARONIAN, AND V. V. BUGAYOV. **Energy spectra of gamma rays, electrons, and neutrinos produced at proton-proton interactions in the very high energy regime**. *Phys. Rev. D*, **74**(3):034018, Aug 2006. 4, 5, 34, 35, 36, 37

[72] AMIR LEVINSON AND ELI WAXMAN. **Probing Microquasars with TeV Neutrinos**. *Physical Review Letters*, **87**:171101, 2001. 28

[73] PAOLO LIPARI. **Lepton spectra in the earth's atmosphere**. *Astroparticle Physics*, **1**(2):195 – 227, 1993. 128

[74] J. LUNDBERG, P. MIOCINOVIC, K. WOSCHNAGG, T. BURGESS, J. ADAMS, S. HUNDERTMARK, P. DESIATI, AND P. NIESSEN. **Light tracking through ice and water–Scattering and absorption in heterogeneous media with Photonics**. *Nuclear Instruments and Methods in Physics Research Section A: Accelerators, Spectrometers, Detectors and Associated Equipment*, **581**(3):619 – 631, 2007. 63, 77

[75] G. MAIER, V. A. ACCIARI, R. AMINI, AND ET AL. **VERITAS: Status and Latest Results**. In *International Cosmic Ray Conference*, **3** of *International Cosmic Ray Conference*, pages 1457–1460, 2008. 33

[76] O. MENA, I. MOCIOIU, AND S. RAZZAQUE. **Neutrino mass hierarchy extraction using atmospheric neutrinos in ice**. *Physical Review D*, **78**(9):093003–+, November 2008. 88

[77] S. P. MIKHEEV AND A. YU. SMIRNOV. **Resonance enhancement of oscillations in matter and solar neutrino spectroscopy**. *Sov. J. Nucl. Phys.*, **42**:913–917, 1985. 41

[78] A. MÜCKE, R. ENGEL, J. P. RACHEN, R. J. PROTHEROE, AND T. STANEV. **Monte Carlo simulations of photohadronic processes in astrophysics**. *Computer Physics Communications*, **124**:290–314, February 2000. 33

[79] PAVEL M. NADOLSKY ET AL. **Implications of CTEQ global analysis for collider observables**. *Phys. Rev.*, **D78**:013004, 2008. 44

[80] W. RALPH NELSON, H. HIRAYAMA, AND DAVID W. O. ROGERS. **The EGS4 code system**. SLAC-0265. 64

[81] K. WOSCHNAGG P. B. PRICE AND D. CHIRKIN. **Age vs depth of glacial ice at South Pole**. *Geophys. Res. Lett.*, **27**(14):2129–2132, 2000. 50

[82] ALLAN HALLGREN KLAS HULTQVIST CHRISTIAN WALCK CARLOS PEREZ DE LOS HEROS PER OLOF HULTH, OLGA BOTNER. **A low energy extension of the IceCube neutrino telescope - Application submitted to the KAW Foundation**. Unpublished document. 92, 94

[83] J. RANFT. **The Dual parton model at cosmic ray energies**. *Phys. Rev.*, **D51**:64–84, 1995. 64

[84] V. C. RUBIN AND W. K. FORD, JR. **Rotation of the Andromeda Nebula from a Spectroscopic Survey of Emission Regions**. *The Astrophysical Journal*, **159**:379–+, February 1970. 38

[85] S. SCHÖNERT, T. K. GAISSER, E. RESCONI, AND O. SCHULZ. **Vetoing atmospheric neutrinos in a high energy neutrino telescope**. *Phys. Rev. D*, **79**(4):043009–+, February 2009. 2, 122

[86] Y. SESTAYO. *Search for high energy neutrinos from our Galaxy with IceCube*. PhD thesis, Ruperto-Carola University Heidelberg, 2010. 37

[87] D. N. SPERGEL, L. VERDE, H. V. PEIRIS, E. KOMATSU, M. R. NOLTA, C. L. BENNETT, M. HALPERN, G. HINSHAW, N. JAROSIK, A. KOGUT, M. LIMON, S. S. MEYER, L. PAGE, G. S. TUCKER, J. L. WEILAND, E. WOLLACK, AND E. L. WRIGHT. **First Year Wilkinson Microwave Anisotropy Probe (WMAP) Observations: Determination of Cosmological Parameters**. *The Astrophysical Journal*, **148**:175, 2003. 38

[88] BIERMANN P. L. STANEV, T. AND T. K. GAISSER. **Cosmic rays. IV. The spectrum and chemical composition above 10' GeV**. *Astronomy and Astrophysics*, **274**:902, 1993. 10

REFERENCES

[89] THE PIERRE AUGER COLLABORATION. **Measurement of the energy spectrum of cosmic rays above 10ˆ18 eV using the Pierre Auger Observatory**. *Phys. Lett.*, **B685**:239–246, feb 2010. 12

[90] ELI WAXMAN AND JOHN BAHCALL. **High Energy Neutrinos from Cosmological Gamma-Ray Burst Fireballs**. *Phys. Rev. Lett.*, **78**(12):2292–2295, Mar 1997. 29

[91] W. R. WEBBER. *Composition and Origin of Cosmic Rays*. D. Reidel Publishing Company, Dordrecht, 1983. 10

[92] C. WENDT AND C. PETTERSEN. **Test Results for 6 High-QE DOMs**. Presentation at the IceCube spring collaboration meeting 2008 in Madison, Wisconsin, U.S.A.; unpublished. 100

[93] K. WERNER. **Strings, pomerons and the VENUS model of hadronic interactions at ultrarelativistic energies,**. *Physics Reports*, **232**(2-5):87 − 299, 1993. 64

[94] W. WHANLON. **Updated cosmic ray spectrum**. http://www.physics.utah.edu/ whanlon/spectrum.html. 11

[95] L. WOLFENSTEIN. **Neutrino oscillations in matter**. *Phys. Rev. D*, **17**(9):2369–2374, May 1978. 41

[96] F. ZWICKY. **Die Rotverschiebung von extragalaktischen Nebeln**. *Helvetica Physica Acta*, **6**:110–127, 1933. 38

Acknowledgements

I would not have been able to write this thesis without the help of many people that I want to thank here. Whether they encouraged and motivated me, advised and taught me or gave me their love and friendship, they all contributed to the outcome of this work and I am deeply thankful for that.

My first and foremost thanks are to my supervisor Dr. Elisa Resconi. She gave me the opportunity to join IceCube and write this thesis and she has put her trust and confidence in me from the first day. Her positive and focused approach to our work has not only been a great motivation, but also a great inspiration. And besides that, it has always been fun to work with her. Thanks Elisa!

The members of our IceCube group in Heidelberg deserve special thanks. Not only are they great physicists with whom it is most productive to work and discuss, but they have also become friends. Thank you, Andreas, Cecile, Claudine, Markus, Martin, Sirin and Yolanda!

Many people within the IceCube collaboration have contributed significantly to the work in this thesis. Most prominent among them are Sebastian Euler and Darren Grant who have done great work in the DeepCore design study. Big thanks also to the whole low-energy group of IceCube for making the work on DeepCore not only very productive and successful, but also a lot of fun.
I also want to thank my fellow pole-travelers Karim Laihem, Steve Movit, Benjamin Semburg and Andreas Tepe for sharing the most amazing trip of my life.
Furthermore, my thanks go to all the other "Cubers" out there that create a productive and enjoyable atmosphere within this remarkable collaboration. Thanks!

I would like to thank Prof. Thomas K. Gaisser and Stefan Schönert for their collaboration on the atmospheric neutrino veto assessment. It was a pleasure to work with them on such an exciting new idea. Thank you!

Declaration

I herewith declare that I have produced this paper without the prohibited assistance of third parties and without making use of aids other than those specified; notions taken over directly or indirectly from other sources have been identified as such. This paper has not previously been presented in identical or similar form to any other German or foreign examination board.

The thesis work was conducted from 01.01.2007 to 10.05.2010 under the supervision of Dr. Elisa Resconi at the Max-Planck Institut für Kernphysik, Heidelberg.

Heidelberg,